2011

MODELING AND QUANTITATIVE ANALYSIS OF WHITE MATTER FIBER TRACTS IN DIFFUSION TENSOR IMAGING

Xuwei Liang
University of Kentucky, xuwei.liang@gmail.com

ABSTRACT OF DISSERTATION

Xuwei Liang

The Graduate School

University of Kentucky

2011

MODELING AND QUANTITATIVE ANALYSIS OF WHITE MATTER FIBER TRACTS IN DIFFUSION TENSOR IMAGING

ABSTRACT OF DISSERTATION

A dissertation submitted in partial fulfillment of the
requirements for the degree of Doctor of Philosophy in the
College of Engineering
at the University of Kentucky

By

Xuwei Liang

Lexington, Kentucky

Director: Dr. Jun Zhang, Professor of Computer Science

Lexington, Kentucky

2011

ABSTRACT OF DISSERTATION

MODELING AND QUANTITATIVE ANALYSIS OF WHITE MATTER FIBER TRACTS IN DIFFUSION TENSOR IMAGING

Diffusion tensor imaging (DTI) is a structural magnetic resonance imaging (MRI) technique to record incoherent motion of water molecules and has been used to detect micro structural white matter alterations in clinical studies to explore certain brain disorders. A variety of DTI based techniques for detecting brain disorders and facilitating clinical group analysis have been developed in the past few years. However, there are two crucial issues that have great impacts on the performance of those algorithms. One is that brain neural pathways appear in complicated 3D structures which are inappropriate and inaccurate to be approximated by simple 2D structures, while the other involves the computational efficiency in classifying white matter tracts.

The first key area that this dissertation focuses on is to implement a novel computing scheme for estimating regional white matter alterations along neural pathways in 3D space. The mechanism of the proposed method relies on white matter tractography and geodesic distance mapping. We propose a mask scheme to overcome the difficulty to reconstruct thin tract bundles. Real DTI data are employed to demonstrate the performance of the proposed technique. Experimental results show that the proposed method bears great potential to provide a sensitive approach for determining the white matter integrity in human brain.

Another core objective of this work is to develop a class of new modeling and clustering techniques with improved performance and noise resistance for separating reconstructed white matter tracts to facilitate clinical group analysis. Different strategies are presented to handle different scenarios. For whole brain tractography reconstructed white matter tracts, a Fourier descriptor model and a clustering algorithm based on multivariate Gaussian mixture model and expectation maximization are proposed. Outliers are easily handled in this framework. Real DTI data experimental results show that the proposed algorithm is relatively effective and may offer an alternative for existing white matter fiber clustering methods. For a small amount of white matter fibers, a modeling and clustering algorithm with the capability of handling white matter fibers with unequal length and sharing no common starting region is also proposed and evaluated with real DTI data.

KEYWORDS: Diffusion Tensor Imaging (DTI), White Matter, Quantitative Analysis, Modeling, Clustering

Xuwei Liang

Student's Signature

July 18, 2011

Date

MODELING AND QUANTITATIVE ANALYSIS OF WHITE MATTER FIBER TRACTS IN DIFFUSION TENSOR IMAGING

By

Xuwei Liang

Dr. Jun Zhang

Director of Dissertation Signature

Dr. Raphael Finkel

Director of Graduate Studies Signature

July 18, 2011

Date

RULES FOR THE USE OF DISSERTATIONS

Unpublished dissertations submitted for the Doctor's degree and deposited in the University of Kentucky Library are as a rule open for inspection, but are to be used only with due regard to the rights of the authors. Bibliographical references may be noted, but quotations or summaries of parts may be published only with the permission of the author, and with the usual scholarly acknowledgements.

Extensive copying or publication of the dissertation in whole or in part also requires the consent of the Dean of the Graduate School of the University of Kentucky.

A library that borrows this dissertation for use by its patrons is expected to secure the signature of each user.

Name	Date

DISSERTATION

Xuwei Liang

The Graduate School

University of Kentucky

2011

MODELING AND QUANTITATIVE ANALYSIS OF WHITE MATTER FIBER TRACTS IN DIFFUSION TENSOR IMAGING

DISSERTATION

A dissertation submitted in partial fulfillment of the
requirements for the degree of Doctor of Philosophy in the
College of Engineering
at the University of Kentucky

By

Xuwei Liang

Lexington, Kentucky

Director: Dr. Jun Zhang, Professor of Computer Science

Lexington, Kentucky

2011

ACKNOWLEDGEMENTS

There have been so many kinds of support, help, and encouragement in the development of this dissertation. Here is the top seven list of people I would like to acknowledge with my sincere gratitude:

1. My advisor, Dr. Jun Zhang, whose insight, guidance, and inspiration led me all the way through the long road of my Ph.D. studies. It is him who introduced me to the wonderful world of computational medical imaging and invested tremendous time, energy, and wisdom into my graduate education. Without my advisor's continual excellent support and help this work would not have been possible.

2. The faculty members who graciously served on my dissertation committees: Dr. Grzegorz (Greg) W Wasilkowski (Department of Computer Science), Dr. Jerzy W Jaromczyk (Department of Computer Science), Dr. Jinze Liu (Department of Computer Science), and Dr. Fuqian Yang (Department of Chemical and Materials Engineering).

3. Dr. Stephen E. Rose at the University of Queensland, Australia, who kindly provided the diffusion tensor data used in this dissertation, tirelessly answered all my questions about it, and carefully commented on the results in chapter 2.

4. Dr. Ning Kang at the University of California San Diego, for providing valuable discussions and suggestions for the work in chapter 2.

5. Dr. Jie Wang at the Indiana University Northwest, for help and advice with the Non-negative matrix factorization.

6. All my fellow officemates in the HiPSCCS lab during my stay, for ensuring that the life as a doctoral student is more than a fun and valuable moment.

7. My family, who are the constant sources of support, love, and happiness in my life. Without them, I could never have finished this dissertation.

The author would like to express his gratitude to the funding agencies for providing the financial support. The research work with this dissertation was supported:

- in part by the US National Science Foundation under grant CCF-0527967 and CCF-0727600
- in part by the National Institutes of Health under grant 1R01HL086644-01
- in part by the Kentucky Science and Engineering Foundation under grant KSEF-148-502-06-186
- in part by the Alzheimer's Association under grant NIRG-06-25460

Table of Contents

Acknowledgements iii

List of Tables viii

List of Figures ix

List of Files xiv

1 Introduction 1
- 1.1 Diffusion Tensor Imaging . . . 1
  - 1.1.1 Basics of DTI . . . 2
  - 1.1.2 Diffusion Tensor Calculation . . . 3
  - 1.1.3 Quantitative Diffusion Properties . . . 5
- 1.2 White Matter Tractography and Neuroscience Applications . . . 10
- 1.3 Tractography Algorithm and DTI Data Acquisition . . . 11
  - 1.3.1 Tractography Algorithm . . . 11
  - 1.3.2 DTI Data Acquisition . . . 11
- 1.4 Organization of the Dissertation . . . 13

2 Quantitative and Visual Analysis of White Matter Integrity 18
- 2.1 Outline . . . 18
- 2.2 Introduction . . . 18
- 2.3 Methods . . . 19
  - 2.3.1 Fiber Tract Bundle Mask . . . 19
  - 2.3.2 Geodesics and Geodesic Distance Mapping . . . 21
  - 2.3.3 Isonodes . . . 22
  - 2.3.4 Local Diffusion Property Calculation . . . 22
  - 2.3.5 Isonode Visualization Scheme . . . 23
- 2.4 Experiments and Results . . . 23
  - 2.4.1 Subjects . . . 24
  - 2.4.2 Quantitative Analysis . . . 26
  - 2.4.3 The Cingulum Bundles . . . 26
  - 2.4.4 The GCC Bundle . . . 28
- 2.5 Discussion and Conclusion . . . 30

3 A Unified Framework for Modeling and Clustering a Small Number of White Matter Tracts 35
- 3.1 Outline . . . 35
- 3.2 Introduction . . . 35
- 3.3 Theory . . . 39
  - 3.3.1 Streamline Representation . . . 39
  - 3.3.2 Streamline Similarity Metrics . . . 43
- 3.4 Methods . . . 46
  - 3.4.1 Streamline Parameter Fitting . . . 46

3.4.2 Matching Starting Point Correspondence . . . 47
3.4.3 Segment Correspondences and Bilateral Matching . . . 48
3.5 Experimental Results . . . 50
3.5.1 DTI Data . . . 50
3.5.2 CST-MCP Tracts . . . 50
3.5.3 CST-CPT-PTR Tracts . . . 52
3.6 Discussion and Conclusion . . . 53

4 Modeling White Matter Tract Shape Patterns using Fourier Descriptors 64
4.1 Outline . . . 64
4.2 Introduction . . . 64
4.3 Methods . . . 66
4.3.1 White Matter Tract Parameter Fitting . . . 66
4.3.2 Shape Signatures . . . 66
4.3.3 Tract Similarity and Clustering . . . 71
4.4 Experiments and Results . . . 71
4.4.1 DTI Data . . . 71
4.4.2 Experiments . . . 72
4.5 Discussion and Conclusion . . . 76

5 White Matter Tracts Clustering using Bayesian Inference to Facilitate Group Analysis 78
5.1 Introduction . . . 78
5.2 Methods . . . 80
5.2.1 The Statistical Model . . . 80
5.2.2 Feature Selection . . . 82
5.2.3 Unsupervised Clustering . . . 87
5.2.4 Supervised Clustering . . . 89
5.3 Experiments and Results . . . 89
5.3.1 DTI Data . . . 92
5.3.2 Without Outliers . . . 92
5.3.3 With Outliers . . . 93
5.4 Discussion . . . 93
5.4.1 Evaluation of the Proposed Fourier Descriptor Formation . . . 93
5.4.2 Comparison with K-means . . . 97
5.4.3 Impacts of the Number of Fourier Descriptors . . . 97
5.4.4 Sensitivity of π Values . . . 99
5.4.5 Initialization of the EM Algorithm . . . 100
5.5 Conclusion . . . 102

6 Evaluation of the Nonnegative Matrix Factorization Technique in White Matter Tract Segmentation 104
6.1 Outline . . . 104
6.2 Introduction . . . 104
6.3 Methods . . . 105
6.3.1 Fiber Tract Parameter Fitting . . . 105
6.3.2 Tract Characterization . . . 106

6.3.3 Transformation of Tract Characterizations into Frequency Space . . 107
6.3.4 Clustering based on Nonnegative Matrix Factorization 108
6.4 Experiments and Results 109
6.4.1 Data Acquisition 109
6.4.2 Experiments and Results 109
6.5 Discussion and Conclusion 111

7 Summary and Outlook **113**
7.1 Summary 113
7.2 Future Research Outlook 115

Bibliography **117**

Vita **127**

List of Tables

2.1 Mean ($\pm SD$) values for the FA and MD measures for the entire volumetric GCC bundle for MCI and normal control groups. The unit of MD is ($10^{-6} mm^2/sec$). 29

List of Figures

1.1 Illustration of a second order diffusion tensor represented as an ellipsoid. . . 3
1.2 Illustration of the six gradient applied images and the base line image used to estimate diffusion tensor. Images are shown in axial, sagittal, and coronal views respectively. 5
1.3 Illustration of anisotropy measures in the different shape of ellipsoid. Subfigures (a), (b), and (c) represent the linear, planar, and spherical diffusion cases respectively. 7
1.4 Relationship between anisotropic diffusion (upper row), diffusion ellipsoids (middle row), and diffusion tensor (bottom row). When environment is isotropic (a), water diffuses equivalently in all directions. The diffusion ellipsoid of this system is spherical and can be depicted by one diffusion constant, D. When the environment is anisotropic, e.g. cylindrical (b,c), water diffusion has directionality. The diffusion ellipsoid of water in a cylinder is elongated and has three principal axes, λ_1, λ_2, and λ_3. To fully characterize such a system, 3 by 3 tensor is needed and the values of the nine elements depend on the orientation of the principal axes. (Taken from [20]) 15
1.5 A brain dissection showing the structure of white matter (Taken from the online library of the Virtual Hospital, University of Iowa) 16
1.6 An illustration of reconstructed white matter tracts by following the direction of maximum diffusion. 17

2.1 The right cingulum bundle mask (red) overlapped on an FA indexed color map. The ROI is in blue and is the starting point of the geodesic distance mapping. 21
2.2 Isonode association. In the left-hand side subfigure, a group of isonodes are assigned one distinct color and circled. The bottom starting point plane is blue. The right-hand side subfigure depicts the parameterized GCC fiber bundle. Fiber tracts are in red and a series of isonodes are in yellow. Isonodes are sparsely spread for illustration purpose. The middle blue plane represents the common starting points. Geodesic distances are calculated bi-directionally originating from the starting point plane. 23
2.3 The left cingulum bundle mask overlapped on the FA value indexed color map. The ROI is in blue and is the starting point of the geodesic path mapping. The yellow color illustrates the region which shows significant FA value reduction in MCIs compared with the control subjects. 27
2.4 Regional FA distribution along the left cingulum bundle in MCIs. The left subfigure illustrates the regional FA value distributions of the control and MCI groups along the geodesic path. The right subfigure gives the p values of the student t-test along the geodesic path. 28
2.5 Left cingulum fiber bundle covered voxels overlapped on an FA indexed color map. Voxels are rendered in wireframe and their colors ranging from blue to red are in accordance with FA values from 0 to 1. Voxels with significant FA degradation are in yellow. 29

2.6 The left subfigure shows the FA value distribution of the 17 connected voxels for both the control and MCI groups. The right subfigure depicts the p values after the student t-test along the geodesic path. 30
2.7 The reconstructed GCC fiber tracts overlapped on a tensor averaged FA map of all subjects. Subfigures (a) and (b) show the GCC bundle in sagittal and axial views respectively. 31
2.8 Scatter plots of the averaged FA (left) and MD (right) values of the entire volumetric region of GCC bundle in normal control and amnestic MCI subjects. The unit of MD is (mm^2/sec). 32
2.9 Statistical analysis of regional micro structural FA and MD alterations along the GCC paths. Negative and positive geodesic indices are in accordance with the left and right parts of the starting point plane (indexed by 0) in Figure 2.2's right-hand side subfigure. The geodesic distance unit is $0.5mm$. The unit of MD is mm^2/sec. 33
2.10 Visualizations of regional micro structural FA (left) and MD (right) alterations along the GCC bundle. Revealed regions with significant FA degradation and MD elevation in MCI subjects are rendered in their according p value indexed colors. p values greater than 0.06 were rendered as 0.06 for simplicity. 34

3.1 Graphical illustrations of the two step reconstruction scheme resulted in forward and backward subpartitions. Arrows in in the two substreamlines in (a) represent local primary eigenvectors in the two reconstruction steps respectively. The backward substreamline is reconstructed by reversing all principal eigenvectors. In (b), the starting points to reconstruct the tract bundle are in blue. The two fiber bundles in distinct colors represent the forward and backward substreamlines respectively. 41
3.2 Illustration of the global diffusion orientation used to distinguish two curves sharing a common geometric center. The black solid and red dotted curves, s_1 and s_2, share a common geometric center c_1 or c_2. The two black dotted lines represent the two global diffusion orientations of s_1 and s_2 respectively. s_1 and s_2 can be identified with the help of their global diffusion orientations if $\alpha \neq 0$. 42
3.3 Illustration of two streamlines s_1 and s_2, their geometric centers, local and global diffusion orientations. Two geometric centers, c_1 and c_2, are marked as solid circles. Arrows of straight line segments indicate one of the two possible diffusion directions. β_i is the angle between the i-th pair of corresponding segments of the two compared streamlines. α is the angle between the two global diffusion orientations. Each streamline's global diffusion orientation is parallel to the linear line directly connecting its two end points. Lengths of s_1 and s_2 are both 4 (4 linear segments). 57

3.4 Demonstration of the advantage of the signed cosine value over the absolute cosine value. Three streamlines, s_1, s_2 and s_3, all have a length of 7. The numbers represent the indices of streamline segments. Arrows represent local primary eigenvectors. s_1, s_2 and s_3 move in the same direction at the beginning. s_1 and s_2 terminate in the same direction while s_3 turns into the opposite direction. 58
3.5 Demonstration of the affinity scores of the two components, S_l and S_g, of PWOSS affected by different relationships between a streamline pair. In subfigure (b), the solid circle is the geometric center of both streamlines. The dotted line represents their global diffusion orientations. 58
3.6 Illustration of multiple streamline bundles sharing no common ROI. 59
3.7 Graphical illustration of substreamline correspondences. In (a), the two end points of streamline s_1, $(p_{11},\ p_{12})$, are close to two different end points of streamline s_2. In (b), both of the two end points of s_1 are close to a common end point of s_2, i.e., p_{21}. $(s_{1f} \leftrightarrow s_{2f},\ s_{1b} \leftrightarrow s_{2b})$ is the substreamline correspondence for both (a) and (b). 59
3.8 The CST-MCP compound trajectories and two clustered sub-bundles. (a) is the original tracts before clustering. (b) shows the separated two subgroups, CST and MCP, in two different colors. $\sigma = 100$ and the PWOSS threshold is 0.5. $\omega = 0.5$. 60
3.9 Histograms of the calculated PWOSSs for the CST-MCP tracts bundling. $\sigma = 100$ and the PWOSS threshold is 0.5. $\omega = 0.5$. (a) shows the calculated PWOSS histogram based on Equation 4.12 for the CST-MCP tracts. The inter and intra cluster PWOSS histograms after clustering are illustrated in (b) 60
3.10 Classification of the CST into two subbundles. (a) shows the two CST subbundles, short and long CST, in two different colors. $\sigma = 100$ and the PWOSS threshold is 0.95. $\omega = 0.5$. (b) is the clustered 3 bundles from the original tracts in subfigure (a). 61
3.11 $\sigma = 100$ and $\omega = 0.5$. (b) shows that the local similarity score contributes more than that of the global affinity score in the classification. 61
3.12 PWOSS, local and global similarity histograms of the CST-CPT-PTR compound tracts. The PWOSS score suggests the similarity thresholds to classify the tracts into two or three sub-bundles. $\sigma = 30$ and $\omega = 0.5$. 62
3.13 Partitions of the CST-CPT-PTR compound tracts into two and three sub-bundles. $\sigma = 30$ and $\omega = 0.5$ for both (a) and (b). 62
3.14 Effects of different σ values on the PWOSS for the CST-CPT-PTR composite tracts. The PWOSS histograms keep almost unchanged for $\sigma \geq 20$. . 63

4.1 Illustration of the clustering result of CST-MCP tract collection in a sagittal view. $\omega = 1.0$ and $\sigma = 1$. The number of the input fiber tracts is 307. The resulting CST and MCP bundles have 199 and 108 tracts each. 72
4.2 Fourier descriptors derived from the center shifted coordinates. $f(2)$ to $f(29)$ are used in clustering. 73
4.3 Fourier descriptors derived from the central distance. $f(1)$ to $f(29)$ are used in clustering. 74

4.4 Fourier descriptors derived from the central angle dot product. $f(1)$ to $f(29)$ are used in clustering. 75
4.5 Illustration of the clustering result of tracts composed of total 13 clusters in different colors. Fourier descriptors are derived from the center shifted coordinates shape signature. $\omega = 0.5$ and $\sigma = 20$. $f(2)$ to $f(29)$ were used for clustering. The number of input tracts is 1379 and 1341 of them are grouped into 13 clusters. Clusters with less than 10 fiber tracts are ignored. 76

5.1 Two angle's views of the symmetric property of tract bundles. The mid sagittal corpus callosum plan is covered by a mask. The symmetric fiber bundles are colored by the overlapped FA values at step points along tracts. The bottom color bars indicate correspondences between colors and FA values. 85
5.2 Sagittal view of the mid-sagittal corpus callosum plan and the geometric center of its bounding box. In the right subfigure, the purple ball represents the the geometric center of the bounding box of the mid-sagittal corpus callosum plan. A mask is placed on the mid-sagittal corpus callosum in the right subfigure. 86
5.3 Illustration of the distance between two geometric centers. The left subfigure is the coronal view of the mid-sagittal corpus callosum plan mask and the geometric center of its bounding box. The small purple ball in the right subfigure represents the geometric center of the fiber tract shown in the graph. The distance between the geometric center of the reconstructed white matter tract and the geometric center of the bounding box of the mid-sagittal corpus callosum plan is depicted by the double arrowed yellow straight line. 87
5.4 Illustration of the clustering results with well defined input tracts. Subfiger (a) shows the input reconstructed white matter tracts. Subfiger (b) demonstrates the clustering results which are seven separated tract bundles colored differently. 93
5.5 Illustration of the clustering result on totally $23,770$ reconstructed white matter tracts. Subfigure (a) shows the tracts before clustering. Subfigure (b) gives the clustered tracts including 18 tract bundles and $9,220$ outliers. Subfigures (c), (d), and (e) demonstrates the 18 tract bundles viewed in three different angles. Subfigure (f) illustrates the $9,220$ tracts labeled as outliers. 94
5.6 Visual comparisons of the performance of combined and uncombined FD methods in reconstructed white matter tract clustering. Subfigures (a), (c), and (e) are the clustering results with the uncombined FD approach. Subfigures (b), (d), and (f) are the clustering results of the same tract bundles using the combined FD method. 96

5.7 Comparisons with the K-means clustering algorithm on a same set of reconstructed white matter. Subfigures (a) and (b) are all the clustered tract bundles by the proposed method and K-means respectively. Subfigures (c) and (c) show the specific tract bundle which has the biggest difference between these two algorithm. The four subfigures in the second last row are the clustering results using K-means. The bottom row are the corresponding results of the proposed method. 98
5.8 Illustration of the impact of the number of Fourier descriptors on tract clustering. Subfigure (a) demonstrates the clustering result including 1216 tracts which are segmented into one single bundle with 9 Fourier descriptors. Subfigure (b) is the separated tracts after using 12 Fourier descriptors. The red color 983 tracts are labeled into one tract bundle. The rest 233 tracts in another color are labeled as outliers 99
5.9 Graphical illustration of the time cost with different setting of π values. The graph indicates that the time cost of unequal values of π is higher than that of equal values of π. 100
5.10 Illustration of some initial target fiber bundles used to initialize the EM algorithm. 101

6.1 Illustration of the clustering result using NMF technique. Subfigure (a) shows the reconstructed white matter tracts before clustering. Subfigure (b) demonstrates the two labeled bundles. The separated CST and MCP bundles are colored in red and light blue respectively. 110
6.2 Value comparisons of elements in the first 10 columns of matrix H. Red: labeled as CST; Blue: labeled as MCP; +: first row; o: second row. Elements in the first and last three columns of the first row, which are colored in red, have larger values than that of the elements in the second row. The six tracts corresponding to these six matrix elements are labeled as CST. On the other hand, the four elements of the mid four columns of the second row which are colored in blue, have larger values than that of the elements in the first row. The four tracts corresponding to these four matrix elements are labeled into MCP bundle 111
6.3 Illustration of the classified first 10 fiber tracts rendered in different colors.The red color six tracts are in correspondence with the six first row matrix entries of the first and last three columns in Figure 6.2. The four light blue colored tracts are in correspondence with the four second row matrix elements of the mid four columns in Figure 6.2. 112

List of Files

1.1 dissertation.pdf xii

1 Introduction

This dissertation presents algorithms to estimate regional white matter alterations in human brains along neural pathways in 3D space, relying on white matter tractography and geodesic distance mapping. It also develops a new class of modeling and clustering techniques for separating reconstructed white matter fibers.

1.1 Diffusion Tensor Imaging

The development of Magnetic Resonance Imaging (MRI) has led to the design of numerous imaging techniques [1, 2, 3]. One of these technologies is Diffusion Tensor Imaging (DTI), which measures the motion of hydrogen atoms within water molecules in all three dimensions [4, 5]. In tissues containing a large number of fibers, like the white matter in human brains, water tends to diffuse mainly along the direction of the fibers [6, 7, 8, 9, 10, 11]. DTI gives us such complex information about how water diffuses in tissues into intricate three-dimensional representations of the tissues [12, 13]. This is particularly informative when imaging fibrous tissues, such as tendons and ligaments [14, 15, 16]. The ability to measure the different rates of diffusion along different directions is one of the features that distinguish DTI from other imaging methods and makes it especially useful for studying the directional qualities of brain tissue [5, 17].

DTI is the only means currently available for *in vivo* investigation of human brain connectivity and one of a few available for studying brain functions [18]. It is emerging as an important technology for elucidating the internal structure of the brain and for diagnosing conditions affecting the integrity of neural tissues. DTI measurements of the brain exploit the fact that the network of neural fibers has a characteristic microstructure that constrains the diffusion of water molecules within it. The direction of the fastest diffusion is aligned with fiber orientation in a pattern that can be numerically modeled by a diffusion tensor. The DTI technique has raised hopes in the neuroscience community for a better understand-

ing of the white matter tract anatomy of the human brain [19, 20]. Knowledge about fiber tract connections within and across individual brains should enhance our understanding of normal brain functions. Such knowledge should also help diagnose certain brain disorders and abnormalities such as edema (swelling), ischemia (brain damage from restricted blood flow), multiple sclerosis, schizophrenia, Alzheimer's disease and certain types of brain tumors [21, 22]. Furthermore, an understanding of white matter structure could help us to avoid damaging important nerve pathways in surgeries. Various methods have been proposed to use DTI data to track nerve fibers and derive connectivity between different parts of the brain [23, 24, 25].

1.1.1 Basics of DTI

DTI is an extension of conventional MRI with signal intensities sensitized to the random motion of water molecules. The phenomenon of water molecule diffusion is commonly referred to as "Brownian motion". In an isotropic liquid the probability that a molecule covers the distance r during time t follows a Gaussian law with variance $6ct$, where c is the diffusion coefficient that characterizes the molecule mobility. In an anisotropic environment, the mobility is different along different directions in space. Hence, diffusion is a three dimensional process which can be modeled by a second order 3-by-3 tensor. This tensor is an intrinsic property of the tissue and is represented by a matrix D, which is symmetric, positive and real. The diffusion coefficient in any direction d is given by the tensorial dot product [20]:

$$c(d) = d^T D d = d d^T \cdot D \tag{1.1}$$

$$D = \begin{pmatrix} D_{xx} & D_{xy} & D_{xz} \\ D_{yx} & D_{yy} & D_{yz} \\ D_{zx} & D_{zy} & D_{zz} \end{pmatrix} \tag{1.2}$$

This second order diffusion tensor can be visualized as an ellipsoid as shown in Figure 1.1.

According to the tensor theory, if we measure the diffusion constant along at least six

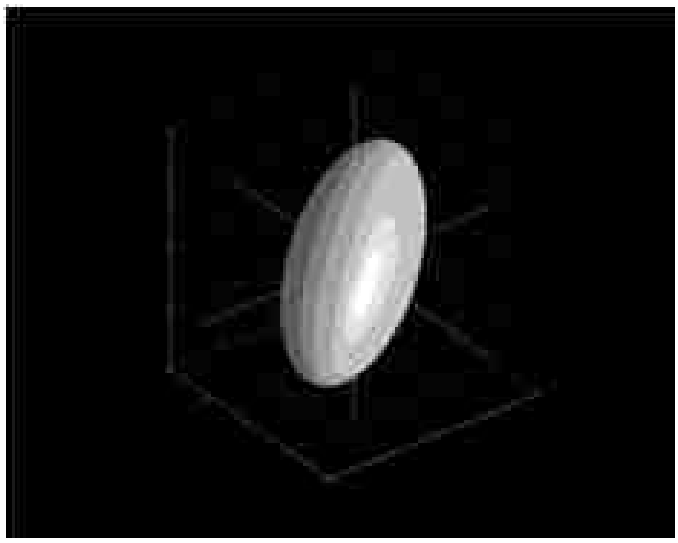

Figure 1.1: Illustration of a second order diffusion tensor represented as an ellipsoid.

independent axes, we can calculate the complete shape of the diffusion ellipsoid [42, 31, 43].

1.1.2 Diffusion Tensor Calculation

Tensors are usually categorized with respect to their order. A tensor of order 0 is simply a scalar, a tensor of order 1 is a vector and a tensor of order 2 can be represented by an n-by-n matrix. In DTI each voxel contains a $2nd$ order tensor representing the diffusion in each voxel. The tensor is written as a 3-by-3 matrix as seen in Equation 1.2.

To determine the diffusion tensor completely, we must first collect diffusion-weighted images along several gradient directions, using diffusion-sensitized MRI pulse sequences [41] such as echoplanar imaging (EPI). As the diffusion tensor is symmetric, measurements along only six directions are mandatory.

The MR signal is usually corrupted by water molecule diffusion, which disturbs the spin technique described earlier, leading to a small decrease of the measured signal. In diffusion imaging, this effect is magnified by making use of the strongest possible magnetic field gradient applied in one direction d. For each slice, six images are separately collected with different diffusion weightings and gradient pulses. Each gradient pulse is typically

applied for duration of several tenths of a millisecond, during which time the average water molecule in brain tissue may migrate 10 or more micrometers in a random direction. The irregularity of the motion entails a signal loss that can be used to quantify the diffusion constant. If S_0 represents the signal intensity in the absence of a diffusion sensitizing field gradient pulse and S, the signal intensity, in the presence of a gradient pulse $g = (g_x, g_y, g_z)^T$, the equation for the loss in signal intensity due to diffusion is given by the Stejskal-Tanner formula [20, 19]:

$$ln(S) = ln(S_0) - \gamma^2\delta^2(\Delta - \delta/3)g^T Dg \tag{1.3}$$

where γ is the proton gyromagnetic ratio of (42MHz/Tesla), δ is the duration of the diffusion sensitizing gradient pulse and Δ is the time between the centers of the two gradient pulses. The six separately acquired images provide six equations for S in each voxel. The equations are solved in a least-squares sense for the six unknowns, which correspond to the six independent components of the symmetric diffusion tensor in Equation 1.2.

Corresponding to the original signal intensity S_0, the image collected in the absence of gradient pulses is referred to as the base line image. These base line images are inherently acquired as part of the acquisition sequence. And they can be used to register individual data into standard anatomical space. Figure 1.2 demonstrates the above mentioned six images plus the base line image generated in the process of diffusion imaging acquisition. They are shown in axial, sagittal, and coronal views respectively. In this example, the six gradient pulses applied in the image acquisition are $(0.707, 0.707, 0.000)$, $(-0.707, 0.707, 0.000)$, $(0.000, 0.707, 0.707)$, $(0.000, -0.707, 0.707)$, $(0.707, 0.000, 0.707)$, and $(-0.707, 0.000, 0.707)$.

One of the fundamental problems in understanding and working with diffusion tensor data is its three dimensional and multi-variate nature. Each sample point in a DTI scan can be represented by six inter-related values, and many features of interest are described in terms of derived scalar and vector fields, which are logically overlayed on the original tensor field.

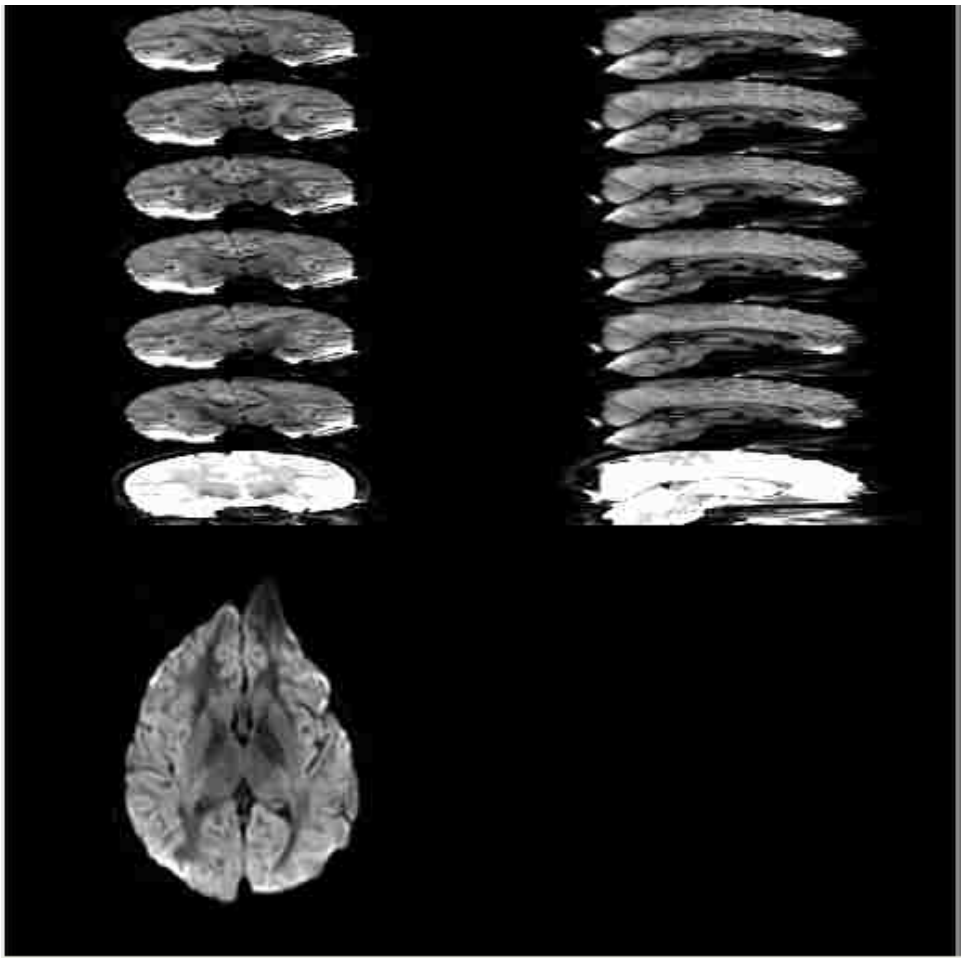

Figure 1.2: Illustration of the six gradient applied images and the base line image used to estimate diffusion tensor. Images are shown in axial, sagittal, and coronal views respectively.

After the complete determination of diffusion tensor D, a series of quantitative diffusion indices can be derived from D.

1.1.3 Quantitative Diffusion Properties

The Eigensystem of The Diffusion Tensor

Since second order tensors can be represented by a matrix, they can also be decomposed into eigenvalues and eigenvectors. An eigenvector x to diffusion tensor D and its corresponding eigenvalue λ have the property that the inner product of the original tensor and the

eigenvector result in a vector that is a scalar multiple of the original eigenvector [20, 19]:

$$Dx = \lambda x, \qquad x \neq 0 \tag{1.4}$$

The solutions λ_i to Equation 1.4 are the eigenvalues of D. The vectors x_i associated with each eigenvalue are the eigenvectors of D. Since the null vector is omitted Equation 1.4 can be re-written as $(D - \lambda I)x = 0$, where I represents the identity matrix. This implies that the matrix $D - \lambda I$ is singular and its determinant is zero, which corresponds to the eigenvalues being the solutions to the secular equation:

$$|D - \lambda I| = 0 \tag{1.5}$$

For each eigenvalue λ the corresponding eigenvector x can be found by solving

$$(D - \lambda I)x = 0 \tag{1.6}$$

The eigenvalue-eigenvector pairs together contain all of the information available in the original tensor. The tensor can be written as a weighted sum of the outer products:

$$D = \sum_{i=1}^{3} \lambda_i x_i x_i^T \tag{1.7}$$

where λ_i and x_i are the eigenvalue and eigenvector pair.

In general the eigenvalues may be real or complex. However, for a real symmetric tensor, like the diffusion tensor, the eigenvalues are always real and the eigenvectors will be orthogonal to each other.

Anisotropy Measures

There are three eigenvalues for the second order diffusion tensor D. They are sorted in descending order in which λ_1 has the largest value and λ_3 has the smallest. The corresponding eigenvectors can be used to represent the principal axes of an ellipsoid. The diffusion can then be divided into three basic cases [20]:

1. Linear case ($\lambda_1 \gg \lambda_2 \approx \lambda_3$): diffusion is mainly in the direction corresponding to the largest eigenvalue. The ellipsoid representation is similar to a cigar as shown in subfigure 1.3(a). And the second order tensor can be approximated by

$$D \approx \lambda_1 D_l = \lambda_1 x_1 x_1^T \tag{1.8}$$

where D_l represents the tensor D in the linear case.

2. Planar case ($\lambda_1 \approx \lambda_2 \gg \lambda_3$): diffusion is restricted to a plane spanned by the two eigenvectors corresponding to the two largest eigenvalues. The ellipsoid representation is illustrated in subfigure 1.3(b). The second order tensor can be approximated by

$$D \approx 2\lambda_1 D_p = \lambda_1 (x_1 x_1^T + x_2 x_2^T) \tag{1.9}$$

where D_p represents the tensor D in the planar case.

3. Spherical case ($\lambda_1 \approx \lambda_2 \approx \lambda_3$): isotropic diffusion as illustrated in subfigure 1.3(c). The second order tensor can be approximated by

$$D \approx 3\lambda_1 D_s = \lambda_1 (x_1 x_1^T + x_2 x_2^T + x_3 x_3^T) \tag{1.10}$$

where D_s represents the tensor D in the spherical case.

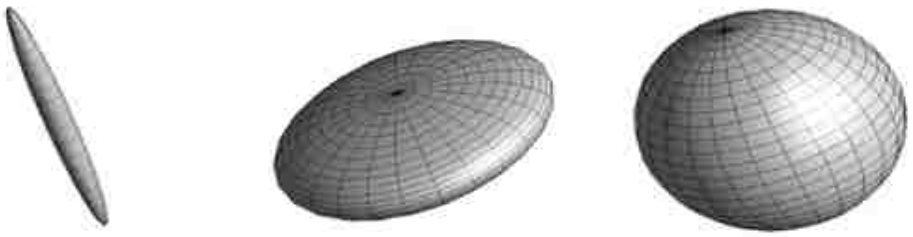

(a) Linear: $\lambda_1 \gg \lambda_2 \approx \lambda_3$ (b) Planar: $\lambda_1 \approx \lambda_2 \gg \lambda_3$ (c) Spherical: $\lambda_1 \approx \lambda_2 \approx \lambda_3$

Figure 1.3: Illustration of anisotropy measures in the different shape of ellipsoid. Subfigures (a), (b), and (c) represent the linear, planar, and spherical diffusion cases respectively.

It is possible to write the general diffusion tensor D as a linear combination of these three cases:

$$\begin{aligned} D &= \lambda_1 x_1 x_1^T + \lambda_2 x_2 x_2^T + \lambda_3 x_3 x_3^T \\ &= (\lambda_1 - \lambda_2) x_1 x_1^T + (\lambda_2 - \lambda_3)(x_1 x_1^T + x_2 x_2^T) + \lambda_3 (x_1 x_1^T + x_2 x_2^T + x_3 x_3^T) \\ &= (\lambda_1 - \lambda_2) D_l + (\lambda_2 - \lambda_3) D_p + \lambda_3 D_s \end{aligned} \tag{1.11}$$

where $(\lambda_1 - \lambda_2)$, $(\lambda_2 - \lambda_3)$, and λ_3 can be viewed as the coordinates of D in the tensor basis D_l, D_p, and D_s. By using the coordinates of the tensor in our new basis, measures can be obtained of how close the diffusion tensor is to the generic cases of line, plane and sphere. The generic shape of a tensor is obtained by normalization with a magnitude measure of the diffusion. The magnitude is here defined as the trace of the tensor, normalizing the sum of the measurements to 1. For the linear, planar and spherical measures this gives [20, 19]:

$$c_l = \frac{\lambda_1 - \lambda_2}{\lambda_1 + \lambda_2 + \lambda_3} \tag{1.12}$$

$$c_p = \frac{2(\lambda_2 - \lambda_3)}{\lambda_1 + \lambda_2 + \lambda_3} \tag{1.13}$$

$$c_s = \frac{3\lambda_3}{\lambda_1 + \lambda_2 + \lambda_3} \tag{1.14}$$

and

$$c_l + c_p + c_s = 1 \tag{1.15}$$

An anisotropy measure c_a describing the deviation from the spherical case is achieved as follows:

$$c_a = c_l + c_p = 1 - c_s = \frac{\lambda_1 + \lambda_2 - 2\lambda_3}{\lambda_1 + \lambda_2 + \lambda_3} \tag{1.16}$$

Figure 1.4 which is taken from [20] demonstrates the relationship between anisotropic diffusion (upper row), diffusion ellipsoids (middle row), and diffusion tensor (bottom row).

Mean Diffusivity

Mean Diffusivity (MD) is designed as a scalar value for overall evaluation of the diffusion in a voxel or region. For this purpose, we must avoid anisotropic diffusion effects and

limit the result to an invariant. MD is such an invariant quantity that is independent of the orientation of the reference frame [31]. MD measures the bulk mean motion of water and can be used to study pathological changes in cerebral tissue [19].

After the diffusion tensor D is completely determined, the trace of D is available as

$$Tr(D) = D_{xx} + D_{yy} + D_{zz} \tag{1.17}$$

MD is then given by $Tr(D)/3$. D_{xx}, D_{yy}, and D_{zz} are the three diagonal elements of diffusion tensor D as shown in Equation 1.2. MD has been proved useful in assessing the diffusion drop in brain ischemia [40].

Fractional Anisotropy

The general diffusion tensor was then diagonalized, yielding eigenvalues λ_1, λ_2, and λ_3, as well as eigenvectors x_1, x_2, and x_3 that define the predominant diffusion direction. Eigenvalues λ_1, λ_2, and λ_3 are combined differently to make a number of invariant diffusion indices. Based on eigenvalues, the fractional anisotropy (FA) can be calculated on a voxel-by-voxel basis. As a diffusion tensor-derived quantitative measure of white matter tissue diffusion anisotropy in each voxel, FA characterizes the micro architecture of local brain tissue, and is sensitive to the integrity and alterations of neuronal connectivity in white matter [26]. FA summarizes the anisotropy of the ellipsoid representation for diffusion. Its value varies between zero and one. An FA of zero indicates the spherical diffusion illustrated in subfigure 1.3(c), as is found in the brain gray matter. As FA increases, the diffusion becomes more anisotropic. FA values near 0.5 indicate either linear (cigar shaped) or planar (pancake shaped) ellipsoids as shown in subfigures 1.3(a) and 1.3(b). They are typically found in the brain white matter. As FA approaches 1, the diffusion becomes increasingly linear, indicated by long and thin ellipsoids.

FA is one of most commonly used anisotropy index and is calculated by [5]

$$FA = \sqrt{\frac{3}{2}}\sqrt{\frac{(\lambda_1 - \overline{\lambda})^2 + (\lambda_2 - \overline{\lambda})^2 + (\lambda_3 - \overline{\lambda})^2}{\lambda_1^2 + \lambda_2^2 + \lambda_3^2}} \tag{1.18}$$

where $\overline{\lambda}$ is formed by

$$\overline{\lambda} = \frac{\lambda_1 + \lambda_2 + \lambda 3}{3} \tag{1.19}$$

1.2 White Matter Tractography and Neuroscience Applications

Most developments in MRI since 1993 have been refinements and improvements on existing imaging technologies, but some have been spectacular, such as diffusion tensor tractography. With DTI datasets, the white matter fibers can be reconstructed using a class of techniques called tractography [27, 34, 35, 37, 38]. DTI and white matter tractography play a crucial role in understanding anatomical connectivity and functional coupling between regions of the brain, and in clinical applications such as neurosurgery planning and brain disorder diagnosis [30, 32, 33].

The invasive methods have been used in the connectivity studies in animal brains cannot be used for humans. Post mortem studies of fiber bundles are possible for human brains, for instance by observing passive diffusion using chemical dyes, but can take months to perform and are often affected by cross fiber diffusion. Post mortem methods have revealed that white matter in the human brain is highly structured, which can be seen in Figure 1.5. However, using conventional MRI protocols, such as T1 and T2, white matter appears to be homogeneous. Only recently, by the introduction of DTI, in vivo studies of the human brain white matter tract anatomy have become possible.

In DTI the diffusion of water molecules is measured in different directions. This measure can be related to nerve fibers by the fact that water tends to diffuse only along the fibers, because tightly packed myelin membranes restricts diffusion perpendicular to the axons. Myelin is not essential for anisotropic diffusion in fiber tracts, as shown in studies of nonmyelinated garfish olfactory nerves and neonates human brains, but is widely assumed to be the main barrier for water diffusion [44]. The eigenvector corresponding to the largest eigenvalue of the diffusion tensor often gives a good estimate of the local fiber orientation inside a voxel. A simple but effective method for fiber tracking is to simply

follow the direction of maximum diffusion, as seen in Figure 1.6.

DTI and white matter tractography techniques have raised hopes in the neuroscience community for a better understanding of the fiber tract anatomy of the human brain. It is known that anisotropic diffusion in white matter reveals micro structural properties of the anatomy of neural pathways as water tends to diffuse along the axons [45, 46, 47, 48]. A variety of methods have been proposed to use DTI data and white matter tractography to track brain neural fibers [49, 50, 52] and detect a number of brain abnormalities [32, 33, 36, 51, 53, 60].

1.3 Tractography Algorithm and DTI Data Acquisition

1.3.1 Tractography Algorithm

A number of tractography algorithms have been proposed since the advent of DTI. The common algorithms include Principal Diffusion Direction (PDD) Tracking [27, 38, 55, 57], Solving the Diffusion Equation [35, 37, 49], Fast Marching Tractography [59], and Markov Random Field Regularization [47]. The tractography method employed in this dissertation is streamline based tracking technique [56] and falls into the PDD category. The reconstructed white matter tracts are streamlines.

DTI data calculations and experiments in this dissertation are performed using software developed in our lab which is based on OpenGL [61], VTK [63], and MFC on the Windows platform.

1.3.2 DTI Data Acquisition

The detailed description of the DTI data acquisition procedure can be found in Dr. Rose's work [23]. The following is the brief summary of the process.

All DTI data were collected with a 1.5T Siemens Sonata scanner using an optimized diffusion tensor sequence [81].The imaging parameters were 48 axial slices, FOV $= 230mm$, TR = $6000ms$, TE = $106ms$, $2.5mm$ slice thickness with $0.25mm$ gap, acquisition matrix 128×128 and 60 images acquired at each location consisting of 16 low ($b = 0$) and

44 high diffusion-weighted images in which the encoding gradient vectors are uniformly distributed in space ($b = 1100s/mm^2$) using the electrostatic approach described elsewhere [81]. The reconstruction matrix was 256×256, resulting in an in-plane resolution of $0.898 \times 0.898mm^2$. The total scan time was 8 minutes. The diffusion tensor was calculated according to the Stejskal-Tanner equation. The resolution of the original calculated tensor data volume was $256 \times 256 \times 48$ with a voxel size of $0.898 \times 0.898 \times 2.75mm^3$ defined on a Cartesian mesh.

A rigorous non-linear registration was performed for all DTI data. They were registered into the same anatomical space by means of their base images. The reason to do this is that the same DTI data were also used for studies conducting voxel-by-voxel statistical comparisons. This process is unnecessary for DTI studies in this dissertation. In the registration, normalized base line images were non-linearly registered using mutual information to the MNI (Montreal Neurological Institute) template known as the ICBM152 [83]. A hierarchical fitting strategy with a minimum step size of $2mm$ was used for this registration procedure [84]. A two-sample t-test was performed to determine significant difference between the two subject groups. Statistical significance, corrected for multiple comparisons, was determined using Gaussian random field theory employing a blurring kernel of $5mm$ (fwhm) [85]. A t-value greater than 4.095 was considered significant ($p < 0.001$). Voxels from the MD and FA maps with a t-value greater than 4.096 were automatically extracted and classified automatically as a ROI when 20 or more voxels were contiguous. Pearson correlation coefficients calculated across both subject groups for each generated ROI were used to determine the relationship between MD and FA measure and neuropsychological assessment scores. Bonferroni correction for multiple comparisons was applied to maintain the total Type 1 error rate at a sufficient level. In this case, only corrected correlations of $p < 0.01$ were considered statistically significant. The mean diffusivity measure from each ROI was used to derive the correlation coefficients.

1.4 Organization of the Dissertation

Given this background, we now turn to our research, which focuses on several key areas in making DTI based tractography a useful probe of neural connectivity. In doing so, it provides new results relating to computing and clustering of white matter tracts in human brain.

Specifically, the major contributions of this dissertation are:

- The implementation of a computational and visual analysis framework for examining the micro structural white matter alterations along neural pathways in 3D space;
- The development of a Fourier descriptor model with improved noise resistance and palliated computational load in clustering a large amount of reconstructed white matter tracts;
- The implementation of a clustering algorithm with enhanced robustness and improved anatomical accuracy in grouping a large amount of reconstructed fiber tracts to facilitate clinical group analysis;
- The implementation of a more practical and efficient modeling and clustering scheme for separating a small amount of reconstructed white matter tracts;
- The evaluation of the performance of the nonnegative matrix factorization technique in clustering reconstructed white matter tracts;

The dissertation is organized as follows. Chapter 2 introduces in detail a computing framework for quantitative and visual analysis of micro structural white matter changes along neural pathways in human brain. Real DTI data including normal controls and patients with amnestic mild cognitive impairment are used to evaluate the proposed methods. We present the modeling and clustering scheme for separating a small amount of reconstructed white matter fibers in Chapter 3. Chapter 4 focuses on the Fourier descriptor

model for white matter tract representation which boosts the computation efficiency and noise resistance in the context of whole brain white matter tractography. In Chapter 5, we deliver a clustering algorithm with improved anatomical accuracy in dealing with a large amount of white matter tracts to facilitate clinical group analysis. The evaluation on performance of nonnegative matrix factorization technique in clustering reconstructed white matter tracts is conducted in Chapter 6. A summary of this dissertation and some remarks for the future work are given in Chapter 7.

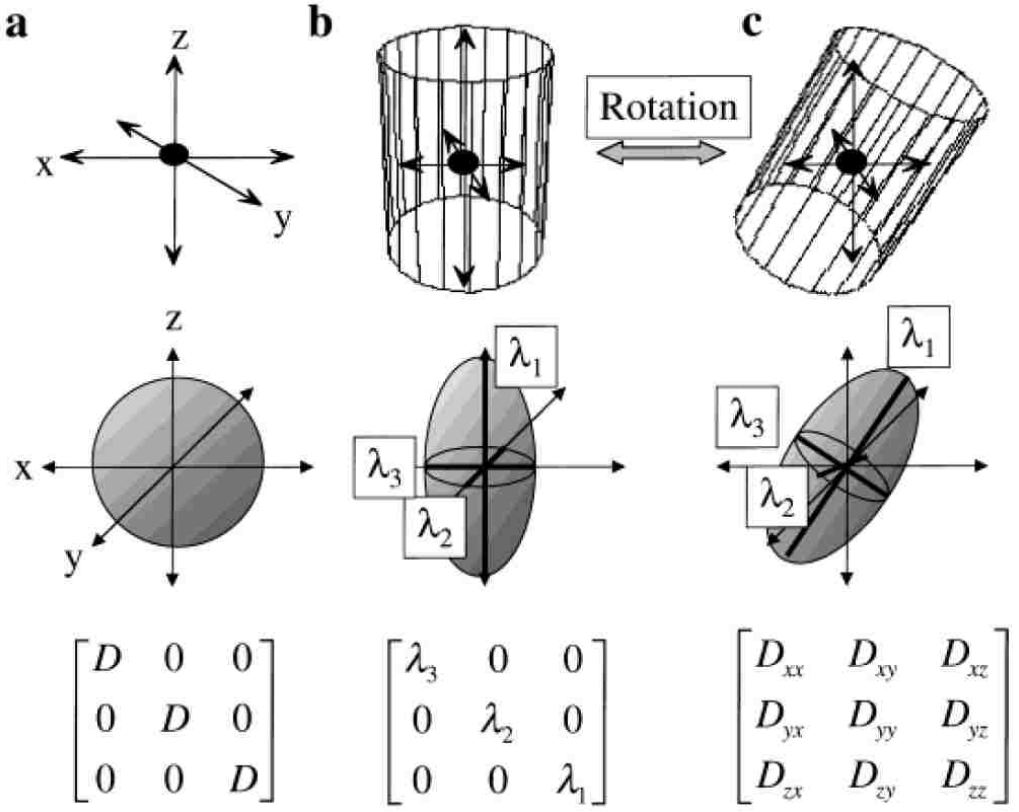

(a)

Figure 1.4: Relationship between anisotropic diffusion (upper row), diffusion ellipsoids (middle row), and diffusion tensor (bottom row). When environment is isotropic (a), water diffuses equivalently in all directions. The diffusion ellipsoid of this system is spherical and can be depicted by one diffusion constant, D. When the environment is anisotropic, e.g. cylindrical (b,c), water diffusion has directionality. The diffusion ellipsoid of water in a cylinder is elongated and has three principal axes, λ_1, λ_2, and λ_3. To fully characterize such a system, 3 by 3 tensor is needed and the values of the nine elements depend on the orientation of the principal axes. (Taken from [20])

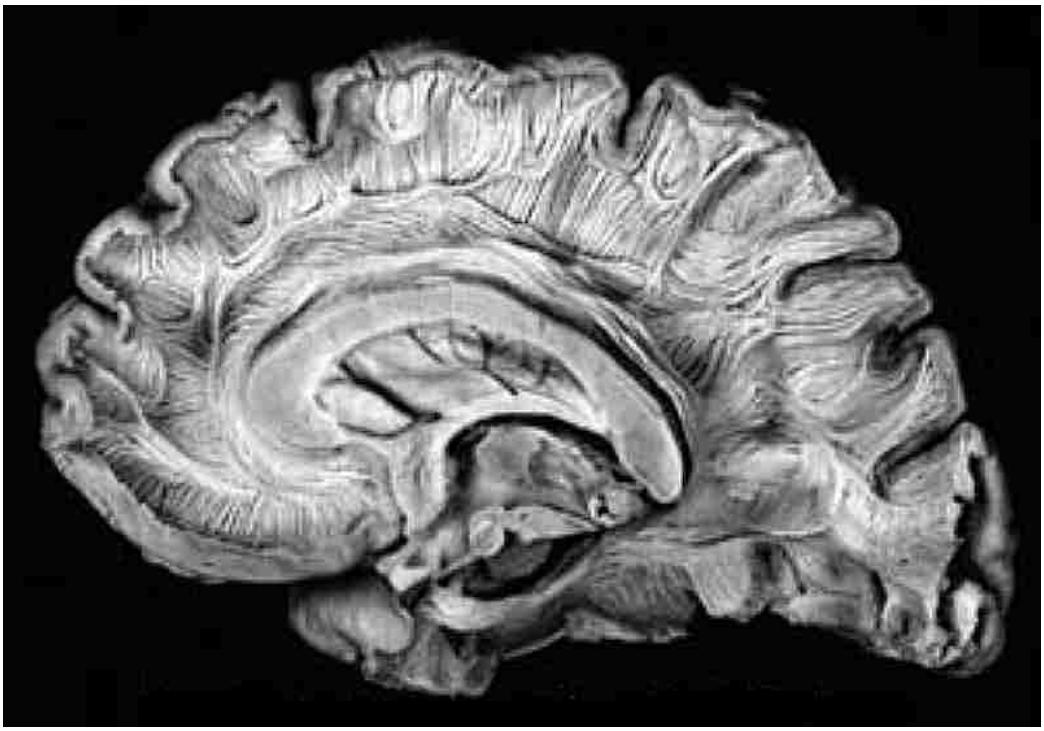

(a)

Figure 1.5: A brain dissection showing the structure of white matter (Taken from the online library of the Virtual Hospital, University of Iowa)

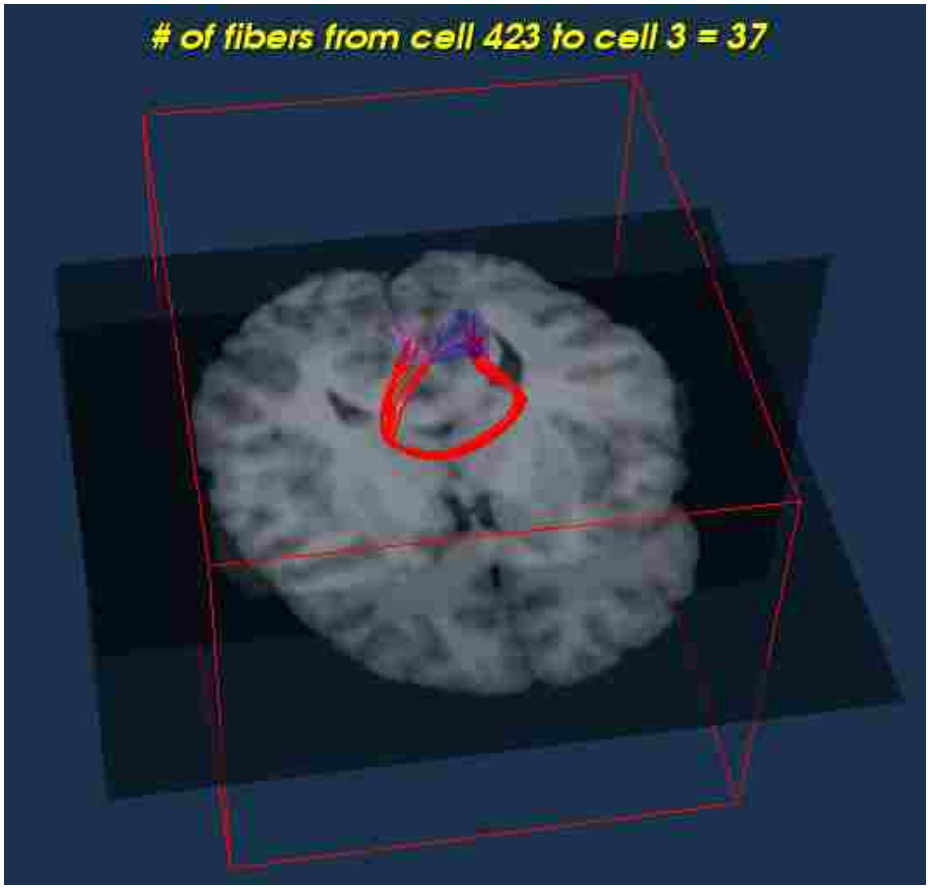

Figure 1.6: An illustration of reconstructed white matter tracts by following the direction of maximum diffusion.

2 Quantitative and Visual Analysis of White Matter Integrity

2.1 Outline

In this chapter, we briefly introduce the background and challenges that motivate us to develop the computing technique. Next, the detailed information about the implementation of the framework is described. Real DTI data experimental results are also presented. Finally, the advantage and limitation of the proposed approach are discussed.

2.2 Introduction

In recent years, developing analysis methods for extracting quantitative information from DTI has received extensive attention. Previously, region-of-interest (ROI) [25] and voxel based morphometry (VBM) [23, 24] techniques have been used in medical literatures for DTI related white matter analysis. But there are known limitations with these approaches [65]. The ROI approach typically measures only one or more prior defined intersections on a white matter fiber bundle and may have difficulty to reflect the white matter changes in the entire volume of a neuronal pathway. It can be subjective and introduce inconsistencies in the placement of ROI among individual studies. Poor reproducibility may be a shortcoming of this method. VBM is a whole-brain, voxel-based automatic method. Its analysis result is voxel-based as well and not directly associated with structural connectivity. With this method, one may be unable to conclude if any explored abnormality happens in a particular anatomical region of a neuronal path. Alternative strategies involving the analysis of diffusivity measures along parts of the computed fiber tracts using scale-invariant parameterizations were proposed [68].

Furthermore, structural and functional MRI studies have reported white and gray matter alterations of a widespread network of regions in human brain [28, 29]. Some of these alterations may be based, in part, on changes to white matter tracts that connect these regions. To explain these regional alterations, neuroscientists are interested in quantitative

evaluations along the specific neuronal network paths. This motivated the development of the tract oriented measuring and analysis approaches. This class of guided analysis techniques is based on DTI tractography and geodesic distance mapping and measures diffusion properties along a reconstructed white matter fiber bundle [32, 33, 62].

The main goals of this study are twofold:

- to develop effective strategies to inspect possible tissue damages caused by regional micro structural white matter changes along the major bundles for both strong and hardly reconstructed fiber tract bundles;
- to interactively visualize hidden regional statistical features along neural pathways *in vivo* for a better understanding of the progression of certain brain diseases;

Our approach is based on DTI white matter tractography and geodesic distance mapping, which establishes correspondences to allow direct cross-subject evaluation of diffusion properties along the tractography-extracted fiber tracts by parameterizing the space of the computed pathways as isonodes, a function of the geodesic distance. For fiber bundles which are very thin, and it is difficult to reconstruct all their entire anatomically valid paths for all subjects in group analysis, we propose the white matter tract mask scheme to overcome this difficulty. The second objective is achieved by employing our proposed isonode visualization scheme. Experiments are conducted to assess the performance of this framework by investigating specific white matter diffusion property changes along three major fiber bundles in patients with the amnestic mild cognitive impairment, compared with the normal control subjects.

2.3 Methods

2.3.1 Fiber Tract Bundle Mask

We use our home-developed software package to process the DTI data and track fibers. The tensor calculation is based on the Stejskal-Tanner equation. The diffusion properties, FA, MD, and eigenvectors of the diffusion tensor, are calculated and saved as image files.

Fiber tracts are reconstructed using the backward streamline tractography technique [39]. This approach treats the entire brain as the tracking source region and only those reconstructed fiber tracts which pass through the predefined ROI (target) are kept. Therefore, one voxel may have more than one fiber tracts passing through and the tracking results are significantly improved [39, 62]. A fixed size ROI, worked as the target region of the fiber tracking, is manually placed in the center area of a fiber bundle to minimize the misregistration effect. As a result, voxels that are around the ventricles and at the edge of a fiber bundle are then excluded. FA indexed color maps are employed to validate the reconstructed fiber tracts.

Limited by the currently available imaging technology, the quality of the DTI data is not sufficiently good for us to reconstruct the full path of certain fiber bundles from each of the subjects. The reason lies in the fact that fiber tracking is susceptible to distortion due to noise and partial volume effects. The volume loss and FA value degradation caused by certain brain diseases, e.g., Alzheimer's disease, contribute to this difficulty as well. An example is the cingulum which is only about one voxel (less than $3mm$) thick. To overcome this difficulty and make the group analysis possible, we instead employ the idea of a fiber tract bundle mask. We reconstruct a fiber tract bundle mask from a tensor averaged image from all control subjects. This tensor averaged image has much less noise and is used to reconstruct anatomically more representative fiber tracts than that of individual subjects. By applying this pre-extracted tractography mask to subjects we evaluate the regional micro white matter abnormalities along fiber bundles in group analysis. In this study, the bilateral cingulum fiber masks are produced in this way and then applied to each DTI data of individual subjects. Figure 2.1 illustrates the right cingulum bundle mask overlapped on a tensor averaged FA indexed color map from all control subjects.

For strong fiber bundles, e.g., the genu of the corpus callosum (GCC) fiber bundle, we perform the fiber tracking for all subjects one by one in their individual spaces.

Figure 2.1: The right cingulum bundle mask (red) overlapped on an FA indexed color map. The ROI is in blue and is the starting point of the geodesic distance mapping.

2.3.2 Geodesics and Geodesic Distance Mapping

Fiber tracts extracted from each individual subject are stored as sets of curvilinear polylines. One fiber tract is a 3D curve $r(s)$ on a Riemannian manifold Ω. The tangent space τ on a Riemannian manifold is equivalent to the vector space of the primary eigenvectors $\overrightarrow{e} = (e_1, e_2, e_3)^T$. To obtain a distance between two points of a connected Riemannian manifold, we have to take the minimum length among the smooth curves joining these points. The curves satisfying this minimum for any two points of the manifold are called geodesics. Geodesic distance of two points c_1 and c_2 on a fiber $r(s)$ is obtained by integrating $\overrightarrow{e}(s)$ along r

$$Dist(c_1, c_2) = \int_{s_1}^{s_2} \overrightarrow{e}(s) ds. \tag{2.1}$$

Let $I = [a, b]$ be an interval on a fiber curve $r(s)$, which is defined as a natural sequence of points $r(s) = (x(s), y(s), z(s))$ or a sequence of point vectors of a moving point on the image set $r(I)$ of curve r. With these definitions, we can now map a fiber $r(s) : \Omega \mapsto [a, b]$ by Equation 2.1. After this mapping, two distinct points on two distinct fibers my share one common geodesic distance $Dist(s)$.

In the implementation, for each fiber bundle (a set of fiber tracts), we set up common starting point region and parameterize each fiber by a fixed geodesic arc-length. These common starting point region and fixed arc-length geodesic path parameterizations estab-

lish correspondences across subjects as well as individual fiber tracts.

2.3.3 Isonodes

To facilitate the use of visual analysis techniques in our research, here we define a new concept, isonodes. Isonodes are a three-dimensional analog of a collection of nodes. They are a group of points of a constant geodesic arc-length within a volume space of fiber tracts. Similar to an isosurface, they form a level set of a continuous function of geodesic distance whose domain is the three-dimensional space.

Isonodes are rendered quickly since they can be displayed as simple points or polygons. They can be used in tractography related volume dataset visualization schemes in medical imaging, allowing researchers to study inherently associated local features along major fiber bundles.

2.3.4 Local Diffusion Property Calculation

Equipped with the above techniques, we model a set of fiber bundles from N subjects as $B = (F_1, \ldots, F_k, \ldots, F_N)$, with the k-th fiber bundle $F_k = (f_1, \ldots, f_i, \ldots, f_n)$ and the i-th fiber $f_i = (d_1, \ldots, d_j, \ldots, d_m)$, where d_j is the j-th node's geodesic distance on the i-th fiber curve from its starting point. In our analysis, diffusion properties are carried as attributes on each node [62]. Then the local diffusion property calculation becomes straightforward by simply associating the isonodes. This is depicted in Figure 2.2 in which isonodes are sparsely illustrated for clarity.

Let Ψ_i be attribute values on the i-th fiber pathway and d_j the geodesic distance of the j-th node in the curvilinear structure. Then the geodesic path for the k-th fiber bundle with average attribute $\overline{\Phi}_k$ is computed as

$$\overline{\Phi}_k(d_j) = \frac{1}{n} \sum_{i=1}^{n} \Psi_i(d_j), j = 1, ..., m. \tag{2.2}$$

We adopted the same scheme of coalescing fiber bundles among subjects for the purpose of group comparisons. The mean attribute value $\overline{\Phi}(d_j)$ across N subjects at the j-th

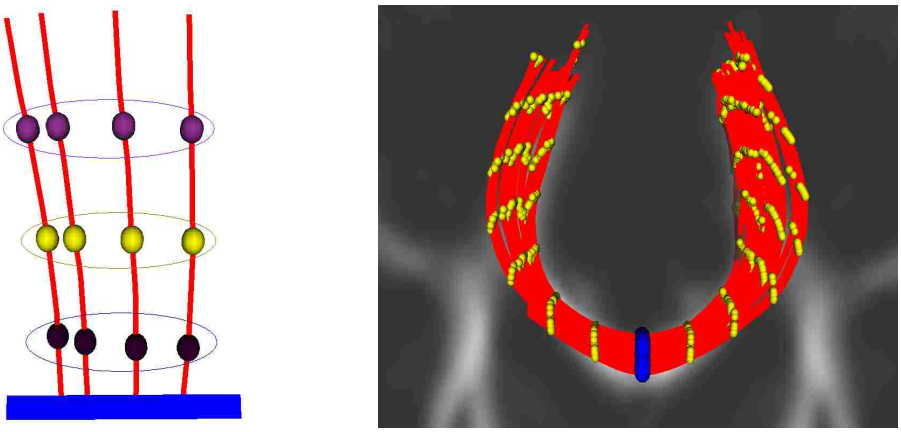

Figure 2.2: Isonode association. In the left-hand side subfigure, a group of isonodes are assigned one distinct color and circled. The bottom starting point plane is blue. The right-hand side subfigure depicts the parameterized GCC fiber bundle. Fiber tracts are in red and a series of isonodes are in yellow. Isonodes are sparsely spread for illustration purpose. The middle blue plane represents the common starting points. Geodesic distances are calculated bi-directionally originating from the starting point plane.

node is

$$\overline{\Phi}(d_j) = \frac{1}{N}\sum_{k=1}^{N}\overline{\Phi}_k(d_j), j = 1, ..., m. \tag{2.3}$$

2.3.5 Isonode Visualization Scheme

Each group of isonodes can be associated with their distinct local statistical feature in addition to their inherent attribute, a unique geodesic arc-length. We render all the calculated isonodes overlapped on the reconstructed fiber paths. In the process, each set of isonodes are positioned by its geodesic distance along the fiber bundles and are color coded by their discovered statistical features. Different color schemes and thresholds can be interactively selected by a user depending on applications and confidence levels to obtain better understanding of the diffusion property changes along the neuronal path.

2.4 Experiments and Results

We illustrate group analysis results of three fiber bundles between amnestic mild cognitive impairment (MCI) subjects and normal controls in this experiment. They are:

- left major cingulum bundle;
- right major cingulum bundle;
- the genu of the corpus callosum (GCC) bundle

The left and right major cingulum bundles are used to show the use of the fiber bundle mask. The two cingulum bundles are major neuronal white matter paths connecting the medial temporal lobe, thalamus and posterior cingulate. It has been hypothesized that episodic memory impairment in MCI most likely involves dysfunction of cingulum bundles. The GCC bundle is a large and strong white matter fiber bundle and is employed here to assess the performance of our approach in general cases. Among fiber bundles examined in this study, GCC has the most potential to be used as bio-markers to distinguish MCI patients from normal controls. For all of them, we measure regional micro structural white matter changes along the major fiber bundles in MCI patients compared with normal controls.

To illustrate the advantage that reconstructed fiber bundles can be used to approximate the volumetric white matter region efficiently, we also inspect the averaged FA and MD values of the entire 3D area. This entire volumetric white matter region may not be effectively revealed by VBM or ROI methods.

2.4.1 Subjects

The DIT data used in this study is provided by Dr. Stephen E. Rose at the University of Queensland, Australia [23]. In detail, seventeen healthy elderly adults (7F/10M, mean age 73.59 (SD 9.06), median Mini Mental State Examination score (MMSE) 28 (range $27-30$) and 17 MCI participants (7F/10M, mean age 73.58 (SD 8.96) years, median MMSE 26 (range $24-29$)) took part in the study. The local ethics committee approved the study and informed consent was obtained for each subject. In this study, participants were categorized on the combination of medical history, clinical and radiological examination and neuropsychological assessment by consensus meeting of a neurologist and 2 neuropsychologists. Participants were excluded from the study if there was evidence of prior head

trauma, a primary psychiatric diagnosis, infectious or endocrine cause of cognitive dysfunction, a Geriatric Depression Scale score of ¿ 16, alcohol consumption greater than 30 grams per day in men and 20 grams per day in women, or a history of drug habituation to drugs such as benzodiazepines or narcotics. Control and MCI participants were recruited from newspaper advertisements and were all community dwelling. All underwent neuropsychological testing using a battery of tests devised to detect cognitive impairment in older adults, including a 7 subtest short form of the WAIS-III [69, 70] the Logical Memory, Paired Associates and Face Recognition subtests of the WMS-III [71], Rey Auditory Verbal Learning Test [72], Boston Naming Test [73], letter and category verbal fluency [72], Trail Making Test forms A and B [74], the Number Location, Dot Counting and Cube Analysis subtests of the Visual Object and Space Perception Battery [75], and Stroop Neuropsychological Screening test [72].

Amnestic MCI diagnosis was determined according to the Mayo Clinic Alzheimers Disease Research Centre criteria [76, 77], and required the following (a) subjective memory impairment according to the patient and/or an informant, (b) objective memory impairment indicated by a delayed recall score on the WMS-III Logical Memory subtest and RAVLT of at least 1.5 standard deviations from age and education adjusted norms [76], (3) relatively normal performance on other tests measuring other cognitive domains, and (4) relatively normal activities of daily living. Participants were excluded if they satisfied a diagnosis for dementia as defined by either NINCDS-ADRDA criteria [78] and/or DSM-IV criteria [79]. Hachinski scores, in addition to Wahlund age related white matter changes (ARWMC) scores, were recorded for all participants [80]. Wahlund scores were obtained from high resolution T2-weighted FLAIR scans. The mean (standard deviation) duration between neuropsychological testing and DTI acquisition was $57(24)$ and $84(61)$ days for the MCI and control participants, respectively. MCI subjects were not administered any cognitive enhancing agents during the course of the study.

Examinations were implemented on the correlation of DTI with three tasks known to

be sensitive to MCI. They are the Rey Auditory Verval Learning Test (RAVLT) [72], the Boston Naming Test (BNT) [73], and a category fluency test [82].

2.4.2 Quantitative Analysis

A non-paired student t-test was employed to evaluate the group difference in MD and FA values between MCI participants and controls for the entire region along the computed white matter pathways. The integrity of these white matter fiber tracts was further evaluated by performing non-paired student t-tests on isonodes across subjects along the geodesic paths. p values ≤ 0.05 were considered as statistically significant in this study.

2.4.3 The Cingulum Bundles

For averaged FA and MD values of the entire volumetric region of the computed bilateral cingulum fiber bundles for the amnestic MCI and control subjects, we found no significant difference between the two groups. The only regional structural white matter alteration that we found is the significantly decreased FA value along the left cingulum.

Regional Structural White Matter Changes along Bilateral Cingula

Figure 2.3 and Figure 2.4 illustrate statistical analysis results of the FA value degradations along the left cingulum occurred at the location shown in yellow color. This degradation area is about $3.83mm$ long along the left cingulum bundle. The ROI size is $1.81 \times 0.9 \times 1.65mm^3$. Due to the small volumetric size of the degradation region, we show it in an uniform color instead of p value coded colors for clarity.

Effect of ROI Size

To assess the possible effect caused by the size of the seed region ROI in the reconstruction of the left cingulum bundle, we used two different size ROIs, one small ROI with dimension $1.81 \times 0.9 \times 1.65mm^3$ and one large ROI with dimension $5.4 \times 0.9 \times 4.13mm^3$. By comparison, we found that ROIs of different size generate similar but not identical results. The FA degradation area is about $3.83mm$ with the smaller ROI and $2.67mm$ long with the

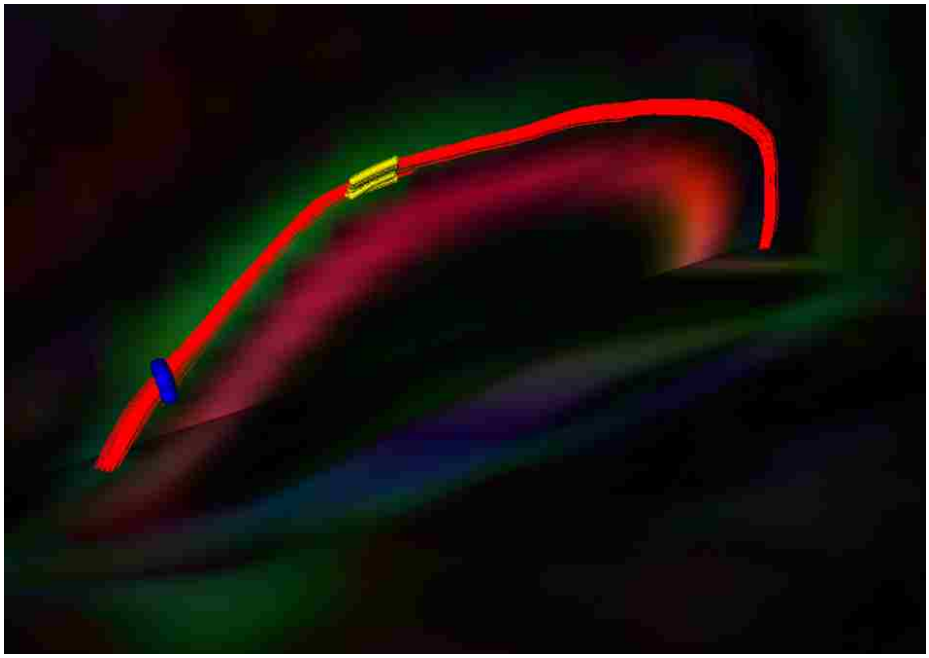

Figure 2.3: The left cingulum bundle mask overlapped on the FA value indexed color map. The ROI is in blue and is the starting point of the geodesic path mapping. The yellow color illustrates the region which shows significant FA value reduction in MCIs compared with the control subjects.

larger ROI in arc-length along the left cingulum fiber bundle. Significantly elevated MD region was not found with either the larger ROI or the smaller ROI.

For a better understanding on why the above two FA degradation areas are not identical in arc-length and their relations with the size of the ROIs, we investigated the voxels covered by the left cingulum bundle mask and compared their FA values based on the correspondence of global voxel indices in the two ROI cases. A group of 17 connected voxels were explored with significant differences in FA in both cases (shown in Figure 2.5). The two groups contained the same set of voxels. They were located in the same region where the aforementioned significant FA value reductions were found. Furthermore, since the smaller ROI generated a thinner fiber bundle than that generated by the larger ROI, fewer number of fiber covered voxels were averaged within each geodesic arc length in the smaller ROI than that in the larger ROI case. With the same number of voxels having significant FA value differences, the larger ROI, subsequently the thicker fiber bundle, would

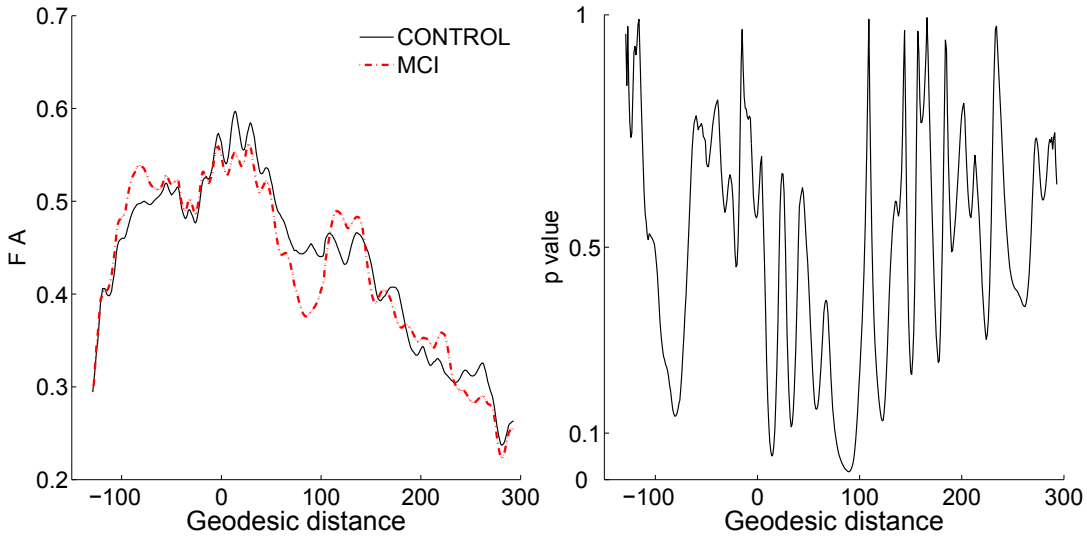

Figure 2.4: Regional FA distribution along the left cingulum bundle in MCIs. The left subfigure illustrates the regional FA value distributions of the control and MCI groups along the geodesic path. The right subfigure gives the p values of the student t-test along the geodesic path.

blur the averaged FA value reduction to some degree. This explains the observation that the smaller ROI demonstrates a relatively longer FA value degradation region along the left cingulum geodesic path than that of the larger ROI. Figure 2.6 illustrates the FA value degradation and the computed p values of these 17 voxels.

2.4.4 The GCC Bundle

Four control and two MCI subjects were removed from the experiment since their reconstructed GCC bundles were not long enough to reach the GCC forceps. Figure 2.7 shows the GCC fiber tracts based on a tensor averaged image from all subjects.

Averaged FA and MD Values of the Entire Volumetric GCC Bundle

Averaged FA and MD values for the entire volumetric GCC bundle between the MCI and control subject groups are listed in Table 2.1. It shows that the averaged FA is significantly reduced while the averaged MD value is significantly elevated in the MCI subjects.

The scatter plots in Figure 2.8 depict the distributions of the FA and MD values of the

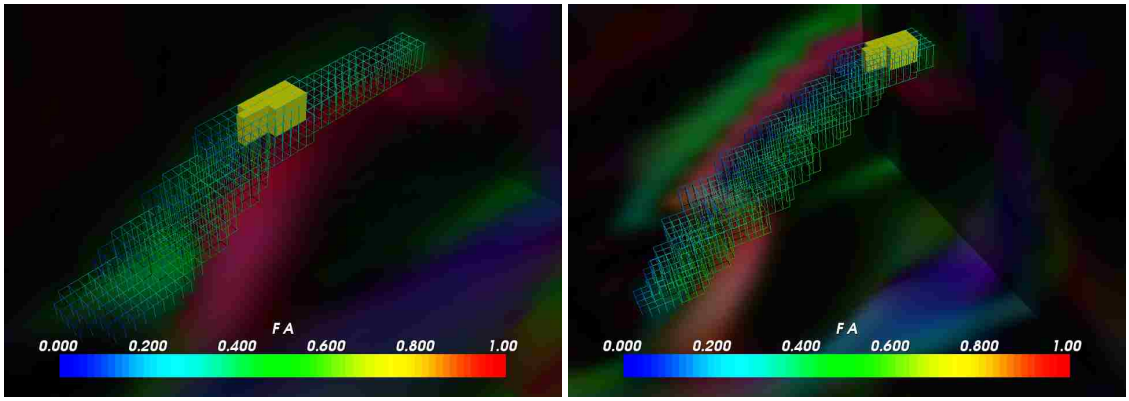

Figure 2.5: Left cingulum fiber bundle covered voxels overlapped on an FA indexed color map. Voxels are rendered in wireframe and their colors ranging from blue to red are in accordance with FA values from 0 to 1. Voxels with significant FA degradation are in yellow.

Table 2.1: Mean ($\pm SD$) values for the FA and MD measures for the entire volumetric GCC bundle for MCI and normal control groups. The unit of MD is ($10^{-6}mm^2/sec$).

GCC Bundle	Normal Control	MCI	p value	df
FA	0.56 ± 0.05	0.51 ± 0.05	0.005	26
MD	844 ± 62	921 ± 88	0.007	26

entire volumetric region of the GCC paths in normal control and amnestic MCI subjects separately.

Regional Structural White Matter Changes along GCC Bundle

Specific anatomical locations along the GCC bundle with significantly reduced FA and elevated MD measures were effectively discovered in MCI patients. The regional FA and MD value differences along the GCC tract bundle between the normal control and MCI groups are plotted in Figure 2.9 respectively. It shows that the most severe FA degradation and MD elevation in MCI subjects mainly happen within the area close to the mid-sagittal plane. The explored white matter alteration in this midregion is consistent with previous literature findings using the ROI approach [25]. Figure 2.10 visualizes the revealed local statistical features with isonodes color indexed by their p values overlapped on the reconstructed GCC bundle.

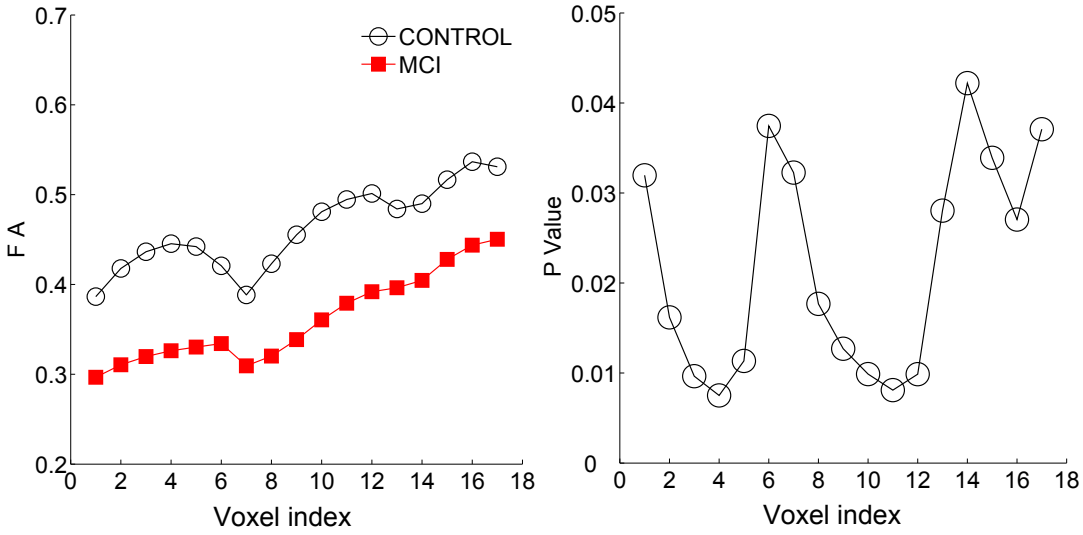

Figure 2.6: The left subfigure shows the FA value distribution of the 17 connected voxels for both the control and MCI groups. The right subfigure depicts the p values after the student t-test along the geodesic path.

2.5 Discussion and Conclusion

We have presented a novel framework to measure white matter alterations along fiber tract bundles. Strategies have been developed for thin and large white matter fiber tract bundles separately. We represented the curved cingulum bundles using a DTI tractography produced fiber bundle mask. This method can also be applied to other thin fiber bundles which are hard to reconstruct their full paths for all subjects in group analysis. Our method makes it possible to examine the micro structural changes along the left and right cingula for all subjects in the comparison. We also illustrated the advantage of our approach to measure large and strong fiber bundles by performing fiber tracking in each subject's individual space. The use of the isonode visualization scheme to help us understand any white matter alterations along fiber bundles is illustrated as well. Experimental results of this study are in agreement with previous amnestic MCI findings [23, 25]. This shows that this analysis method is promising and may provide a sensitive approach to determining the integrity of neuronal pathways in human brain.

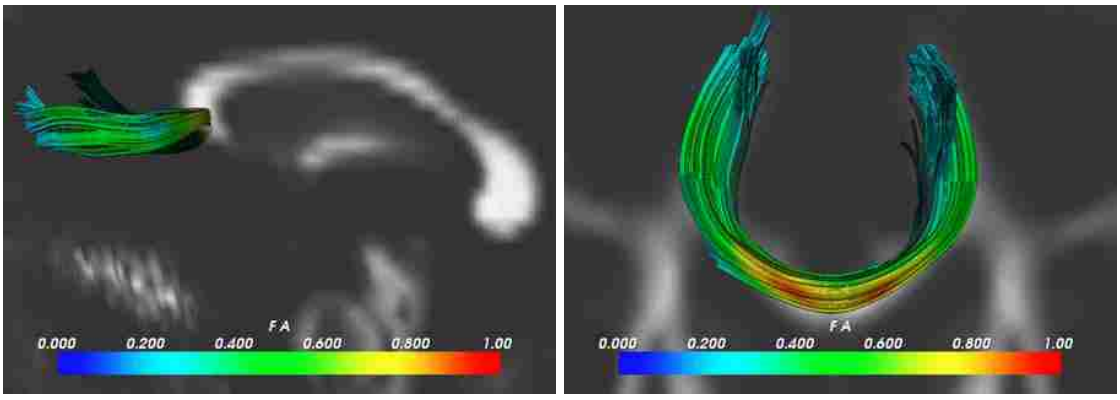

(a) GCC bundle in sagittal view (b) GCC bundle in coronal view

Figure 2.7: The reconstructed GCC fiber tracts overlapped on a tensor averaged FA map of all subjects. Subfigures (a) and (b) show the GCC bundle in sagittal and axial views respectively.

Previous DTI studies in amnestic MCI have found significantly reduced measures of FA value within posterior dorsal regions of the left cingulum bundles [23, 24, 64]. These studies employed either ROI or automated VBM analysis method. Although ROI approach is robust in large white matter tracts, with thin white matter pathways it may be less reliable due to confounding partial volume effects, exacerbating the difficulty associated with the accurate and consistent placement of ROIs within target tracts across all subjects [65]. The VBM analysis method reduces this problem, although issues concerning image registration, segmentation and the choice of smoothing kernels prior to statistical analysis of grouped data are still to be resolved [65]. The presence of unrelated fibers may also result in the contamination of targeted fiber pathways using this approach. In contrast, DTI tractography enables robust generation of fiber trajectories across subject groups with less off-target fiber contamination. In addition, the integrity of the computed tracts can be analyzed by evaluating diffusivity indices either averaged for the entire tract or along the length of the white matter pathway in a spatially continuous fashion.

Non-invasive neuroimaging techniques, which can investigate the integrity of the cingulum fasciculi, are extremely important in understanding the progression of some brain diseases such as Alzheimer's disease (AD). There is converging agreement based upon

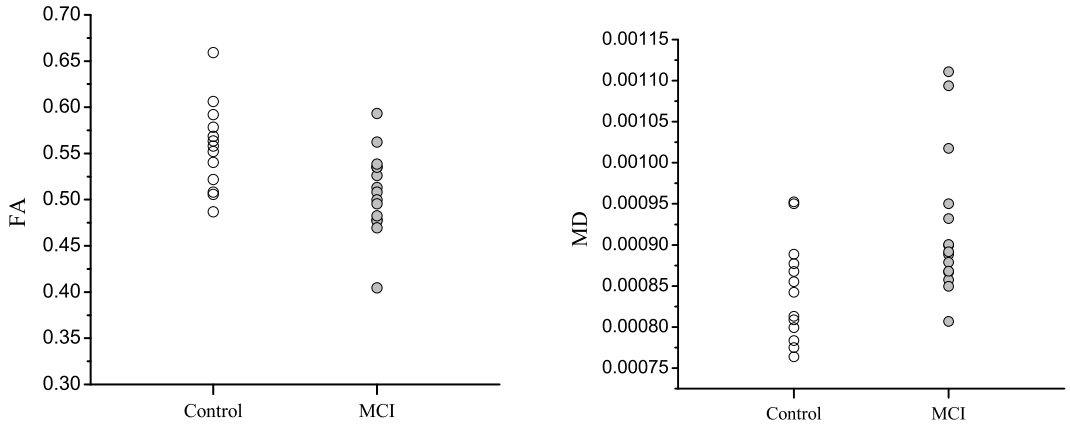

Figure 2.8: Scatter plots of the averaged FA (left) and MD (right) values of the entire volumetric region of GCC bundle in normal control and amnestic MCI subjects. The unit of MD is (mm^2/sec).

structural and metabolic studies of the importance of the involvement of the posterior cingulate gyrus in AD [23, 24, 64, 66]. It is important to study the link between white matter pathways of the cingulate gyrus and the cholinergic system [67]. With the proposed technique, the entire curvilinear left and right cingulum regions can be defined and evaluated. The findings of this study reaffirm the importance of being able to spatially define a complex 3D region of interest in DTI tractography and to study the diffusion measures along the length of the white matter pathways.

There are a number of limitations with this study. Due to the signal-to-noise limitations at the resolution of our DTI data, even with the use of an optimized DTI acquisition scheme, we could not robustly compute white matter trajectories for the more ventral pathway of the cingulum bundles. Analysis of geodesic paths of the white matter tracts that project from the hippocampus to the posterior cingulate gyrus would be extremely useful and provides a challenge for high field (>3T) DTI studies in AD. Although DTI-based tractography method is automated, tractography algorithms normally rely on the manual placement of ROI to compute target white matter trajectories. In this study, we carefully placed the ROI within the cingulum with the help of an FA indexed color map. Alternative methods of

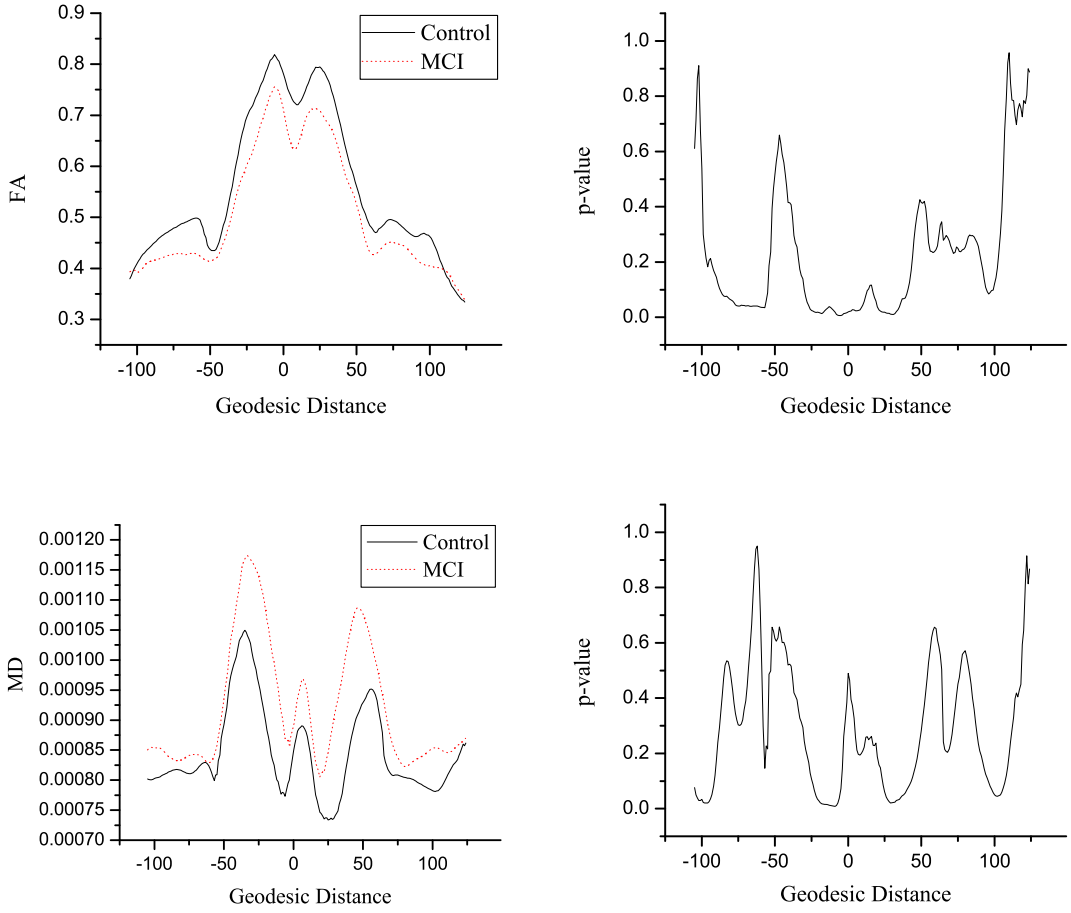

Figure 2.9: Statistical analysis of regional micro structural FA and MD alterations along the GCC paths. Negative and positive geodesic indices are in accordance with the left and right parts of the starting point plane (indexed by 0) in Figure 2.2's right-hand side subfigure. The geodesic distance unit is $0.5mm$. The unit of MD is mm^2/sec.

analyzing diffusivity measures along target white matter trajectories that do not require accurate within subject registration would be of considerable benefit [68]. Inclusion of a reference AD subject group would have been of interest to explore the full potential of this new fiber tract analysis technique.

Significant reduction in the FA value within specific anatomical regions was only detected by evaluating diffusivity measures mapped as geodesic paths. Our analysis technique is able to pinpoint the exact fiber locations with altered diffusion properties and may provide a more sensitive technique for determining the integrity of white matter tracts in the

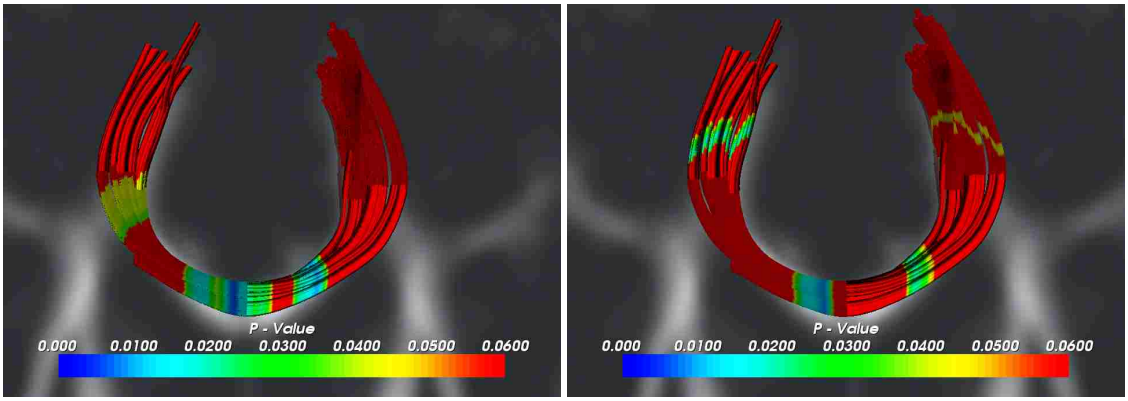

Figure 2.10: Visualizations of regional micro structural FA (left) and MD (right) alterations along the GCC bundle. Revealed regions with significant FA degradation and MD elevation in MCI subjects are rendered in their according p value indexed colors. p values greater than 0.06 were rendered as 0.06 for simplicity.

brain.

3 A Unified Framework for Modeling and Clustering a Small Number of White Matter Tracts

3.1 Outline

In this chapter, recent developments in white matter tract clustering techniques are first surveyed at the beginning. We then present in detail the proposed framework which aims to classify a small number of reconstructed white matter fiber tracts which may not have common starting region and/or equal length. Experimental results with real DTI data are used to demonstrate the performance of the method. A discussion about the advantage and limitations of the presented technique is included at the end.

3.2 Introduction

DTI based tractography enables selective reconstruction of specific neural pathways [27, 35, 37] and has been used to visualize brain white matter fiber tracts to facilitate our understanding of brain structural connections in clinical applications such as neurosurgery planning. In recent years, developing analysis methods for extracting quantitative information from DTI and classifying white matter fiber bundles has received extensive attentions. Such information is helpful in understanding human brain connectivity and in tackling a variety of brain diseases and disorders, such as Alzheimer's disease, multiple sclerosis, and schizophrenia.

To achieve meaningful and reproducible results for techniques based on quantitative analysis of reconstructed white matter tracts, accurate and efficient tools are necessary to group the trajectories into anatomically meaningful clusters or bundles. A variety of white matter tract segmentation schemes have been proposed in recent years. Most of these techniques set unlabeled tracts (or streamlines) extracted from DTI tractography as input. Methods able to remove outliers will output part of the labeled inputs.

Based on their fundamental mechanisms, these methods can be divided into three categories, i.e., visual dissection, automatic clustering, and atlas based segmentation. Conturo

et al. [52] and Mori et al. [93] proposed a visual dissection method by manually selecting tracts passing through one or more user defined ROIs in the process of DTI tractography. This approach can be used to remove anatomically plausible tracts and is commonly used in practice. One limitation of this method is that it is time consuming to segment a large amount of spatially closed fibers which demonstrate complex structures in general. Good knowledge of brain white matter anatomy is necessary for this method to work well. Most published literatures on white matter tract segmentation so far fall into the second category, i.e., the automatic clustering. In this class of methods, a set of features of a fiber tract and a pairwise similarity (or affinity) measure are mathematically defined in advance. A number of supervised or unsupervised clustering algorithms in this category have been published. Ding et al. [94] bundled reconstructed white matter tracts by finding the corresponding portion of two tracts that have point-wise correspondence between them. The similarity between two tracts was formed by calculating the point-wise Euclidean distance. For doing so, these two compared tracts need to have the same starting region. This restriction may limit the application of this method. Burn et al. [95] described a tract representation which is a 9-dimensional feature vector representing the mean and the lower triangular part of the covariance matrix of step points on a tract. A Gaussian kernel of Euclidean distance between two feature vectors was employed as the similarity measure. The clustering algorithm used is called normalized cuts which first appeared in the computer vision community. Gerig et al. [97] and Corouge et al. [96] introduced Hausdorff and similar distance metrics when compare a pair of tracts point-wisely and kept individual local shape characterization of each tract within the associated bundle. Equal tract length was assumed following the assumption that tracts under consideration were from a common starting area which is not the general case. Xia et al. [98] reported a similar method with the extension that the spatial organization of gray matter was employed as a reference for identifying white matter tracts. With this strategy, two tracts do not have to have a common starting region. The trade-off is that some gray matter areas have to be precisely located in advance

of the tract segmentation. Jonasson et al. [99] employed the spectral clustering technique to segment white matter tracts reconstructed from high angular resolution DTI data. The classification is performed by counting the number of shared voxels as the affinity metric between a pair of tracts. In the work of El Kouby et al. [100], the clustering is not performed directly on the fascicles but on a number of ROIs by splitting the Talairach grid into small cubes. These cubic ROIs need to be transformed back to the individual subject space. Batchelor et al. [101] compared several quantitative metrics including link and the Euclidean distance of Fourier descriptors to study the relative spatial configurations of trajectory pairs and indicated that these measures could be used in classifying and clustering the reconstructed white matter tracts. They made the assumption that the point-wise correspondence between a pair of tracts could be established by the selection of a seed point and regular re-parameterizations. O'Donnell et al. [102, 103] proposed a framework to label new coming fiber bundles based on an atlas which is built in advance. In the intra subject clustering process to construct the atlas, a symmetric affinity matrix needs to be maintained and handled to compute eigenvalues and eigenvectors for the tract spectral embedding. This matrix may be very large if a huge set of white matter tracts are reconstructed by applying some common tractography techniques such as the backward streamline tractography algorithm introduced by Mori and van Zijl [39] in the case of whole brain tractography. Klein et al. [104] described a multiple eigenvector fiber tract clustering method by using singular value decomposition (SVD) to factorize the similarity matrix to determine the possible number of clusters. They reduced the computational complexity from $O(n^2)$, which is a typical cost of spectral clustering, to $O(n)$. This is achieved by assuming that a single cell does not contain more than a fixed number of tracts in the average situation. This method could be very sensitive to the noise which is inherent to the DTI data. And it is still an open issue if the proposed approach is practical for estimating the number of clusters . Maddah et al. [105] introduced a atlas-based framework for white matter tract clustering and quantitative analysis. They employed the expectation-maximization (EM) algorithm to partition

the trajectories into the context of a Gamma mixture statistical model of distances. This approach needs the *a priori* knowledge of each target fiber bundle. The anatomical atlas is obtained by user-drawn curves or manually selected trajectories. Features used in the clustering are mutual features which are extracted by calculating distances between corresponding step points along two tracts. One of the two tracts may be a user-drawn reference curve. This method is helpful for clustering a large amount of white matter tracts.

These existing methods have their advantages and disadvantages as discussed above. There is no universal measure to assess which clustering algorithm and parameter settings give the best results. Moberts et al. [106] evaluated some clustering methods and compared them with a manual classification. They found that the use of hierarchical clustering with a single-link and a tract similarity measure based on the mean distance between tracts gave the best results. In general, performances of existing tract clustering algorithms is very dependent on how well they tackle the random configuration of tracts, e.g., unequal tract length and different starting regions. Challenges in the development of clustering techniques with consistent performance include (1) objective representations of reconstructed white matter tracts, (2) quantitative affinity measurements with enough differentiation capability, (3) matching correspondences to calculate similarity metrics between two random tracts, and (4) a robust clustering algorithm.

In this work, we propose a novel framework to address these challenges. Particularly, the objective representation is achieved by incorporating the information of diffusion orientation, tract length and geometric center into the mathematical model. The quantitative measurements are implemented by calculating the pairwise affinity score which is sensitive to tract shape, location, and length. A matching method is developed to establish piece-wise correspondences between two randomly located tracts. The clustering algorithm we employ is the well known K-mean algorithm. Experiments with real DTI data are conducted to assess the performance of our approach.

For the sake of simplicity, we refer to reconstructed white matter tracts as streamlines

in the following discussion.

3.3 Theory

3.3.1 Streamline Representation

To take the advantage of the diffusion orientation information carried in DTI and incorporate this information into the streamline representation, we introduce the substreamline and linear segment concepts by a review of the tract reconstruction procedure. Since different tractography algorithms produce different forms of output, we take as the example streamlines being reconstructed from the popular streamline based DTI tractography algorithm [5, 38] to demonstrate our streamline representation.

The streamline based tractography algorithm takes as input a set of seed points and produces numbers of voxelized outputs, the fiber tract streamlines. The process to generate streamlines is typically to choose a local diffusion orientation in a specific voxel starting at a seed point, moves a small distance in one of the two directions parallel to the local voxel's diffusion orientation (i.e., the principal/primary eigenvector derived from diffusion tensor calculation), and repeats until some termination criteria are met. The moving distance at each step may or may not be equal. This process has to be performed for the second time to reconstruct a complete streamline by reversing the moving directions (the principal eigenvectors). This is because water diffusion is directionally nonspecific or bidirectionally symmetric and in turn the same for the diffusion orientation in DTI data. A streamline is saved as a sequence of step points. Each step point is associated with a primary eigenvector indicating the local diffusion orientation of a specific voxel it lies in. A pair of adjacent step points and their in-between connection, the two directionally symmetric major eigenvectors, define a linear segment of a streamline. As a result, a streamline s is sets of connected straight line segments with equal or unequal length. A single linear segment is parallel to the local diffusion orientation in a particular voxel. We will refer this voxelized parallelism feature to be a streamline's "local diffusion orientation". And a streamline's length L is

defined as the number of segments it has.

This local diffusion orientation is inferred from the local primary eigenvector and its reversed direction. A principal eigenvector indicates one of the two directions referenced by a diffusion orientation. The second direction can be easily obtained by reversing a principal eigenvector. In the following, we represent local diffusion orientations by principal eigenvectors and use the two terms interchangeably for convenience. But we should note that they are not equivalent.

As a result of the above two step reconstruction strategy, a streamline can thus be conceptually split into two substreamlines at its seed point, indicating what we will refer to as the "forward" and "backward" substreamlines in this study. Subsequently, a streamline's length equals to the summation of its two substreamline's length, i.e. $L = L_f + L_b$. L_f and L_b are lengths of the forward and backward substreamline respectively. It is worth mentioning that the terms forward and backward we used here have no strict significance. They are for convenience only. Figure 3.1 graphically depicts the rationale we describe in this paragraph. Arrows in the forward substreamline in subfigure 3.1(a) represent the primary eigenvector directions in the first reconstruction step. The backward substreamline is reconstructed in the second step. Arrows in the backward substreamline thus reflects the reversed major eigenvectors. Subfigure 3.1(b) shows an implementation example.

The local orientation feature gives us only the shape information of a streamline. In order to distinguish a streamline from others as distinct as possible, we still need more features. Natural choices would be its global measures such as its geometric center and the global diffusion orientation which we will describe. The geometric center of a streamline indicates its mean spatial position and can be used to assess the global geometric relationship between two streamlines. But multiple streamlines may share one common geometric center. For instance, different half arc partitions of a circle have their geometric center overlapped though they do occupy different spatial positions. To differentiate this type distinct curves, we associate a streamline's geometric center with a direction feature, the global

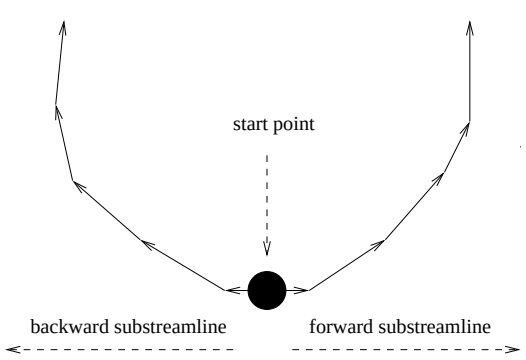

(a) Two step reconstruction of a complete streamline and its two subparts

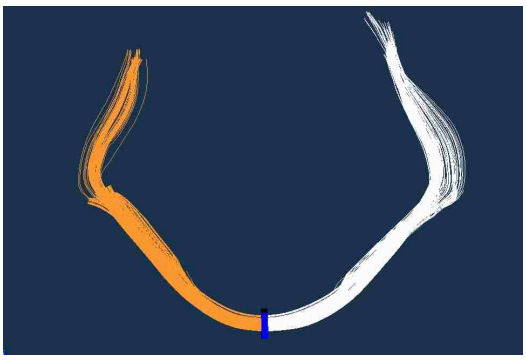

(b) Implementation of the two step reconstruction method

Figure 3.1: Graphical illustrations of the two step reconstruction scheme resulted in forward and backward subpartitions. Arrows in in the two substreamlines in (a) represent local primary eigenvectors in the two reconstruction steps respectively. The backward substreamline is reconstructed by reversing all principal eigenvectors. In (b), the starting points to reconstruct the tract bundle are in blue. The two fiber bundles in distinct colors represent the forward and backward substreamlines respectively.

diffusion orientation. A streamline's global diffusion orientation is the accumulation of its all local diffusion orientations, the simple summation of all voxel's principal eigenvectors along this streamline. It is parallel to the virtual straight line directly connecting a streamline's two end points. It is also bidirectionally symmetric, the same as the local diffusion orientation. It gives us the directional knowledge about the connectivity between the two end points of a streamline. With the help of this new feature, we are now able to distinguish streamlines of equal length and same geometric center such as the aforementioned different half arc parts of a circle. This is demonstrated in Figure 3.2, which shows two curves, s_1 and s_2, sharing one common geometric center.

It should be noticed that this global diffusion orientation concept does not make sense if a streamline's two end points are overlapped (e.g., a closed curve), such as a circle. It is of no help if two streamlines share both of their two end points and geometric centers. Fortunately, such situations are rarely encountered in streamlines reconstructed from most existing DTI tractography algorithms.

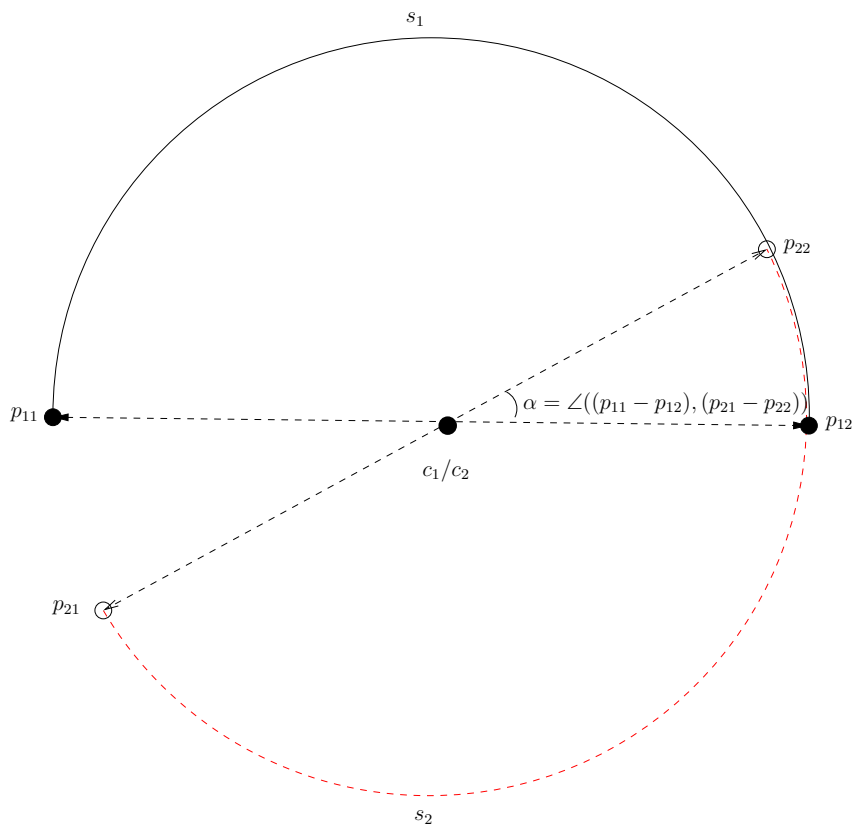

Figure 3.2: Illustration of the global diffusion orientation used to distinguish two curves sharing a common geometric center. The black solid and red dotted curves, s_1 and s_2, share a common geometric center c_1 or c_2. The two black dotted lines represent the two global diffusion orientations of s_1 and s_2 respectively. s_1 and s_2 can be identified with the help of their global diffusion orientations if $\alpha \neq 0$.

Hence, we can model a streamline s as

$$s = \{e,\ c,\ v\}, \tag{3.1}$$

where $e = \{e_1, e_2, ..., e_L\}$ is sets of local diffusion orientations of a streamline. L is the streamline length, i.e., the number of linear segments. c is the geometric center. And v is the global diffusion orientation and is formulated as

$$v = \sum_{i=1}^{L} e_i. \tag{3.2}$$

Two streamlines, s_1 and s_2, their geometric centers, local and global diffusion orientations are illustrated in Figure 3.3. Arrows of straight line segments in Figure 3.3 demonstrate one of the two local possible diffusion directions. Reversed arrows are another sets of

local diffusion directions. Two geometric centers, c_1 and c_2, are marked as solid circles. β_i is the angle between the i-th corresponding segment pair of two matched streamlines. α is the angle between the two global diffusion orientations. Each streamline's global diffusion orientation is parallel to the straight line directly connecting its two end points. The length of both s_1 and s_2 are 4 (4 straight line segments) in this example. We use principal eigenvectors along a streamline to represent local diffusion orientations, i.e., $\beta_i = \angle(e_{1_i}, e_{2_i})$ and

$$\alpha = \angle(v_1, v_2) = \angle(\sum_{i=1}^{L} e_{1_i}, \sum_{i=1}^{L} e_{2_i}), \tag{3.3}$$

where L equals 4 in this instance.

3.3.2 Streamline Similarity Metrics

The reason that we employ in clustering is that two streamlines should be in the same cluster when they (1) connect the same two anatomical regions; (2) have similar shape; and (3) are separated by a short distance. The first characteristic requires that they have comparable length in addition that the two virtual lines directly connecting their respective end points be parallel and spatially close. Similar shape means that most corresponding straight line segments of the two streamlines should be as parallel as possible. The last property is related to the distance between the two geometric centers. These goals can be achieved by using the appropriately formed affinity measures based on the previously defined streamline model.

In our implementation, we consider that two streamlines belong to one cluster if they satisfy four criteria: (1) comparable length, i.e., the number of segments $L_1 \approx L_2$; (2) short geometric center distance d_c; (3) close to 1 the absolute cosine value of their global diffusion orientations $|\cos\alpha|$; (4) close to 1 the cosine value $\cos\beta_i$ for most corresponding local diffusion orientation pairs. We here use the accumulated cosine value $\sum_{i=1}^{n}\cos\beta_i$ of all segments to assess the fourth criterion. This is much like a voting scheme for curve

matching in the field of computer vision [86]. Each pair of segments vote to the final score with a weight equal to their cosine value and in turn their shape similarity. Highly matched streamlines will receive votes of large (close to 1) weight. The cosine value is given by the normalized inner product of two vectors

$$\frac{e_1^T \cdot e_2}{\|e_1\|\|e_2\|}. \tag{3.4}$$

To compute the local shape similarity, we first define the relative length difference, δ, between a pair of streamlines as

$$\delta = \|\frac{L_1 - L_2}{n}\|, \tag{3.5}$$

where L_1 and L_2 are lengths of the two streamlines respectively and $n = \min(L_1, L_2)$. δ has the value zero if $L_1 = L_2$, and unity if either L_1 or L_2 is zero. A longer streamline pair has a smaller δ value than that of a shorter streamline pair with a fixed absolute length difference. The length difference between a very long and a fairly short streamline is magnified by this definition.

Gaussian kernel is employed to assess the relative length difference. The local similarity score between two streamlines under the current principal eigenvector setting, S_{l_1}, is formed by the summation of segment cosine values together with the length factor.

$$S_{l_1} = \frac{1}{n}\sum_{i=1}^{n} \cos\beta_i \exp\left(-\frac{\delta}{2\sigma^2}\right). \tag{3.6}$$

This means that the cosine value computation depends on the length of the shorter one of the two streamlines. Since the current principal eigenvectors are in one of the two diffusion directions, we then reverse all primary eigenvectors of any one of the two streamlines and repeat the calculation in Equation 3.6 to obtain S_{l_2}. S_{l_1} and S_{l_2} both have values in the interval of $[-1,\ 1]$. The first component of pairwise overall similarity score (PWOSS), the local similarity measure, is finally established as

$$S_l = \max\left(S_{l_1}, S_{l_2}\right). \tag{3.7}$$

The values of S_l range from -1 to 1.

A natural question arises here is that why we do not calculate the absolute value of $\cos\beta_i$, instead, we compute S_{l_1} and S_{l_2}, the signed cosine values separately. The reason is that the signed cosine values of all corresponding segments between a streamline pair can give their relative global as well as local shape information without additional computational cost. On the other hand, the absolute cosine values carry only their relative local shape information. This property is especially useful when we compare two spatially close streamlines belonging to two fiber bundles. It is also computationally efficient in removing outliers within a tract cluster. Figure 3.4 illustrates the advantage of the signed cosine value over the absolute cosine value. In Figure 3.4, there are three streamlines, s_1, s_2 and s_3, each has a length of 7. The segment signed cosine values $\cos(e_7, e_{7'}) = 1$, $\cos(e_7, e_{7''}) = -1$ and $\cos(e_{7'}, e_{7''}) = -1$. While $\cos(e_1, e_{1'}) = 1$, $\cos(e_1, e_{1''}) = 1$ and $\cos(e_{1'}, e_{1''}) = 1$. These signed values reveal useful information that the end partitions of s_1 and s_3, s_2 and s_3 terminate in two opposite directions while they start in the same direction. On the other hand, s_1 and s_2 end in the same direction. The same conclusion can also be drawn with all reversed principal eigenvectors. By contrast, the absolute cosine value carries no such information.

The second constituent of PWOSS, the global affinity metric, is given by

$$S_g = |\cos\alpha| \exp\left(-\frac{d_c}{2\sigma^2}\right), \tag{3.8}$$

where $d_c = \|c_1 - c_2\|$ is the Euclidean distance between the two geometric centers. $\cos\alpha$ represents the cosine value of two global diffusion orientations. S_g thus quantifies both global geometry and global shape relationships between a pair of streamlines. Its value lies in the interval of $[0,\ 1]$. S_g equals zero when global diffusion orientations of two streamlines are perpendicular to each other. It is unity if the two global orientations are parallel as well as the two geometric centers are overlapped.

Using our developed global and local affinity measures, we here combine them together

to form the PWOSS between two streamlines as

$$S(s_1, s_2) = \omega S_l + (1 - \omega) S_g, \tag{3.9}$$

where ω is the weight of the local affinity scores and takes values from 0 to 1. It can be simply set to 0.5 in most cases. The bounds of the PWOSS are -1 and 1. A higher value of PWOSS indicates a stronger match, and a lower value reflects a weaker match. The PWOSS value equals one if and only if a streamline is matched with itself.

Figure 3.5 shows examples of different spatial organizations of streamline pairs and their corresponding similarity scores. The subfigures depict how the similarity measures depend on different relationships between a pair of streamlines. Streamlines are drawn in continuous, smooth curves instead of a sequence of linear segments for simplicity. They demonstrate how the two components of the PWOSS value are scored under different scenarios. In subfigure 3.5(a), the pair of streamlines have equal length and are parallel to each other. As a result, they get a full score in S_l. $S_g < 1$ since the two geometric center are not identical. They are likely to be identified as being in one cluster if their geometric centers are close enough. Two streamlines in subfigure 3.5(b) share both a common geometric center and global diffusion orientation. Subsequently their $S_g = 1$. Here $S_l < 1$ since they have unequal length. This pair of streamlines may be classified into one bundle if their relative length difference is small. Subfigure 3.5(c) shows the general relationship between two random streamlines.

3.4 Methods

3.4.1 Streamline Parameter Fitting

The backward streamline based DTI tractography technique proposed by Mori and van Zijl [39] is employed in this analysis to generate input streamlines for tract partition purpose. The tractography output is a set of streamlines with unequal separation distances between successive step points. To obtain comparable length unit among tracts for clustering, all streamlines are first fitted using a fixed geodesic arc length. After this parameter

fitting, all streamlines have the same length unit. This makes it possible to evaluate the length difference between two streamlines. But it should be noticed that each segment of a streamline may no longer be strictly parallel to the voxel's diffusion orientation it falls in. Another situation may arise is that a single linear segment lies in two or more voxels. In this scenario, we take the summation of the related multiple diffusion orientations as a segment's local orientation. To reduce these side effects we employ an arc length which is shorter than the voxel size in the fitting process.

3.4.2 Matching Starting Point Correspondence

To compare two arbitrary located streamlines, we need first to determine the matching starting points to begin our affinity calculation. There are mainly two scenarios depending on the spatial organization of tracts under consideration. The first is that a streamline pair share a common ROI which is usually a cutting plane perpendicular to both of them. This ROI can be a seed point region in tractography or a manually placed reference plane afterwards. One obvious example is the corpus callosum tracts for which the mid-sagittal plane is usually set as their common ROI. In this situation, all streamlines can be matched by starting from this ROI and moving towards along certain directions.

The second case occurs when tracts share no such common ROI. One example is shown in Figure 3.6. It is also difficult to manually place a common ROI, a cutting plane, perpendicular to all of them. This is more general than the first case especially when we isolate tracts stemmed from the whole brain tracing. To find matching starting points for a pair of streamlines in this situation is challenging. Our solution is to find the two closest step points such that each of them is located on a distinct streamline and their in-between distance is the minimum among all point-to-point distances between the two streamlines. Each of the two closest points is set as the matching starting point of the streamline to which it belongs.

The pair of the closest points (p_1, p_2) can be computed as

$$(p_1, p_2) = \arg \min_{p_{1_i} \in s_1, p_{2_j} \in s_2} \|p_{1_i} - p_{2_j}\|, \tag{3.10}$$

where p_{1_i} is any step point on the streamline s_1, p_{2_i} is any step point on the streamline s_2, $\|p_{1_i} - p_{2_j}\|$ is the Euclidean norm, $i \in [1, L_1 + 1]$, $j \in [1, L_2 + 1]$. L_1 and L_2 are the lengths of s_1 and s_2 respectively. This is a variation of the Hausdorff distance measure.

Note that it is possible to obtain multiple closest point pairs. In this case, any pair can be chosen without apparent difference in the clustering results. Another issue needs to be addressed is that a streamline's starting point depends on other streamlines with which it is matched. In general, it may have several matching starting points when compared with different streamlines.

With the common ROI or matching starting points outlined in above two cases, we can continue to conceptually treat a streamline s as two subpartitions, forward and backward substreamlines s_f and s_b. The splitting point of a streamline here is its matching starting point instead of the seed point in tractography. And this splitting point may vary when this streamline is compared with others.

3.4.3 Segment Correspondences and Bilateral Matching

As above described, the local similarity score S_l is calculated segment-wisely. Since a streamline is split into forward and backward partitions, with the matching starting points determined, we still need to find the correct moving directions, i.e. the substreamline correspondences to obtain segment-to-segment correspondences to compute S_l between two streamlines. Similarly, the substreamline correspondences are easily achieved for tracts sharing a common ROI. However, for tracts sharing no such common ROI it is not obvious.

There are two possible such correspondences between two streamlines s_1 and s_2 sharing no common ROI. They are either $(s_{1f} \leftrightarrow s_{2f},\ s_{1b} \leftrightarrow s_{2b})$ or $(s_{1f} \leftrightarrow s_{2b},\ s_{1b} \leftrightarrow s_{2f})$. $(s_{1f} \leftrightarrow s_{2f})$ here means the forward substreamline of s_1, s_{1f}, is corresponding to the forward section of s_2, s_{2f}. Each configuration generates different segment-to-segment correspondences. As a result, different local affinity measures, S_l, may be obtained.

We solve this directional uncertainty by inspecting the four end point distances between

a pair of streamlines. The underline rationale is that the pair of substreamlines from two distinct streamlines are in accordance with each other if their end points are close. Let $(p_{11},\ p_{12})$ and $(p_{21},\ p_{22})$ be the two end points of the streamlines s_1 and s_2 respectively. p_{10} and p_{20} are the starting points of s_1 and s_2. p_{11} and p_{12} are the end points of s_{1f} and s_{1b} respectively. Similarly, p_{21} and p_{22} are the end points for s_{2f} and s_{2b}. Assume $d_{11} = \|p_{11} - p_{21}\|$, $d_{12} = \|p_{11} - p_{22}\|$, $d_{21} = \|p_{12} - p_{21}\|$ and $d_{22} = \|p_{12} - p_{22}\|$ as depicted in Figure 3.7. The procedure to determine the substreamline correspondence can be described as

1. Calculate d_{11}, d_{12}, d_{21} and d_{22}.

2. If $d_{11} \leq d_{12}$ and $d_{22} \leq d_{21}$, the substreamline correspondence is $(s_{1f} \leftrightarrow s_{2f},\ s_{1b} \leftrightarrow s_{2b})$ and vise-versa. This means each of the two ends of a streamline s_1 are close to a different end point of another streamline s_2 as illustrated in subfigure 3.7(a).

3. If $d_{11} \leq d_{12}$ and $d_{22} > d_{21}$, compare the two shorter distances d_{11} and d_{21}. If $d_{11} \leq d_{21}$, the substreamline correspondence is $(s_{1f} \leftrightarrow s_{2f},\ s_{1b} \leftrightarrow s_{2b})$. Else if $d_{11} > d_{21}$, the substreamline correspondence is $(s_{1f} \leftrightarrow s_{2b},\ s_{1b} \leftrightarrow s_{2f})$. It is similar when $d_{11} > d_{12}$ and $d_{22} > d_{21}$. This case indicates that both of the two end points of a streamline s_1 are close to a common end point of another streamline s_2. This scenario is demonstrated in subfigure 3.7(b).

Once the substreamline correspondence is fixed, to figure out the segment-to-segment correspondences becomes trivial.

Figure 3.7 graphically illustrates the determination of substreamline correspondences under two possible scenarios. In subfigure 3.7(a), the two end points of streamline s_1, are close to two different end points of streamline s_2. In detail, p_{11} is close to p_{21} and p_{12} is close to p_{22}. The substreamline correspondence is established by the above procedure 2. In subfigure 3.7(b), both of the two end points of s_1 are close to a common end point

of s_2, i.e., p_{21}. This configuration falls in the category described in procedure 3 above. $(s_{1f} \leftrightarrow s_{2f},\ s_{1b} \leftrightarrow s_{2b})$ is the resulting substreamline correspondence for both cases.

After the segment-to-segment correspondences are formed, the calculation of local shape affinity measure S_l is performed bidirectionally, once in a direction. It begins at the starting points or a common ROI and moves towards the two end points of one pair of corresponding substreamlines, e.g., s_{1f} and s_{2f}, simultaneously, segment by segment. Then the calculation is repeated for another pair of corresponding substreamlines, e.g., s_{1b} and s_{2b}, in a similar manner. S_l is thus composed of two components to which we will refer as S_{lf} and S_{lb}. S_{lf} and S_{lb} are local affinity measures for the two pairs of corresponding substreamlines respectively. In general, $S_l = S_{lf} + S_{lb}$. However, in cases of the bilaterally symmetric tracts, such as the corpus callosum, S_l can be formed differently as $S_l = \max\{S_{lf}, S_{lb}\}$ or $S_l = \min\{S_{lf}, S_{lb}\}$ to emphasize more on the bilateral symmetry feature of fibers dependent on different applications.

3.5 Experimental Results

Two tract sets, the CST-MCP and CST-CPT-PTR (the posterior thalamic radiations) collective trajectories, were employed to assess our proposed approach in this study. Neither tract collection has a common ROI. And their length is unequal.

3.5.1 DTI Data

The DTI data used in this study are from health controls which are described in sections 1.3.2 and 2.4.1.

3.5.2 CST-MCP Tracts

The first tract collection is the CST-MCP data set as shown in subfigure 6.1(a). Its calculated PWOSS histogram is shown in subfigure 3.9(a). This PWOSS histogram reveals that the proposed similarity metrics characterize streamlines successfully with the fact that the number of peaks in the histogram suggests the number of possible subclusters. Further-

more, the height of a peak reflects the number of streamlines in one subbundle (subcluster size). For example, there are three relatively high peaks in subfigure 3.9(a). One is widely separated from the other two which are close to each other. As a result, the CST-MCP bundle may be partitioned into two subclusters with large intra cluster similarities. It may also be differentiated into three subbundles and two of the three subclusters are expected to have relatively large inter cluster similarities. However, this may cause some clustering errors since the height of the midpoint between the two right adjacent high peaks is not close to zero. We thus prefer to first classify this CST-MCP tract set into two subclusters. Another merit of this type of histogram is that it can be used to probe the PWOSS threshold to obtain the desired number of subbundles in advance of the clustering. The PWOSS threshold can be any similarity value in the interval between the two adjacent peaks. The wide interval between the left two peaks in subfigure 3.9(a) means a wide selection range of the PWOSS threshold and subsequently a robust clustering result. We set 0.5 as our PWOSS threshold in this example.

Subfigure 4.1 demonstrates the two successfully separated subbundles, CST and MCP, in two distinct colors. To investigate the quality of the clustering result, we compute one inter cluster (CST-MCP) and two intra cluster (CST-CST and MCP-MCP) PWOSS histograms illustrated in subfigure 3.9(b). It shows that the developed clustering algorithm classify the streamlines quite reliably, with the maximum inter cluster affinity being smaller than the minimum intra cluster affinity.

Further inspecting the CST-CST intra cluster histogram reveals two high peaks whose the midpoint is closer to zero than that in the previous CST-MCP histogram. We further group the CST tracts into two subbundles with a PWOSS threshold 0.95 which is suggested by the separation point between the two peaks. Figure 3.10 illustrated the two subbundles of the CST and the final three subclusters of the original CST-MCP composite tracts in subfigure 6.1(a). Subfigure 3.11(a) illustrates the inter and intra cluster PWOSS histograms of the generated two CST subbundles. It can be seen that the two peaks in the intra cluster CST-

CST histogram in subfigure 3.9(b) have been removed. This subpartition further reduces the variance of intra cluster affinity as well as making the maximum inter cluster similarity being smaller than the minimum intra cluster similarity. The two CST subbundles, which we will refer as short and long CST subbundles respectively, have almost equal intra but obviously distinct inter cluster lengths while sharing similar shapes and occupying close spatial positions. This suggests that our defined streamline length difference feature and subsequently the local similarity score play a major role in this subpartition. Histograms in subfigure 3.11(b) confirms this argument with the local similarity score contributing more than that of the global affinity score to classify these two subbundles. This information suggests that we can get a better PWOSS histogram if we assign more weight to the local similarity score than that to the global affinity measure, i.e., $\omega \approx 1$. This subbundling can hardly be done by measuring only the streamline pairwise distance [96] or using the visual dissection method [52]. The hierarchical clustering strategy is employed in this example using the intra bundle similarity histogram. We point out that the same subgrouping process can be applied to the MCP tracts as well. Since the most left peak in the MCP-MCP intra cluster PWOSS histogram is relatively low, one of the further clustered MCP subbundles is expected to have low cardinality.

3.5.3 CST-CPT-PTR Tracts

The second data set used in the experiment is composed with three types of projecting fiber tracts, CST, CPT and PTR. They all penetrate the internal capsule either between the thalamus and the putamen or between the caudate and the putamen. When approaching the cortex, they fan out to form the corona radiate.

As previously, we first calculate its PWOSS, local and global similarity scores and generate the their histograms in Figure 3.12. The information that three potential subbundles form this collective trajectories can be revealed from the the three obvious peaks in the PWOSS histogram. With any values in the two intervals between each two of the three

peaks, e.g., 0.6 and 0.9, being set as the PWOSS thresholds in clustering, we obtain two and three subbundles respectively. The results are shown in Figure 3.13. We directly get three subbundles here instead of using the hierarchical method in the previous CST-MCP example by exploiting the fact that both heights of the two midpoints belonging to different intervals are zero in the PWOSS histogram. Note that the same reliable clustering results can be achieved as well by using only the local similarity score in this case.

3.6 Discussion and Conclusion

In this work, we have developed a diffusion orientation based approach to segment a small number of reconstructed white matter tracts. We have modeled a streamline based on diffusion orientations, streamline length and geometric center. This objective representation has no specific dependence on a particular tratography algorithm. We have formed the pairwise tract similarity metric and its two constituents, the local and global affinity scores to quantify shape and spatial position relationships between two streamlines. Furthermore, we have described a novel scheme to find the matching starting points to compare two streamlines sharing no common ROI. Strategies have been developed to establish segment-wise correspondences between two streamlines under two different scenarios. The proposed approach is thus independent of user's placement of ROI(s), in addition to be able to handle tracts of unequal length. Experimental results show that this method is apt for clustering two or more fascicles of similar as well as different shapes. And it may provide an alternative to existing algorithms.

Compared to other methods, the success of our approach benefits from several factors. The first desirable feature is that this methodology shows the capability to segment both equal and unequal length tracts. The second attractive property is that our method handles streamlines sharing a specified ROI(s) [96] or none with different strategies because the similarity measures are independent of user's placement of selected ROI(s). Thirdly, the representation of a streamline as sets of straight line segments together with their lo-

cal diffusion orientations gives a streamline's both topological (connection between a pair of step points) and geometrical information (positions of step points) as shown in the experiments. Taking the advantage of the local diffusion orientation property, local shape similarities of two streamlines are evaluated by simply investigating the cosine values of the principal eigenvector pairs along the streamlines. Since these primary eigenvectors are already available before a tractography algorithm applied, the use of them does not incur extra computation loads. Next is that in the definition of PWOSS, the isolation of the local and global similarities gives us the flexibility to emphasize on either tract shape or position information, or both. With the geodesic parameter fitting, it may be possible to apply this methodology to across subject studies by normalizing the fitting arc length. Furthermore, our computed pairwise similarity score histogram has the potential to determine a reasonable number of clusters for a small number of streamlines. The reason is that it accounts for both inter and intra cluster affinities. Inner clusters within a coarse structure can be identified using the similarity score histogram as shown in the CPT-MCP example. This should produce a more consistent and meaningful clustering result than the methods that determine the number of clusters automatically. The similarity score histograms facilitates the choice of an appropriate PWOSS threshold for tracts isolation. The only parameter needs to be estimated in advance is the σ value in the utilized Gaussian kernel. This parameter can be determined by visually checking several PWOSS histograms in correspondence with different σ values. For instance, Figure 3.14 illustrated the effect of different σ values on PWOSS for the CST-CPT-PTR compound tracts. This example shows that the PWOSS histograms become stable when $\sigma \geq 20$. The σ value which can separate the PWOSS histogram peaks furthest would be the best one. ω value in Equation 4.12 can be inferred by probing the local and global similarity score histograms as demonstrated in the CST-MCP example.

For streamline segmentation purpose, a concern is the noise in the DTI data. Large arc unit in the fitting procedure can filter out the high frequencies in some extent. However,

this is achieved at the expense of loss of information regarding local properties of the tracts. We also can manually remove suspicious clusters, e.g., the short CST sub-bundle in Figure 3.10(a), by visual assessment.

Our method does have limitations, however. Low spatial resolution of DTI data and the limited robustness of currently used tractography algorithms at fiber junctions and in noisy regions may produce trajectories that are locally consistent but incorrectly connected. Our method is not capable to handle this situation. Even though no *a priori* anatomic knowledge about the entire tracts under consideration is required which is a prerequisite in some other publications [105], our technique does not guarantee that the isolated sub-bundles all have anatomical meanings. Thus, the quality of the clustering results depends on the validity of the input streamlines. The quality of the inputs is in turn determined by the quality of the DTI data and the tractography algorithm. The *a priori* anatomic knowledge of the whiter matter in question, e.g., the geometrical information of connected regions or a prototype of tracts, may be of great help in such situations.

The second shortcoming of this method is that the best σ, ω values, and the PWOSS threshold need to be interactively selected in advance by visually inspecting several similarity score histograms. This means that the PWOSS threshold and in turn the number of sub-bundles we expect to find have to be predefined. Though the approach we have taken is straightforward and generates robust streamline segmentation, it does cost more time than the automatic cluster number determination methods which is still a research problem in the field of tract segmentation. Another disadvantage to probe the number of clusters using the similarity score histogram is that we have to calculate all pairwise affinities though the all-or-zero clustering algorithm does not require it. This would cause some storage costs for large amounts of tracts. Of course, we can avoid the extra time and storage expenses by blindly setting the clustering parameters without the concern of achieving reasonable and meaningful results.

In future work, alternative tract representations could be considered in order to handle

branched streamlines. An appropriate rich representation of relationships between the topological and geometrical properties of matched neuronal paths across individual subjects is informative in its own right. It may alleviate the difficulty in tract group analysis.

In summary, the work presented here provides a tool to group white matter trajectories into sub-bundles using the diffusion orientation information carried in DTI data. With further development, it may ultimately be possible to produce a standard atlas as tract architecture references, similar to the currently used brain image templates. It thus has potentials to quantify the deformation of white matter fibers under certain pathologies and brain diseases, e.g., tumor, or for clinical group analysis. In group studies, fiber tracts from a new individual could be matched to an atlas or a prototype. The methodology could thus be applied to in vivo data with the aim of classifying patients from normal controls by differentiating statistically normal and abnormal tract shapes and configurations.

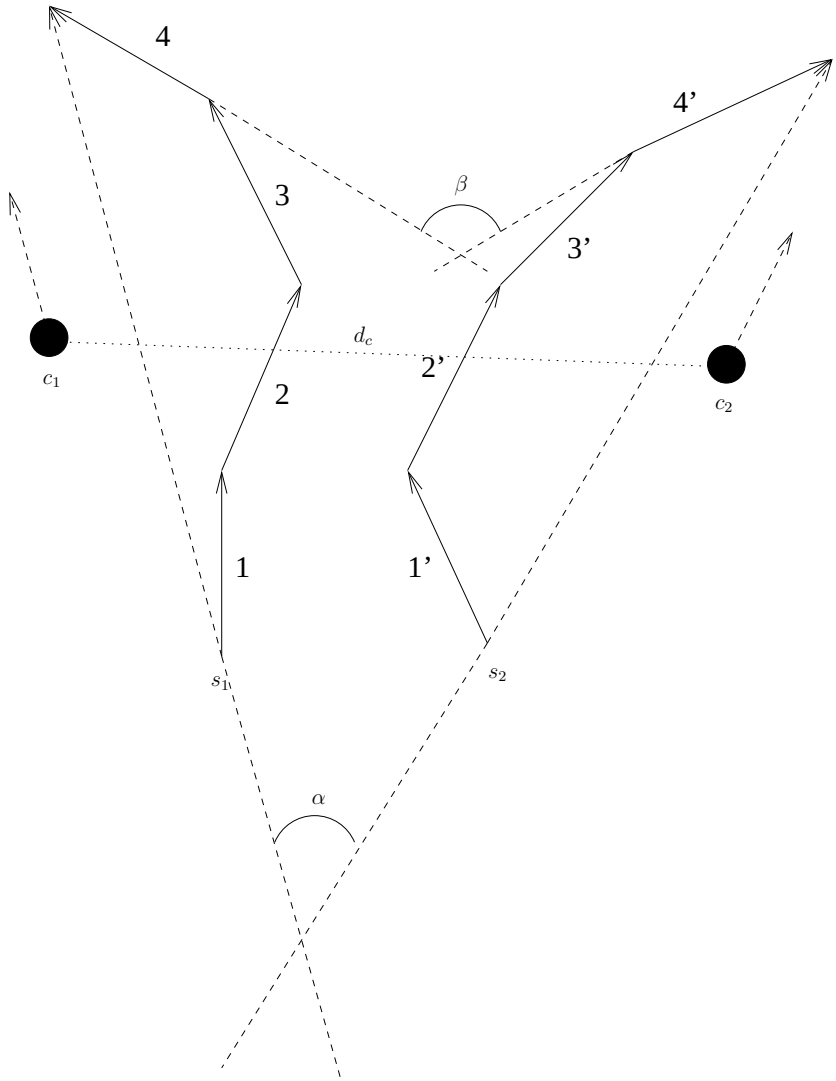

Figure 3.3: Illustration of two streamlines s_1 and s_2, their geometric centers, local and global diffusion orientations. Two geometric centers, c_1 and c_2, are marked as solid circles. Arrows of straight line segments indicate one of the two possible diffusion directions. β_i is the angle between the i-th pair of corresponding segments of the two compared streamlines. α is the angle between the two global diffusion orientations. Each streamline's global diffusion orientation is parallel to the linear line directly connecting its two end points. Lengths of s_1 and s_2 are both 4 (4 linear segments).

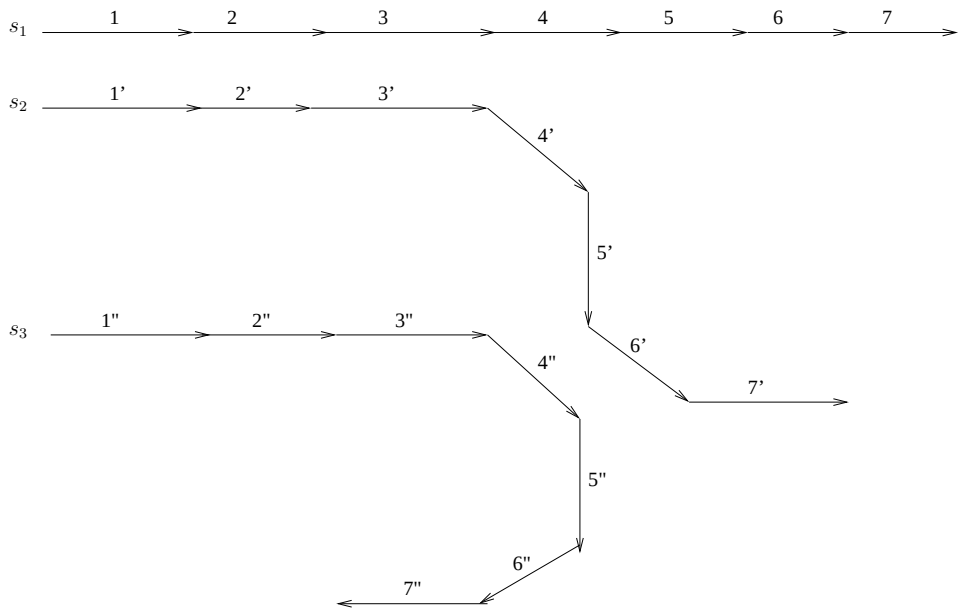

Figure 3.4: Demonstration of the advantage of the signed cosine value over the absolute cosine value. Three streamlines, s_1, s_2 and s_3, all have a length of 7. The numbers represent the indices of streamline segments. Arrows represent local primary eigenvectors. s_1, s_2 and s_3 move in the same direction at the beginning. s_1 and s_2 terminate in the same direction while s_3 turns into the opposite direction.

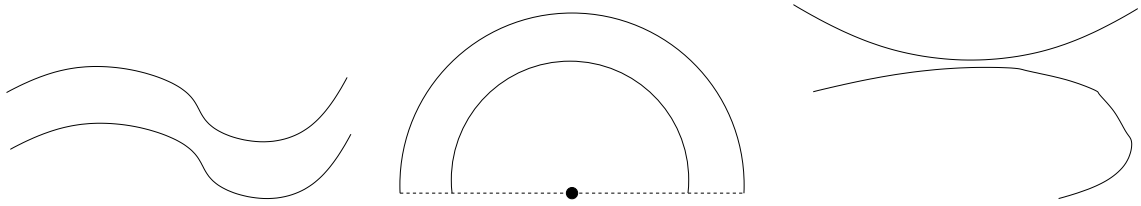

(a) $S_l = 1,\ S_g < 1$ (b) $S_l < 1,\ S_g = 1$ (c) $S_l < 1,\ S_g < 1$

Figure 3.5: Demonstration of the affinity scores of the two components, S_l and S_g, of PWOSS affected by different relationships between a streamline pair. In subfigure (b), the solid circle is the geometric center of both streamlines. The dotted line represents their global diffusion orientations.

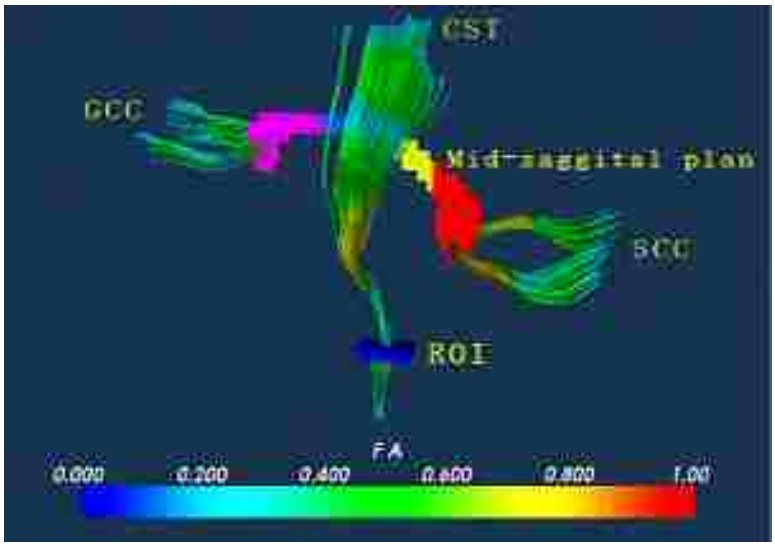

Figure 3.6: Illustration of multiple streamline bundles sharing no common ROI.

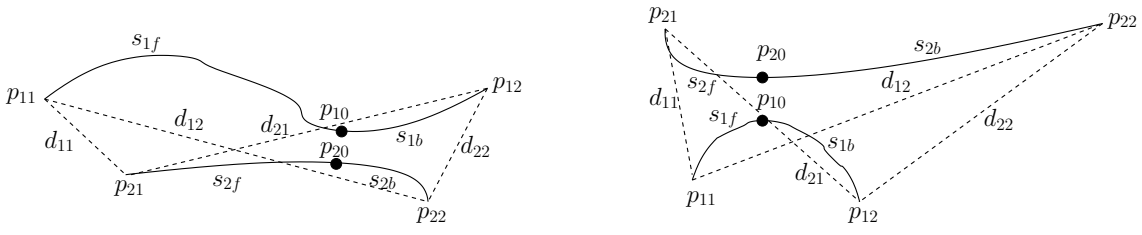

Figure 3.7: Graphical illustration of substreamline correspondences. In (a), the two end points of streamline s_1, $(p_{11},\ p_{12})$, are close to two different end points of streamline s_2. In (b), both of the two end points of s_1 are close to a common end point of s_2, i.e., p_{21}. $(s_{1f} \leftrightarrow s_{2f},\ s_{1b} \leftrightarrow s_{2b})$ is the substreamline correspondence for both (a) and (b).

(a) CST and MCP

(b) CST and MCP in two clusters

Figure 3.8: The CST-MCP compound trajectories and two clustered sub-bundles. (a) is the original tracts before clustering. (b) shows the separated two subgroups, CST and MCP, in two different colors. $\sigma = 100$ and the PWOSS threshold is 0.5. $\omega = 0.5$.

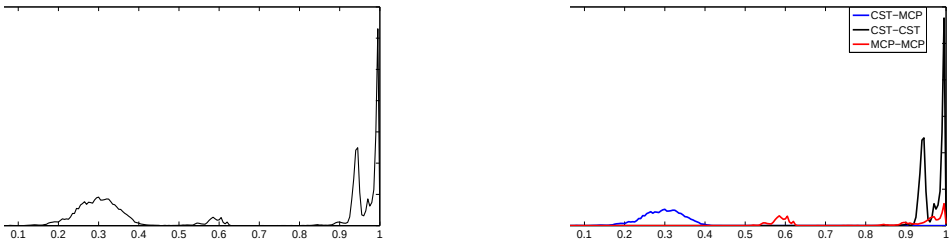

(a) PWOSS of CST-MCP tracts

(b) Inter and intra cluster PWOSS of CST-MCP tracts

Figure 3.9: Histograms of the calculated PWOSSs for the CST-MCP tracts bundling. $\sigma = 100$ and the PWOSS threshold is 0.5. $\omega = 0.5$. (a) shows the calculated PWOSS histogram based on Equation 4.12 for the CST-MCP tracts. The inter and intra cluster PWOSS histograms after clustering are illustrated in (b)

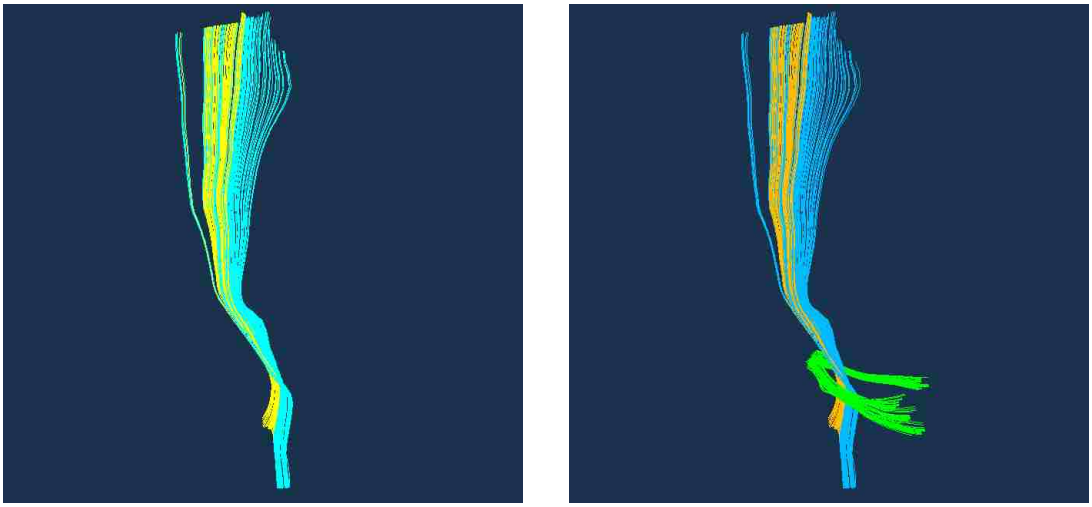

(a) CST and MCP

(b) CST and MCP in three clusters

Figure 3.10: Classification of the CST into two subbundles. (a) shows the two CST subbundles, short and long CST, in two different colors. $\sigma = 100$ and the PWOSS threshold is 0.95. $\omega = 0.5$. (b) is the clustered 3 bundles from the original tracts in subfigure (a).

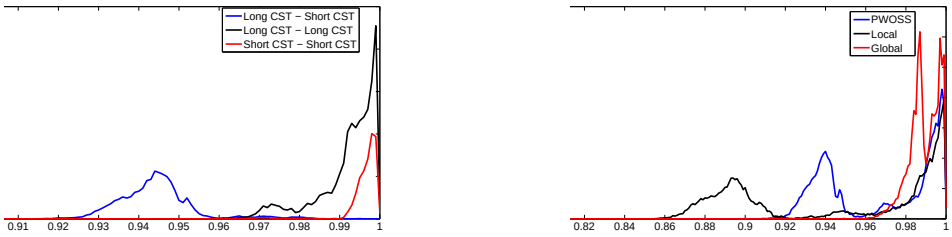

(a) The intra and inter cluster histograms of PWOSSs of the short and long CST subbundles

(b) PWOSS, local, and global similarity score histograms of the CST bundle.

Figure 3.11: $\sigma = 100$ and $\omega = 0.5$. (b) shows that the local similarity score contributes more than that of the global affinity score in the classification.

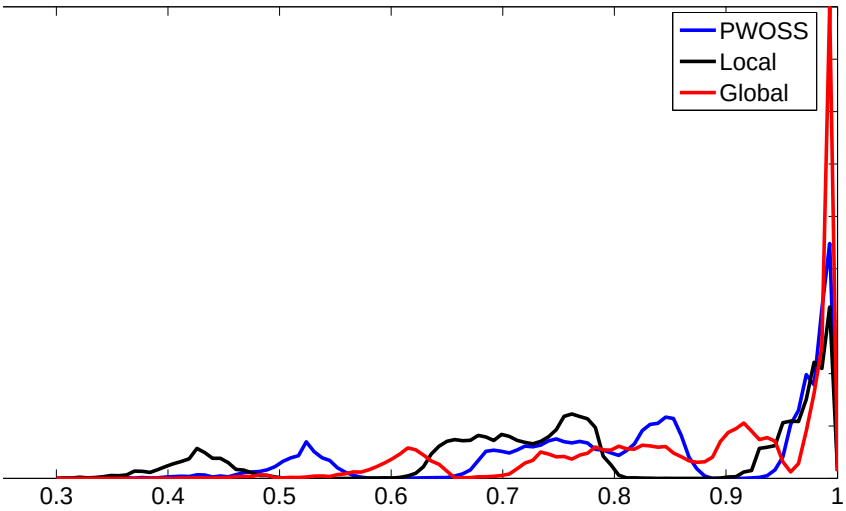

Figure 3.12: PWOSS, local and global similarity histograms of the CST-CPT-PTR compound tracts. The PWOSS score suggests the similarity thresholds to classify the tracts into two or three sub-bundles. $\sigma = 30$ and $\omega = 0.5$.

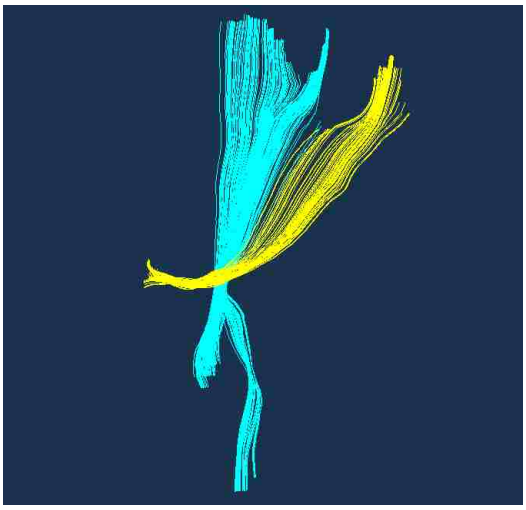

(a) Tracts in two subbundles. The PWOSS threshold is 0.6.

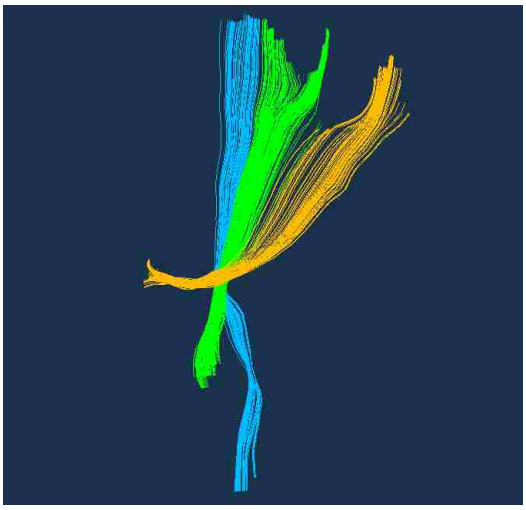

(b) Tracts in three subbundles. The PWOSS threshold is 0.9.

Figure 3.13: Partitions of the CST-CPT-PTR compound tracts into two and three subbundles. $\sigma = 30$ and $\omega = 0.5$ for both (a) and (b).

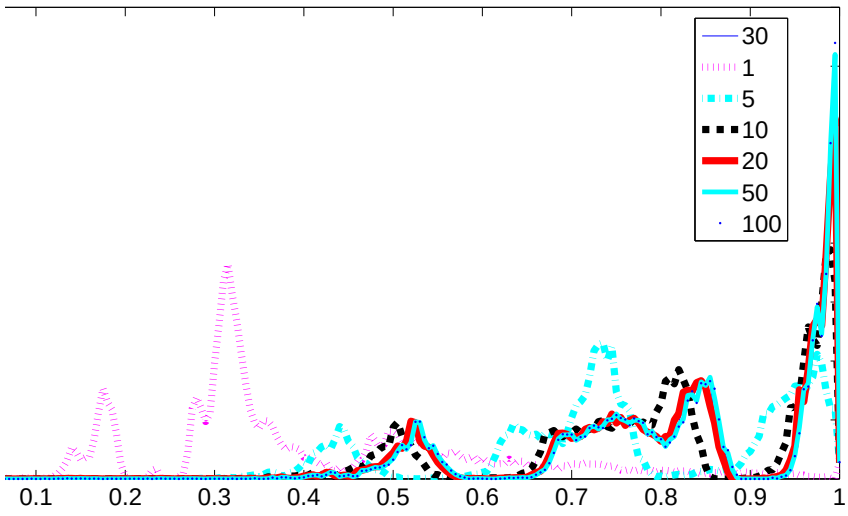

Figure 3.14: Effects of different σ values on the PWOSS for the CST-CPT-PTR composite tracts. The PWOSS histograms keep almost unchanged for $\sigma \geq 20$.

4 Modeling White Matter Tract Shape Patterns using Fourier Descriptors

4.1 Outline

In this chapter, we first briefly give an introduction of the Fourier transform and its shape representation applications in other research areas. To apply the Fourier transform technique in the representation of reconstructed white matter tracts, we then present and evaluate several tract shape signatures. The performance of Fourier descriptors with different tract signatures are assessed with white matter tracts reconstructed from real DTI data. In the end, we give discussions and concluding remarks of this chapter.

4.2 Introduction

For visual and quantitative analysis of complicated three dimensional (3D) white matter tracts, efficient computational tools are essential to model and segment reconstructed white matter trajectories into specific clusters or bundles to gain clinical insight. Over the past few years, a number of white matter tract segmentation schemes have been published. However, in the literature, there appears to be disproportionately more effort and emphasis placed on the development of better clustering algorithms and less on better representations of reconstructed white matter tracts, even though the latter is more critical in determining the success of a tract clustering strategy. The popular distance measures capture the local relationship but tends to lack the ability to capture the global configuration of fiber tracts. The same applies to other proposed shape signatures such as curvature and torsion. They are essentially local representations of tract shape features and are thus sensitive to noise which is an inherent problem in DTI. Secondly, distance measures are tract pair-wise metrics. If any one tract has been replaced or removed, then the distance measures have to be recalculated. Thus they are mutual and temporal. Another property of the tract local representation is that it is subject dependent. This characterization makes it difficult to be applied to the clinical practice of group analysis.

The challenge that we face is to model a fiber tract with a representation method to separate white matter tracts belonging to distinct clusters while keeping tracts of the same cluster close by. The tract representation should eliminate the need to establish matching correspondences between randomly configured tracts generated from whole brain tracking. Since the procedure to establish intra and inter subject tract correspondences incurs huge even formidable computational cost when we segment a large amount of tracts such as the scenario in whole brain tractography. It would be especially desirable if this representation can be normalized and easily extended to inter subject clustering for group analysis which is more important than the intra subject clustering in clinical studies.

In this work, we aim to find an effective white matter tract and tract representation which has enhanced noise resistance and potential to facilitate clinical group analysis of DTI data. To achieve these goals and to overcome drawbacks of local shape signatures, unlike traditional techniques, we introduce a technique to model and segment fiber tracts by using Fourier descriptors derived from different shape signatures. We split a tract representation into two separate parts, shape and position characteristics. Especially, we employ Fourier descriptors to quantify a fiber tract's shape signatures. Fourier descriptors have been widely used in shape coding [107], shape analysis [108] and shape retrieval [109] in computer vision community since they render well both representation and normalization of a shape. The first few low frequency terms of Fourier series capture the more general shape properties while the higher frequency terms capture finer shape details. As an integral, Fourier descriptors not only preserve the tract shape information but also overcome the noise sensitivity in shape signature representations. Another advantage of Fourier descriptors is that features extracted from Fourier approach can be normalized so that we can easily handle the effect of rotation, translation and scaling. They thus bear the potential to be extended into fiber tract recognition and detection across subjects for group analysis.

Next, we present the modeling scheme to quantify the shape of white matter tracts reconstructed from DTI data and cluster them into bundles using Fourier descriptors. We

characterize a tract's shape by using Fourier descriptors which are effective in capturing shape properties of fiber tracts. Fourier descriptors derived from different shape signatures are analyzed. Clustering is then performed on these multi-dimensional features in conjunction with geometric centers using a k-means like threshold based approach.

4.3 Methods

4.3.1 White Matter Tract Parameter Fitting

The backward streamline based DTI tractography technique proposed by Mori and van Zijl [39] is employed in this analysis to reconstruct white matter fiber tracts. This tractography technique produces fiber tracts as spatial curves in the three dimensional space with unequal separation distances between successive step points. Fourier transform approach is dependent on the parameterization of the curves. This requires the parameterization to be standardized. For this reason, all reconstructed tracts are fitted using a fixed geodesic arc length. Distinct fiber tracts have equal length unit but usually different numbers of step points.

4.3.2 Shape Signatures

Each step point on a fiber tract has its three dimensional coordinates representing its spatial position and a principal eigenvector indicating the local diffusion orientation in a specific voxel it falls in. Based on the spatial position and orientation properties, three shape signatures are considered in this paper. They are center shifted coordinates, central distance and central angle dot product.

Center Shifted Coordinates

A tract's center shifted coordinates are its three dimensional coordinates shifted according to its geometric center to eliminate the effect of bias [110]. Assume $(x,\ y,\ z)$ are the three dimensional coordinates of a step point on a fiber tract. The corresponding center shifted coordinates are $(x - x_c,\ y - y_c,\ z - z_c)$, where $(x_c,\ y_c,\ z_c)$ is the geometric center of the

fiber tract which is the average of coordinates of the tract step points

$$x_c = \frac{1}{n}\sum_{i=0}^{n-1} x_i, \quad y_c = \frac{1}{n}\sum_{i=0}^{n-1} y_i, \quad z_c = \frac{1}{n}\sum_{i=0}^{n-1} z_i. \tag{4.1}$$

where n is the number of step points of a fiber tract. This shift makes the coordinates invariant under translations.

Central Distance

The central distance is the distance of the tract step points from the geometric center $(x_c,\ y_c,\ z_c)$ of the tract

$$d_c = \sqrt{(x - x_c)^2 + (y - y_c)^2 + (z - z_c)^2}. \tag{4.2}$$

The subtraction of the geometric center, which reflects a tract's spatial position, from step points makes the central distance invariant under translations as well.

Central Angle Dot Product

A fiber tract's shape can also be represented by its local diffusion orientations. But these orientations are not invariant to either translations or rotations. To overcome this downside, we first define a fiber tract's global diffusion orientation concept as the accumulation of local diffusion orientations intrinsic to step points along a fiber tract. This global diffusion orientation is similar to the cumulative angular function defined by Zahn and Roskies [111] for closed planar curves. It is the net amount of diffusion orientation difference between the two end points of a fiber tract. Assume $e = \{e_0,\ e_1,\ \ldots,\ e_{n-1}\}$ is the set of local diffusion orientations of a fiber tract, then the global diffusion orientation e_g is given by

$$e_g = \sum_{i=0}^{n-1} e_i. \tag{4.3}$$

A voxel's diffusion orientation e_i is defined as its associated principal eigenvector. However, they are not equivalent in the sense that a diffusion orientation is symmetrically bi-directional while a principal eigenvector is directional. In order to get the correct global

orientation e_g, we need to check the directional consistency of the principal eigenvectors. The strategy is similar to that finding the local tracing direction in streamline based DTI tractography [27, 39]. In detail, we start from any one of the two end points of a fiber tract and move along its successive step points. If the dot product between the principal eigenvectors of the starting point and the next point is negative, we reverse the principal eigenvector of the next point. Then we move forward following the direction of the principal eigenvector to the next point and repeat the process, until reach the last step point of the tract.

The central angle dot product is the absolute value of the dot product between a step point's local diffusion orientation and the global diffusion orientation of the tract

$$\frac{|e_i^T \cdot e_g|}{\|e_i\|\|e_g\|}.$$

This 1D shape signature is invariant under translations and rotations.

Discrete Fourier Transform

We compute the discrete Fourier transform of a tract for each of the shape signatures described above as

$$FD(k) = \frac{1}{n}\sum_{i=0}^{n-1} s(i)\exp(\frac{-j2\pi ki}{n}),\ k = 0, 1, \ldots, n-1 \tag{4.4}$$

where $s(i),\ i = 0, 1, \ldots, n-1$, is a shape signature at the ith point, and $j = \sqrt{-1}$. The coefficients $FD(k),\ k = 0, 1, \ldots, n-1$, are called Fourier descriptors of the shape of a fiber tract. Since the shape signatures that we introduced are all real values, there are only $n/2$ different frequencies in the discrete Fourier transform. If n is an odd number, the number of different frequencies is $(n+1)/2$. In the following discussion, we assume that n is even for convenience. Therefore, only a half of the Fourier descriptors in Equation 6.1 are needed to describe the shape pattern of a fiber tract.

Fourier descriptors transform the fiber tract shape from the spatial domain into a frequency domain. This eliminates the difficulty to establish the matching correspondence

between two randomly organized fiber tracts in spatial domain. The number of coefficients from Fourier transform is usually large, but a small subset of these coefficients is sufficient to capture the general shape features of a fiber tract. We show in later that this small subset of coefficients is also adequate to identify one fiber tract from others. The coefficients corresponding to very high frequencies are not so helpful in fiber tract shape differentiation and subsequently for fiber tract clustering. The reason is that fiber tracts are usually smooth since sharp turns are avoided in their reconstruction process [27, 39]. These high frequency components can be ignored without significant accuracy loss for fiber tract clustering. The lower order components also help filter out noise dependent perturbations. As a result, the dimension of Fourier descriptors used for fiber tract clustering are significantly reduced. In addition, two fiber tracts compared based on the Fourier descriptors do not have to have the same numbers of step points.Consequently, Fourier descriptors can be employed in matching of fiber tracts with unequal length.

Invariance Normalization

In order to easily extend our method to fiber tract matching across subjects, the shape representations should be invariant to translation, rotation and scaling. Shape representation invariance is difficult to achieve in spatial domain. Especially the rotation invariance needs large amounts of computation. On the other hand, Fourier descriptors significantly reduce the difficulty to achieve invariance [112]. If a fiber tract is linearly transformed, Fourier transform keeps the same linearity of the transformation. All the three shape signatures introduced above are invariant under translation. Their corresponding Fourier descriptors are also translation invariant. Rotation invariance of the Fourier descriptors is achieved by discarding their phase information and keeping only their magnitude components [112]. We represent a Fourier descriptor's magnitude as $|FD|$ in the following.

For the center shifted coordinates, we treat each of the three coordinate components of the parameterized fiber tract, $x - x_c$, $y - y_c$, and $z - z_c$, as three one dimensional signals.

After applying discrete Fourier transform on each of them individually, we get three sets of Fourier descriptors, $FD_x(k)$, $FD_y(k)$ and $FD_z(k)$. We use the Euclidean norm as the one dimensional descriptor as [101]

$$|FD(k)| = \sqrt{|FD_x(k)|^2 + |FD_y(k)|^2 + |FD_z(k)|^2}, \tag{4.5}$$

where $k = 0, 1, \ldots, (n/2 - 1)$. $FD(0)$ is the direct current (DC) component which is a real value and represents the mean position [112]. It is not useful for shape representation and is thus ignored. $FD(1)$ indicates a fiber tract's scale information. To achieve scaling invariance, we divide all other Fourier descriptors by $FD(1)$. Finally, Fourier descriptors derived from center shifted coordinates are

$$\frac{|FD(2)|}{|FD(1)|}, \frac{|FD(3)|}{|FD(1)|}, \ldots, \frac{|FD(n/2-1)|}{|FD(1)|}. \tag{4.6}$$

For central distance and central angle dot product, scaling invariance is achieved by dividing all other Fourier descriptors by $FD(0)$, the DC component. Their Fourier descriptors are given by

$$\frac{|FD(1)|}{|FD(0)|}, \frac{|FD(2)|}{|FD(0)|}, \ldots, \frac{|FD(n/2-1)|}{|FD(0)|}. \tag{4.7}$$

In the following discussion, we represent a normalized descriptor as $f(k)$ for convenience. In detail, $f(k) = |FD(k)|/|FD(1)|$ and $k = 2, 3, \ldots, (n/2 - 1)$ for the center shifted coordinates. $f(k) = |FD(k)|/|FD(0)|$ and $k = 1, 2, \ldots, (n/2 - 1)$ for the other two shape signatures.

Now, the normalized Fourier descriptors generated from all the three shape signatures are invariant under translation, rotation and scaling. Each tract's shape is featured by a shape vector, f, composed of a set of normalized Fourier descriptors

$$f = [f(m),\ f(m+1),\ \ldots,\ f(n/2)]. \tag{4.8}$$

where n is the number of points of a fiber tract. This number may not be equal among tracts. m is the starting index of the descriptors. In particular, $m = 2$ for the center shifted coordinates and $m = 1$ for the other two shape signatures.

4.3.3 Tract Similarity and Clustering

For a reference fiber tract indexed by a shape vector $f_r = [f_r(m),\ f_r(m+1),\ \ldots,\ f_r(L)]$ and a candidate fiber tract indexed by a shape vector $f_c = [f_c(m),\ f_c(m+1),\ \ldots,\ f_c(L)]$, the shape similarity S_s is calculated by Gaussian kernel of the Euclidean distance as

$$S_s = \exp\left(-\frac{d_f}{2\sigma^2}\right), \tag{4.9}$$

and

$$d_f = \sqrt{\sum_{i=m}^{L} |f_r(i) - f_c(i)|^2}, \tag{4.10}$$

where L is the truncated number of the Fourier descriptors used and m is the starting index of descriptors.

For intra subject clustering, we calculate the spatial position similarity between two fiber tracts as

$$S_p = \exp\left(-\frac{d_m}{2\sigma^2}\right), \tag{4.11}$$

where $d_m = \|c_1 - c_2\|$ is the Euclidean distance between the two geometric centers, c_1 and c_2, of the two fiber tracts.

Finally, we combine them together to define the overall similarity score S between two fiber tracts as

$$S = \omega S_s + (1-\omega) S_p, \tag{4.12}$$

where ω is a weight factor and takes values between 0 to 1. For S, S_s and S_p, a higher value indicates a stronger match, and a lower value reflects a weaker match. We then apply a k-means like threshold based approach to perform tract clustering.

4.4 Experiments and Results

4.4.1 DTI Data

The DTI data used in this study are from health controls which are described in sections 1.3.2 and 2.4.1.

4.4.2 Experiments

We first evaluated the capability of the Fourier descriptors to distinguish different shapes by using a fiber tract collection composed of the corticospinal tract (CST) bundle and the medial cerebellar peduncle (MCP) bundle. $f(2)$ to $f(29)$ were used for the center shifted coordinates. $f(1)$ to $f(29)$ were used for the other two shape signatures. In this experiment, we only applied the Fourier descriptors to differentiate these two fiber bundles, and we set $\omega = 1.0$ and $\sigma = 1$. The clustering result shows that the tracts were grouped into two plausible bundles, CST and MCP. Figure 4.1 illustrates the segmented tracts in different colors in a sagittal view.

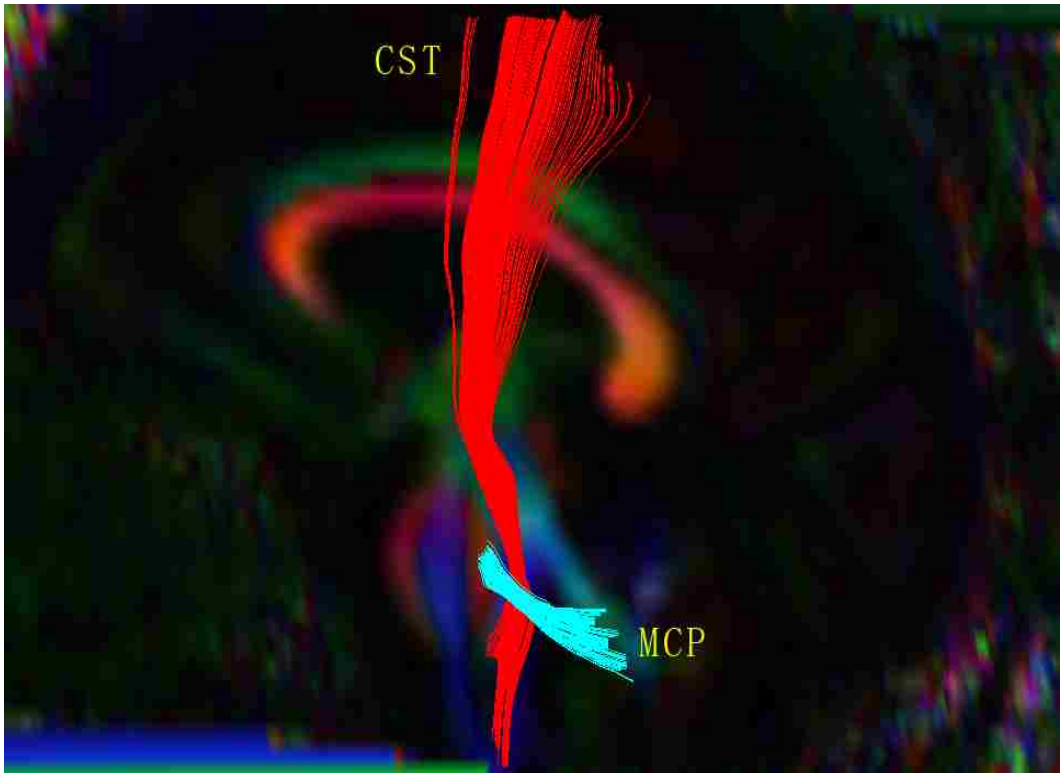

Figure 4.1: Illustration of the clustering result of CST-MCP tract collection in a sagittal view. $\omega = 1.0$ and $\sigma = 1$. The number of the input fiber tracts is 307. The resulting CST and MCP bundles have 199 and 108 tracts each.

However, shape discrimination of these Fourier descriptors may be different. Figures 4.2, 4.3, and 4.4 show the calculated Fourier descriptors for all fiber tracts in this collection. They reveal that Fourier descriptors derived from the center shifted coordinates

have the highest discrimination ability among the three shape signatures in this specific test while the others remain almost the same. Furthermore, with $\omega = 1.0$ and $\sigma = 1$, the only parameter needed to be adjusted in clustering is the similarity threshold. Similarity threshold intervals to get reasonable partitions are $[0.89, 0.96]$ for the center shifted coordinates, $[0.89, 0.92]$ for the central angle dot product and $[0.93, 0.97]$ for the central distance. Fourier descriptors transformed from the center shifted coordinates also have the widest value range.

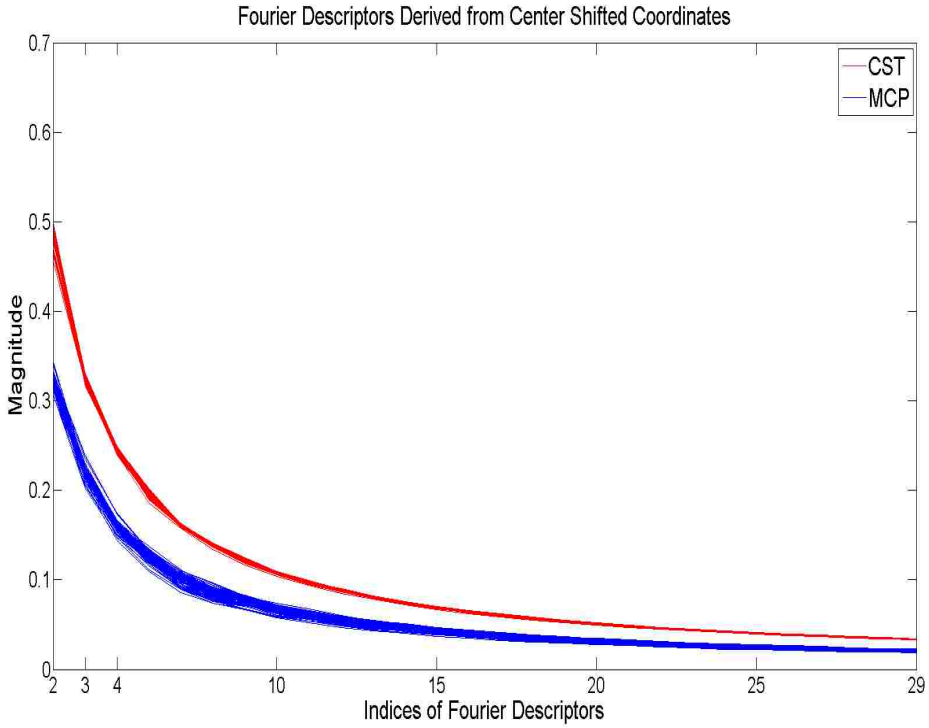

Figure 4.2: Fourier descriptors derived from the center shifted coordinates. $f(2)$ to $f(29)$ are used in clustering.

We further apply these Fourier descriptors to segment a more complicated fiber tract collection and the clustering result is shown in Figure 4.5. Fourier descriptors fail to distinguish this set of tracts into plausible bundles without the help of the spatial position feature ($\omega = 1.0$). With $\omega = 0.5$ and $\sigma = 20$, Fourier descriptors stemmed from all the three shape signatures performed successfully with minor differences on the number of output

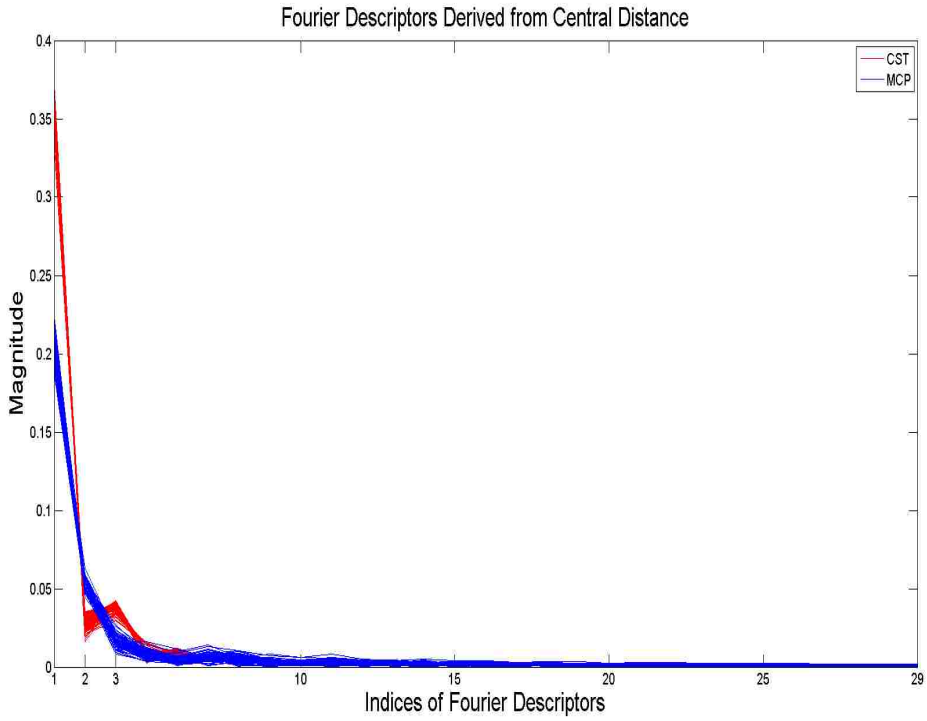

Figure 4.3: Fourier descriptors derived from the central distance. $f(1)$ to $f(29)$ are used in clustering.

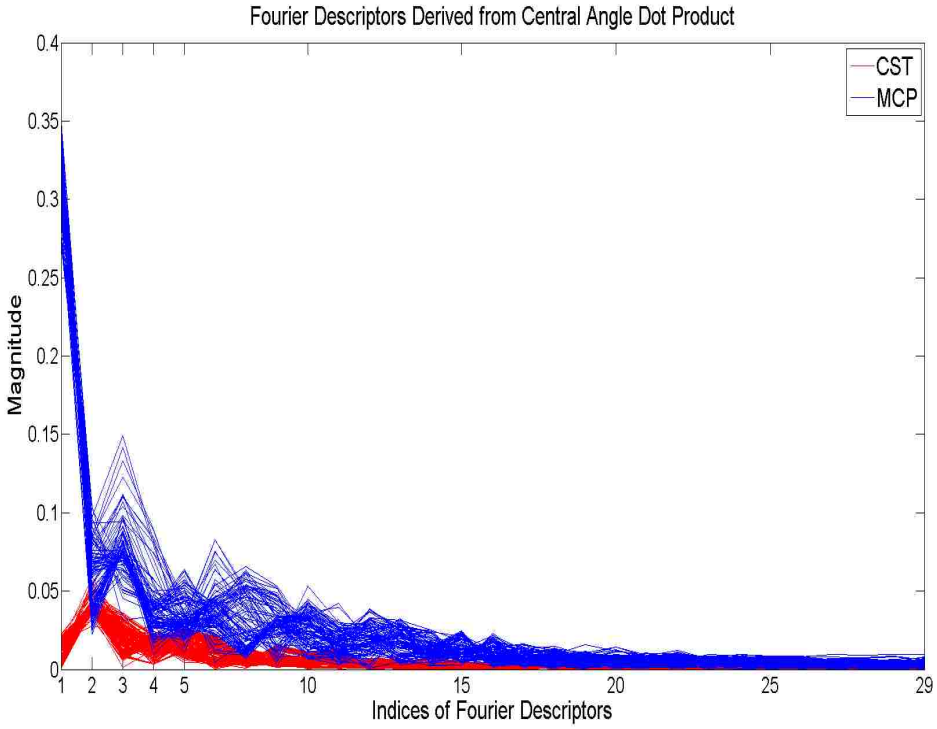

Figure 4.4: Fourier descriptors derived from the central angle dot product. $f(1)$ to $f(29)$ are used in clustering.

fiber tracts. In this test, $f(2)$ to $f(29)$ were used for the center shifted coordinates. $f(1)$ to $f(29)$ were used for the other two shape signatures.

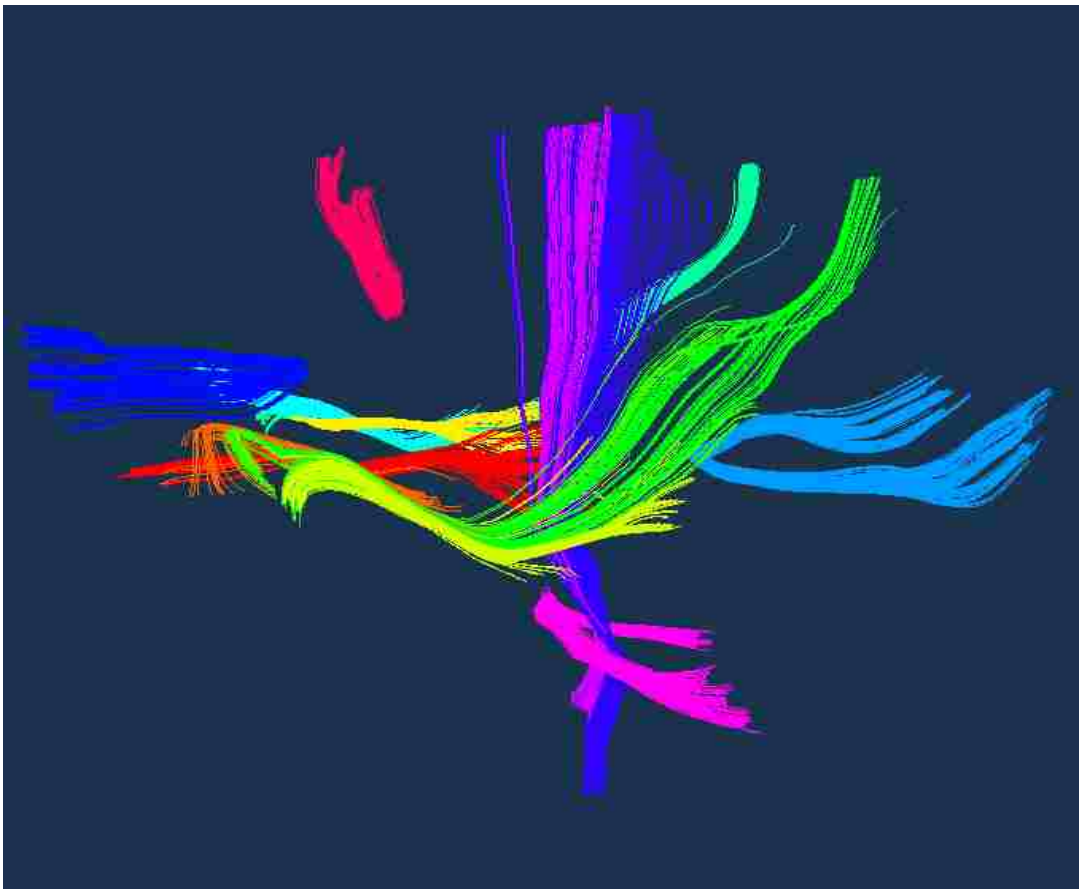

Figure 4.5: Illustration of the clustering result of tracts composed of total 13 clusters in different colors. Fourier descriptors are derived from the center shifted coordinates shape signature. $\omega = 0.5$ and $\sigma = 20$. $f(2)$ to $f(29)$ were used for clustering. The number of input tracts is 1379 and 1341 of them are grouped into 13 clusters. Clusters with less than 10 fiber tracts are ignored.

4.5 Discussion and Conclusion

In this chapter, we have successfully modeled the shape of white matter fiber tracts using Fourier descriptors derived from three different shape signatures. Their performance in fiber tract shape differentiation and clustering were analyzed. Our preliminary results show that they are all adequate to capture shape features for fiber tract identification. Among them, the center shifted coordinate signature is the best in our test. Our experimental

results show that Fourier descriptors generated from different shape signatures can play an important role in fiber tract shape recognition and clustering.

One important clinical application of DTI tractography is the identification of fiber tracts across subjects for group analysis. Being invariant under translations, rotations and scaling, the Fourier descriptors can be a good candidate for clustering fiber tracts across subjects.

Our method does have limitations, however. Low spatial resolution of DTI data and the limited robustness of currently used tractography algorithms at fiber junctions and in noisy regions may produce trajectories that are locally consistent but incorrectly connected. Our method cannot distinguish these fibers at this time. The a priori anatomic knowledge of the whiter matter in question, e.g., the geometrical information of connected regions or a prototype of tracts, may be of great help in such situations.

In summary, the work presented in this study provides an approach to quantify the shape of white matter fiber tracts without the difficulties, i.e., spatial normalization, happened in spatial domain. The technique has potentials to quantify the deformation of white matter fibers under certain pathologies and brain diseases, e.g., tumor, or for clinical group analysis. In group studies, fiber tracts from a new individual could be matched to an atlas or a prototype. The methodology could thus be applied to in vivo data with the aim of classifying patients from normal controls by differentiating statistically normal and abnormal tract shapes and configurations.

5 White Matter Tracts Clustering using Bayesian Inference to Facilitate Group Analysis

5.1 Introduction

In recent years, analysis of quantitative information extracted from DTI and white matter has received extensive attentions in order to understand a variety of brain diseases and disorders such as Alzheimer's disease, multiple sclerosis and schizophrenia. DTI based tractography enables selective reconstruction of specific neuronal pathways [27, 35, 37] and has been used to visualize brain white matter fiber tracts to facilitate our understanding of brain structural connections in clinical studies such as neurosurgery planning. However, to reconstruct several tens of fiber bundles for each of the several tens of subjects in group analysis is tedious, time consuming, subjective and sometimes impractical. In this scenario, it is desirable to perform the whole brain fiber tracking first for all subjects under study. Afterwards, we group the reconstructed fiber tracts into anatomically meaningful bundles and simultaneously remove the anatomically incorrect tracts, i.e., outliers. Nevertheless, in the design of the algorithm to perform this task, there are two major challenges we need to overcome. The first is the computation cost. In the whole brain fiber tracking, the amount of reconstructed fiber tracts is generally very large, i.e., in the order of several tens of thousands. Though there exist techniques to reduce the amount of reconstructed fibers, the tradeoff is that some fiber bundles will not be able to be reconstructed. Furthermore, each fiber tract may consist of several hundreds of step points. If we conduct the clustering by computing the step point-wise similarity or distance between all possible trajectory pairs, the computation complexity may be prohibitive in this case. The second challenge is that the tractography algorithm is usually inaccurate and thus generates a large amount of outliers. We would like the clustering algorithm to be able to handle the outliers effectively. Except that, we hope the clustering accuracy will not be affected by the existence of the outliers. But the practical situation is that most of the proposed fiber clustering methods to date, as we have described in previous chapters, are based on the correspondence and

comparison of the the step points along fibers and lack the desirable capability of handling outliers. This motivates us to find a practical and efficient way instead.

In this work, we aim to develop a clustering framework to facilitate the single subject or group quantitative analysis of the reconstructed white matter fiber bundles in the DTI data based on a certain level of *a priori* knowledge. The goal is to cluster fiber tracts into a number of interested target fiber bundles instead of random groups. The above mentioned two major challenges are addressed in the framework. Different strategies are presented to handle the scenarios dependent on more or less the *a priori* knowledge contained in the target fiber bundles. In both of the two cases, the heavy computing burden is largely reduced by eliminating the need either to establish the point-wise correspondence between trajectory pairs or to perform the calculation at the level of the step points along fiber tracts. We achieve this goal by introducing the fiber tract representation in the format of a number of Fourier shape descriptors and geometric features. This representation provides the framework the theoretical ground to reduce the noise effect inherent to the DTI data and the desired differentiating ability. In the framework, the distribution of fiber tracts is described by a multivariate Gaussian mixture model. This statistical parametric model makes it feasible to exploit the *a priori* knowledge in the format of mean and covariance of fiber bundles. Fiber tracts do not fit into any of the target bundles are labeled as outliers. Anatomically meaningless fiber bundles are mostly avoided since the involvement of the *a priori* knowledge. In the case that we have little *a priori* knowledge, we use the expectation-maximization (EM) algorithm to perform the maximum likelihood estimation (MLE) to approximate the class parameters and label fiber tracts. On the other hand, if a set of fiber bundle atlas are given, i.e., the class parameters are known, we directly label each trajectory by finding its maximum of the *a posterior* Bayesian probabilities among all the target classes. The method has the potential to incorporate new found fiber bundle patterns into the existing atlas. It as well has the flexibility to conduct the grouping on a portion or all of the fiber tract set one time to accommodate different situations. In both cases,

outliers are handled by easily setting a probability threshold. Experiment in real DTI data set is conducted to evaluate the performance of the proposed approach.

In this chapter, we first go over the mathematical basics and the proposed methodology. Then we present the experimental results obtained. At the end, we give discussions and conclusion remarks of this work.

5.2 Methods

5.2.1 The Statistical Model

Suppose we have a finite data set of observations $\mathcal{D}$ of N fiber tracts $\mathcal{D} = \{\mathbf{x}_1, \ldots, \mathbf{x}_N\}^{\mathrm{T}}$. Each fiber tract is denoted by a D-dimensional feature vector $\mathbf{x}_n = [x_{n1}, \ldots, x_{nD}]$. Here, $n = 1, \ldots, N$. Then we can mathematically form the data set $\mathcal{D}$ as an $N \times D$ matrix $\mathbf{X} \equiv \{\mathbf{x}_1, \ldots, \mathbf{x}_N\}^{\mathrm{T}}$. Each row of $\mathbf{X}$ represents one single fiber tract. And its n^{th} row is given by $\mathbf{x}_n$. We further assume that we have a finite target fiber bundle set $\mathcal{C}$ of K fiber bundles $\mathcal{C} = \{C_1, \ldots, C_K\}$. Each fiber tract is to be labeled into one of the K target fiber bundles or labeled as an outlier.

Without loss of generality, we assume that the N fiber tracts are drawn independently from the distribution. In other words, they are statistically independent and identically distributed (i.i.d.). And fiber tracts in each of the K bundles follow the Gaussian distribution of positions. That is, the distribution of the fiber tracts in the k^{th} target fiber bundle takes the form of the multivariate Gaussian

$$\mathcal{N}(\mathbf{x}_n|\boldsymbol{\mu}_k, \boldsymbol{\Sigma}_k) = \frac{1}{(2\pi)^{D/2}} \frac{1}{|\boldsymbol{\Sigma}_k|^{1/2}} \exp\left\{-\frac{1}{2}(\mathbf{x}_n - \boldsymbol{\mu}_k)^T \boldsymbol{\Sigma}_k^{-1}(\mathbf{x}_n - \boldsymbol{\mu}_k)\right\} \tag{5.1}$$

where $k = 1, \ldots, K$, $\boldsymbol{\mu}_k$ is a D-dimensional feature mean vector, $\boldsymbol{\Sigma}_k$ is the $D \times D$ feature covariance matrix, and $|\boldsymbol{\Sigma}_k|$ represents the determinant of $\boldsymbol{\Sigma}_k$. For our convenience, we represent the feature mean of all the K target clusters as a $K \times D$ matrix $\boldsymbol{\mu} \equiv \{\boldsymbol{\mu}_1, \ldots, \boldsymbol{\mu}_K\}^{\mathrm{T}}$ with rows $\boldsymbol{\mu}_k^{\mathrm{T}}$. For the covariance matrix, we use the notation $\boldsymbol{\Sigma} \equiv \{\boldsymbol{\Sigma}_1, \ldots, \boldsymbol{\Sigma}_K\}$.

The observed distribution of the date set $\mathcal{D}$ is represented by a Gaussian mixture model which is a simple linear superposition of the K single Gaussian components [113, 114].

Thus, the Gaussian mixture distribution is written in the form

$$p(\mathbf{x}_n) = \sum_{k=1}^{K} \pi_k \mathcal{N}\left(\mathbf{x}_n | \boldsymbol{\mu}_k, \boldsymbol{\Sigma}_k\right) \tag{5.2}$$

where π_k, the mixing coefficient, represents the contribution of the k^{th} bundle to the overall observed distribution. The values of π_k satisfy $\pi_k \in \{0, 1\}$ and $\sum_{k=1}^{K} \pi_k = 1$. Similarly, we denote the mixing coefficients of the K target fiber bundles as a K-dimensional variable $\boldsymbol{\pi} \equiv \{\pi_1, \ldots, \pi_K\}$.

For the purpose of fiber clustering, we now introduce a K-dimensional binary indicator variable $\mathbf{c} = [c_1, \ldots, c_K]$ to denote the latent variable, i.e., the class label of fiber tracts. $\mathbf{c}$ has a 1-of-K representation in which a particular element c_k equals 1 and all other elements equal to 0. Therefore, $c_k \in \{0, 1\}$ and $\sum_{k=1}^{K} c_k = 1$. Every fiber tract in the clustering has a corresponding latent variable c_k. If a fiber track is assigned to cluster k then its $c_k = 1$.

With the help of the latent variable $\mathbf{c}$ we are now able to estimate the joint distribution $p\left(\mathbf{x}, \mathbf{c}\right)$ by means of the marginal and conditional distribution $p\left(\mathbf{c}\right)$ and $p\left(\mathbf{x}|\mathbf{c}\right)$. The marginal distribution

$$p(c_k) \equiv p(c_k = 1) = \pi_k \tag{5.3}$$

Note that we denote the priori probability of $p(c_k = 1)$ as π_k, i.e., the mixture proportion of each single Gaussian component. Thus

$$p(\mathbf{c}) = \prod_{k=1}^{K} \pi_k^{c_k} \tag{5.4}$$

The marginal distribution follows a Gaussian and is formed as

$$p(\mathbf{x}_n | c_k) \equiv p(\mathbf{x}_n | c_k = 1) = \mathcal{N}(\mathbf{x}_n | \boldsymbol{\mu}_k, \boldsymbol{\Sigma}_k) \tag{5.5}$$

and

$$p(\mathbf{x}_n | \mathbf{c}) = \prod_{k=1}^{K} \mathcal{N}(\mathbf{x}_n | \boldsymbol{\mu}_k, \boldsymbol{\Sigma}_k)^{c_k} \tag{5.6}$$

Then we get the joint distribution from Equations 5.4 and 5.6

$$p\left(\mathbf{x}_n, \mathbf{c}\right) = p(\mathbf{c}) p(\mathbf{x}_n | \mathbf{c}) \tag{5.7}$$

Summing over all the target classes gives the marginal distribution of $\mathbf{x}_n$

$$p(\mathbf{x}_n) = \sum_{\mathbf{c}} p\left(\mathbf{x}_n, \mathbf{c}\right) = \sum_{\mathbf{c}} p\left(\mathbf{c}\right) p(\mathbf{x}_n|\mathbf{c}) = \sum_{k=1}^{K} \pi_k \mathcal{N}\left(\mathbf{x}_n|\boldsymbol{\mu}_k, \boldsymbol{\Sigma}_k\right) \tag{5.8}$$

It shows that the marginal distribution $p(\mathbf{x}_n)$ is also a Gaussian mixture and its formulation is equivalent to Equation 5.2. But it explicitly contains the latent variable, i.e., the class labels $\mathbf{c}$ which are of our interests in the context of fiber clustering. This desirable characteristic makes it possible for us to estimate the joint distribution $p(\mathbf{x}_n, \mathbf{c})$ instead of the marginal distribution $p(\mathbf{x}_n)$. Thus it leads us further to calculate the following Bayesian posterior probability p_{nk} and finally to estimate the class labels of fiber tracts.

Based on Equations 5.3, 5.5, and 5.8, the posterior probability of c_k given the fiber tract $\mathbf{x}_n$ is available by using the Bayesian theorem

$$\begin{aligned} p_{nk} = p(c_k|\mathbf{x}_n) &= \frac{p(c_k)p(\mathbf{x}_n|c_k)}{p(\mathbf{x}_n)} \\ &= \frac{\pi_k \mathcal{N}(\mathbf{x}_n|\boldsymbol{\mu}_k, \boldsymbol{\Sigma}_k)}{\sum_{i=1}^{K} \pi_i \mathcal{N}\left(\mathbf{x}_n|\boldsymbol{\mu}_i, \boldsymbol{\Sigma}_i\right)} \end{aligned} \tag{5.9}$$

For handling outliers, We set up one threshold for posterior probability p_{nk}. That is, if p_{nk} is less than a certain value, x_n will be labeled as outlier.

5.2.2 Feature Selection

To reduce the heavy computing cost and the noise impact on the clustering accuracy, both of which are inherent to the traditional step point comparison techniques, we instead select features limited at the fiber tract level. We split the representation of a fiber tract into three separate parts, the shape, length, and spatial position characteristics. Specifically, we model the shape of a fiber tract using Fourier descriptors derived from its shape signatures, i.e., the Euclidean coordinates of the step points. And the spatial position used is a relative position described by the distance from a reference point instead of an absolute distance.

We have first introduced the Fourier descriptor tract model in Chapter 4. In this work, we make two major modifications based on the performance of the clustering algorithm

we develop in this chapter. The first modification is that we use the step points along a white matter tract as our shape signature. Secondly, we do not simply sum over the three components as what is introduced in Eqauition 5.23. Instead, we take each individual component's real part as one single feature. The following describes the details. For the sake of clarity, we briefly repeat the Fourier transform definition here.

Fourier Descriptors

In the streamline tractography techniques, a single fiber tract consists of a sequence of step points in the number of several tens to several hundreds. Assume the i-th step point has the three dimensional coordinates (x_i, y_i, z_i). (x_i, y_i, z_i) are the shifted coordinates according to the mid-sagittal plan of the brain we will show later. We compute the discrete Fourier transform of a fiber tract for each of the components of the three dimensional coordinates (x_i, y_i, z_i) individually [101]

$$\mathcal{F}_l(s) = \frac{1}{L}\sum_{i=0}^{L-1} s_i \exp\left(-\frac{2\pi j}{L} li\right),\ l = 0, 1, \ldots, L-1 \tag{5.10}$$

where L is the number of step points along a fiber tract, s represents x or y or z, s_i is x_i or y_i or z_i at the ith point, $i = 0, 1, \ldots, L-1$, and j is the imaginary unit, i.e., $j = \sqrt{-1}$.

$\mathcal{F}_l(s)$ is a complex describing the magnitude and phase of the input as a function of frequency. In our application, the phase information is not important and thus discarded. We keep only the magnitude information defined as

$$FD_l(s) = |\mathcal{F}_l(s)| = \sqrt{\text{Re}\left(\mathcal{F}_l(s)\right)^2 + \text{Im}\left(\mathcal{F}_l(s)\right)^2} \tag{5.11}$$

where $\text{Re}\left(\mathcal{F}_l(s)\right)$ and $\text{Im}\left(\mathcal{F}_l(s)\right)$ are the real and imaginary parts of $\mathcal{F}_l(s)$ respectively. The coefficient $FD_l(s)$ is called the Fourier shape descriptor of a fiber tract in our context. Sometimes it is referred as the frequency spectrum or spectral density in the signal processing feild. Since the coordinates x_i, y_i, and z_i are all real values, there are only $L/2$ different frequencies in the discrete Fourier transform. If L is an odd number, the number of different frequencies is $(L+1)/2$. In the following discussion, we assume that L is

even for convenience. Therefore, only a half of the Fourier descriptors in Equation 5.10 are needed to describe the shape pattern of a fiber tract.

Fourier descriptors transform the fiber tract shape description from the spatial domain, i.e., the three dimensional Euclidean space, into a frequency domain. This transformation eliminates the difficulty and cost to find the step point-wise correspondence between two randomly organized fiber tracts in the spatial domain at all. The number of coefficients from Fourier transform is usually large, but a small subset of these coefficients is sufficient to capture the general shape features of a fiber tract. Furthermore, it provides us the flexibility to use more or less features in clustering according to the closeness in the shape measurement of fiber tracts. We show in Section 5.3 that this small subset of coefficients together with a few geometric features is adequate to identify one fiber tract from others.

Geometric Features

Besides the above mentioned Fourier descriptors to characterize a fiber's shape pattern, we also employ a few geometric features at the fiber tract level to characterize a fiber tract. They are the length, the shifted coordinates of the centroid or the geometric center of a fiber tract, and the distance between a fiber's centroid and a user defined reference point. We use the shifted coordinates and the distance based on the fact that the human brain is left and right sphere symmetric. The reference point used in this study is the centroid of bounding box of the mid-sagittal corpus callosum. We choose it as the reference point based on two observations. First, our common sense of the brain symmetry means that the left and right brain sphere are symmetric according to the mid-sagittal plan. The second observation is that the size of the bounding box of the corpus callosum on the mid-sagittal plan are similar, though not identical, across populations. And the averaging effect in obtaining the centroid of the bounding box reduces the difference. In fact, other reference points can certainly be employed as long as the difference of the relative distance between a spatial location and the reference point among subjects is small.

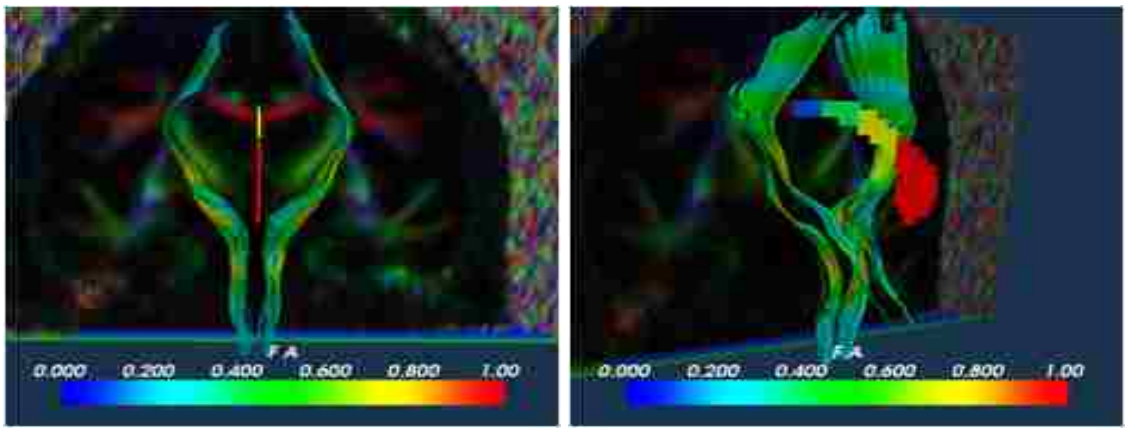

Figure 5.1: Two angle's views of the symmetric property of tract bundles. The mid sagittal corpus callosum plan is covered by a mask. The symmetric fiber bundles are colored by the overlapped FA values at step points along tracts. The bottom color bars indicate correspondences between colors and FA values.

The length is defined as the number of step points along a fiber tract. The centroid of a fiber tract (x_c, y_c, z_c) is the geometric center of the fiber tract which is the average of coordinates of all the step points along a fiber tract

$$x_c = \frac{1}{L}\sum_{i=0}^{L-1} x_i, \quad y_c = \frac{1}{L}\sum_{i=0}^{L-1} y_i, \quad z_c = \frac{1}{L}\sum_{i=0}^{L-1} z_i. \tag{5.12}$$

Here L is the number of step points of a fiber tract.

Due to the symmetry of the brain, we use the shifted coordinates to represent a step point of a fiber tract. Assume that the coordinates of the i^{th} step points is (x_i, y_i, z_i) and the mid sagittal plan is located at x_m, then the shifted coordinates of the i^{th} step point is $(|x_i - x_m|, y_i, z_i)$. In this way, the two symmetric positions in the symmetric left and right half brain spheres have the same positive x coordinates. Figure 5.1 depicts the symmetric property of fiber bundles.

Figures 5.2 and 5.3 demonstrate the calculation of the shifted coordinates. The geometric center of the bounding box of the mid-sagittal corpus callosum plan is shown as a large purple ball in Figures 5.2 and 5.3. The small purple ball in the right subfigure of Figure 5.3 represents the geometric center of the fiber tract shown in the graph. The distance between the geometric center of the reconstructed white matter tract and the geometric center of

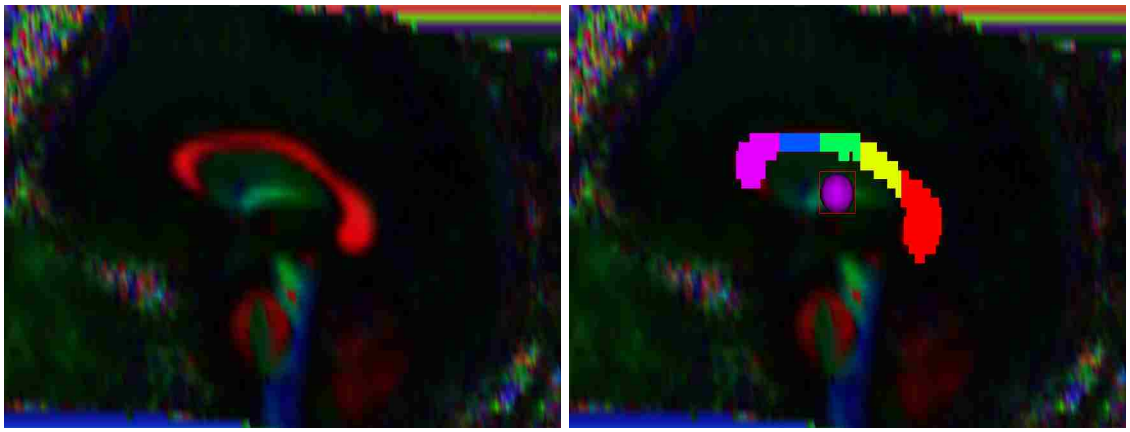

(a) The mid-sagittal corpus callosm plan. (b) The mid-sagittal corpus callosm plan mask.

Figure 5.2: Sagittal view of the mid-sagittal corpus callosum plan and the geometric center of its bounding box. In the right subfigure, the purple ball represents the the geometric center of the bounding box of the mid-sagittal corpus callosum plan. A mask is placed on the mid-sagittal corpus callosum in the right subfigure.

the bounding box of the mid-sagittal corpus callosum plan is depicted by a double arrowed yellow straight line.

Formation of the Features Vector

Combine the above introduced features together, the n^{th} fiber tract ${x_n}^{\text{T}}$ then is depicted by the following $D-$dimensional feature vector

$$\begin{aligned} {x_n}^{\text{T}} = [&FD_1(x), \ldots, FD_{D_x}(x), \\ &FD_1(y), \ldots, FD_{D_y}(y), \\ &FD_1(z), \ldots, FD_{D_z}(z), \\ &L_n, x_{nc}, y_{nc}, z_{nc}] \end{aligned} \tag{5.13}$$

where L_n is the length of this tract, i.e., the number of step points it has. D_x, D_y, and D_z are the numbers of Fourier descriptors of the coordinate x, y, and y respectively. (x_{nc}, y_{nc}, z_{nc}) is the coordinate of the geometric center of the tract. We let $D_x = D_y = D_z$ for simplicity.

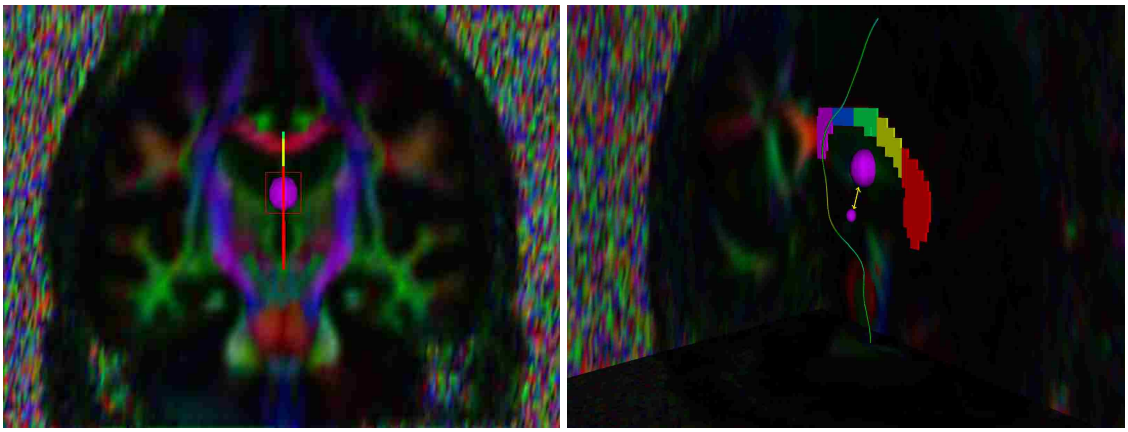

Figure 5.3: Illustration of the distance between two geometric centers. The left subfigure is the coronal view of the mid-sagittal corpus callosum plan mask and the geometric center of its bounding box. The small purple ball in the right subfigure represents the geometric center of the fiber tract shown in the graph. The distance between the geometric center of the reconstructed white matter tract and the geometric center of the bounding box of the mid-sagittal corpus callosum plan is depicted by the double arrowed yellow straight line.

5.2.3 Unsupervised Clustering

In general, parameters, π_k, $\boldsymbol{\mu}_k$ and $\boldsymbol{\Sigma}_k$, in the Gaussian mixture model of Equation 5.2 are unknown. To achieve our goal, we need first to estimate these unknown parameters of the distribution of the target bundles from the data set $\mathcal{D}$, i.e., the N fiber tracts need to be labeled. We can do this by using MLE [113, 114]. From Equation 5.2 the logarithm of the likelihood is

$$\ln p\left(\mathbf{X}\middle|\boldsymbol{\pi},\boldsymbol{\mu},\boldsymbol{\Sigma}\right)=\sum_{n=1}^{N}\ln\left\{\sum_{k=1}^{K}\pi_k\mathcal{N}\left(\mathbf{x}_n\middle|\boldsymbol{\mu}_k,\boldsymbol{\Sigma}_k\right)\right\} \tag{5.14}$$

We denote the parameter set, $\boldsymbol{\pi}$, $\boldsymbol{\mu}$ and $\boldsymbol{\Sigma}$, as $\boldsymbol{\Theta}$ for our convenience. Then the estimated parameter set $\hat{\boldsymbol{\Theta}}$ is

$$\hat{\boldsymbol{\Theta}}=\arg\max_{\Theta}\left\{\ln p\left(\mathbf{X}\middle|\boldsymbol{\Theta}\right)\right\} \tag{5.15}$$

Equation 5.14 shows that the maximum likelihood solution for the unknown parameters does not have a closed analytical form under the mixture model context. We employ the well-known framework which is called the EM algorithm to approximate the maximum likelihood solutions [115, 116]. After appropriate initializations, the EM algorithm finds the optimal solution by iteratively performing the expectation (E-step) and maximiza-

tion (M-step) until it reaches convergence. We summarize it as below

1). E-step. Evaluate the the posterior probability of c_k given the fiber tract $\mathbf{x}_n$, i.e., p_{nk}. p_{nk} depicts the probability, or the level of the certainty, that fiber tract $\mathbf{x}_n$ belongs to the k-th target bundle. Suppose we are at the i-th iteration and the current parameter set is $\hat{\Theta}^{\text{i-1}}$, then we have

$$p_{nk}^{i} = \frac{\pi_k^{i-1}\mathcal{N}\left(\mathbf{x}_n \middle| \boldsymbol{\mu}_k^{i-1}, \boldsymbol{\Sigma}_{\boldsymbol{k}}^{\boldsymbol{i-1}}\right)}{\sum_{j=1}^{K} \pi_j^{i-1}\mathcal{N}\left(\mathbf{x}_n \middle| \boldsymbol{\mu}_j^{i-1}, \boldsymbol{\Sigma}_{\boldsymbol{j}}^{\boldsymbol{i-1}}\right)} \tag{5.16}$$

2). M-step. Update the parameter set $\hat{\Theta}^{\text{i}}$ using the current posterior probability p_{nk}^{i} obtained at the E-step, i.e.,

$$N_k^i = \sum_{n=1}^{N} p_{nk}^i \tag{5.17}$$

$$\boldsymbol{\mu}_k^i = \frac{1}{N_k^i}\sum_{n=1}^{N} p_{nk}^i \boldsymbol{x}_n \tag{5.18}$$

$$\boldsymbol{\Sigma}_k^i = \frac{1}{N_k^i}\sum_{n=1}^{N} p_{nk}^i \left(\boldsymbol{x}_n - \boldsymbol{\mu}_k^i\right)\left(\boldsymbol{x}_n - \boldsymbol{\mu}_k^i\right)^{\text{T}} \tag{5.19}$$

$$\pi_k^i = \frac{N_k^i}{N} \tag{5.20}$$

Once the EM algorithm reaches its convergence, the estimated parameters $\pi_k, \boldsymbol{\mu}_k, \boldsymbol{\Sigma}_k$ in current feature set become available.

In a complicated situation, the above EM procedure with a fixed small set of features does not guarantee that it will generate the desirable results for all clusters. In our study, it happens when some of the fiber bundles are very similar in both the shape and positional measures. We overcome this difficulty by employing more Fourier descriptors in clustering. To automate this procedure, we simply add one out layer loop outside the EM iteration. In the out layer loop, we increase the number of Fourier descriptors by one at each iteration until a predefined threshold is reached. The structure of the algorithm is depicted in Algorithm 1. In Algorithm 1, e is the predefined threshold which measures the differences

of all the three unknowns between two iterations. That is, we check if the stop condition

$$||\boldsymbol{\mu}_{knew} - \boldsymbol{\mu}_{kold}|| + |\pi_{knew} - \pi_{kold}| + |\mathrm{trace}(\boldsymbol{\Sigma}_{\mathrm{knew}}) - \mathrm{trace}(\boldsymbol{\Sigma}_{\mathrm{kold}})| < \mathrm{e} \tag{5.21}$$

holds at each iteration.

The cluster label $\hat{k}$ according to the largest p_{nk} is assigned to the n^{th} fiber tract if p_{nk} is greater than a user defined threshold for handling outliers. That is

$$\hat{k} = \arg\max_{k} \{p_{nk}\}, k = 1, \ldots, K \tag{5.22}$$

If p_{nk} is less than the outlier threshold, a label of outlier is assigned to this tract.

5.2.4 Supervised Clustering

In the case that parameters, π_k, $\boldsymbol{\mu}_k$ and $\boldsymbol{\Sigma}_k$, in the Gaussian mixture model of Equation 5.2 are known, we can directly calculate the *a posterior* Bayesian probabilities based on Equation 5.9 and thus omit the EM procedure. The algorithm is a simplified version of the Algorithm 1 and is illustrated in the Algorithm 2. In Algorithm 2, definitions of parameters and the stop criterion are the same as that in Algorithm 1 and FD refers to Fourier descriptor.

5.3 Experiments and Results

Fourier descriptors and some spatial features are used to form the feature vector. For convenience, we use following conventions in our discussion:

FD - Fourier descriptor;

FD_x - Fourier descriptor of the x component of the coordinate (x, y, z);

FD_y - Fourier descriptor of the y component of the coordinate (x, y, z);

FD_y - Fourier descriptor of the z component of the coordinate (x, y, z);

L - Tract length which is the number of step points on it;

(cx, cy, cz) - Coordinates of the geometric center of a tract;

$cdist$ - The distance between the geometric center of a tract and the geometric center of the

Algorithm 1 Algorithm with additive Fourier descriptors and EM

Ensure: $N_{old} = N_{new} = \#$ of fibers;
$K_{old} = K_{new} = \#$ of target bundles;
$D_{max} =$ maximum # of Fourier descriptors;
$D = \#$ of Fourier descriptors; $e =$ Predefined stop criterion; $\boldsymbol{\mu}_{old}$; $\boldsymbol{\Sigma}_{old}$; $\boldsymbol{\pi}_{old}$

while $K_{old} > 0 \vee D < D_{max}$ **do**
  $n = 0$
  while $n < N_{old}$ **do**
    construct the feature vector ${x_n}^{\mathrm{T}}$
    $n \leftarrow n + 1$
  end while
  initialize the EM algorithm with $\boldsymbol{\mu}_{old}$, $\boldsymbol{\Sigma}_{old}$, and $\boldsymbol{\pi}_{old}$
  run the EM with N_{old} and K_{old} and obtain $\boldsymbol{\mu}_{new}$, $\boldsymbol{\Sigma}_{new}$, and $\boldsymbol{\pi}_{new}$
  $k = 0$
  while $k < K_{old}$ **do**
    $N_k = 0$
    $k \leftarrow k + 1$
  end while
  $n = 0$
  while $n < N_{old}$ **do**
    $k = 0$
    while $k < K_{old}$ **do**
      if x_n is labeled as k **then**
        $N_k \leftarrow N_k + 1$
      end if
      $k \leftarrow k + 1$
    end while
    $n \leftarrow n + 1$
  end while
  $k = 0$
  while $k < K_{old}$ **do**
    if $||\boldsymbol{\mu}_{knew} - \boldsymbol{\mu}_{kold}|| + |\pi_{knew} - \pi_{kold}| + |\mathrm{trace}(\boldsymbol{\Sigma}_{\mathrm{knew}}) - \mathrm{trace}(\boldsymbol{\Sigma}_{\mathrm{kold}})| < \mathrm{e}$ **then**
      $K_{new} \leftarrow K_{old} - 1$
      $N_{new} \leftarrow N_{old} - N_k$
      $k \leftarrow k + 1$
    end if
  end while
  $K_{old} \leftarrow K_{new}$
  $N_{old} \leftarrow N_{new}$
  $k = 0$
  while $k < K_{old}$ **do**
    $\pi_{kold} = \pi_{knew}$
    $\boldsymbol{\mu}_{kold} = \boldsymbol{\mu}_{knew}$
    $\boldsymbol{\Sigma}_{kold} = \boldsymbol{\Sigma}_{knew}$
    $k \leftarrow k + 1$
  end while
end while

Algorithm 2 Clustering algorithm with the atlas

Ensure: $N_{old} = N_{new} = \#$ of tracts; $K_{old} = K_{new} = \#$ of target bundles; $D_{max} =$ max # of FDs; $D = \#$ of FDs; $e =$ Stop criterion; $\boldsymbol{\mu}_{old}; \boldsymbol{\Sigma}_{old}; \boldsymbol{\pi}_{old}$

while $K_{old} > 0 \vee D < D_{max}$ **do**
  $n = 0$
  while $n < N_{old}$ **do**
    construct the feature vector ${x_n}^{\mathrm{T}}$
    $n \leftarrow n + 1$
  end while
  $n = 0$
  while $n < N_{old}$ **do**
    calculate p_{nk} using Equation 5.9 with $\boldsymbol{\mu}_{old}$, $\boldsymbol{\Sigma}_{old}$, and $\boldsymbol{\pi}_{old}$
    label this fiber tract according to its maximum p_{nk}
    $n \leftarrow n + 1$
  end while
  calculate $\boldsymbol{\mu}_{new}$, $\boldsymbol{\Sigma}_{new}$, and $\boldsymbol{\pi}_{new}$ from the labeled fiber tracts
  $k = 0$
  while $k < K_{old}$ **do**
    $N_k = 0$
    $k \leftarrow k + 1$
  end while
  $n = 0$
  while $n < N_{old}$ **do**
    $k = 0$
    while $k < K_{old}$ **do**
      if x_n is labeled as k **then**
        $N_k \leftarrow N_k + 1$
      end if
      $k \leftarrow k + 1$
    end while
    $n \leftarrow n + 1$
  end while
  $k = 0$
  while $k < K_{old}$ **do**
    if $||\boldsymbol{\mu}_{knew} - \boldsymbol{\mu}_{kold}|| + |\pi_{knew} - \pi_{kold}| + |\mathrm{trace}(\boldsymbol{\Sigma}_{\mathrm{knew}}) - \mathrm{trace}(\boldsymbol{\Sigma}_{\mathrm{kold}})| < \mathrm{e}$ **then**
      $K_{new} \leftarrow K_{old} - 1$
      $N_{new} \leftarrow N_{old} - N_k$
      $k \leftarrow k + 1$
    end if
  end while
  $K_{old} \leftarrow K_{new}$
  $N_{old} \leftarrow N_{new}$
  $k = 0$
  while $k < K_{old}$ **do**
    $\pi_{kold} = \pi_{knew}$
    $\boldsymbol{\mu}_{kold} = \boldsymbol{\mu}_{knew}$
    $\boldsymbol{\Sigma}_{kold} = \boldsymbol{\Sigma}_{knew}$
    $k \leftarrow k + 1$
  end while
end while

mid sagittal corpus callosum plan;

e - The predefined stop criterion of EM algorithm;

po - The user defined outlier threshold for labeling with a default value 0.5;

K - Number of tract bundles;

N - Number of reconstructed white matter tracts;

D - The dimension of the feature vector;

D_{FD_x} - The number of FD_x;

D_{FD_y} - The number of FD_y;

D_{FD_z} - The number of FD_z;

D_{FD} - The total number of Fourier descriptors, i.e. the summation of D_{FD_x}, D_{FD_y}, and D_{FD_z};

In default, FD_x starts from its first term. Priori probabilities $\boldsymbol{\pi}$ of all K target bundles are set as $1/K$.

5.3.1 DTI Data

The DTI data used in this study are from health controls which are described in sections 1.3.2 and 2.4.1.

5.3.2 Without Outliers

First, we test the performance of our technique with reconstructed white matter tracts including no outliers. We would like to find if the algorithm can correctly segment these well formed tract bundles.

Before the clustering, we manually reconstruct seven separated tract bundles. All these bundles have been carefully trimmed and validated. There are totally $2,498$ tracts included in the seven bundles. After visual checking, we found no outlier. The seven bundles are shown in Subfigure 5.4(b). We then mix the seven bundles together and form the unlabeled inputs for the clustering algorithm. The mixed tracts are illustrated in Subfigure5.4(a). The experimental results show that the $2,498$ tracts are all correctly labeled into the seven

bundles and no tract is labeled as outlier. Here, $D = 20$, $D_{FD_x} = 5$, $D_{FD_y} = 5$, and $D_{FD_z} = 5$. The 5 spatial features include L, cx, cy, cz, and $cdist$. $e = 1.00e - 006$ and $po = 0.50$. The number of EM iterations is 3.

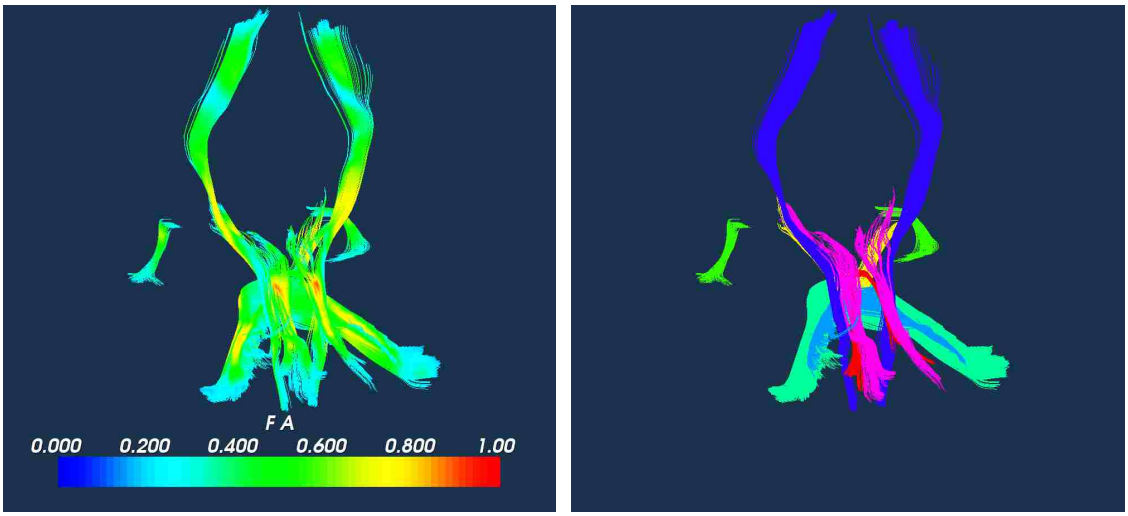

(a) Unclassified 2498 tracts (b) Classified seven tract bundles

Figure 5.4: Illustration of the clustering results with well defined input tracts. Subfiger (a) shows the input reconstructed white matter tracts. Subfiger (b) demonstrates the clustering results which are seven separated tract bundles colored differently.

5.3.3 With Outliers

Figure 5.5 demonstrates the clustering result on totally $23,770$ reconstructed white matter tracts. Among the $23,770$ tracts, $14,550$ are grouped into 18 target bundles and $9,220$ are labeled as outliers. Here, $D = 50$, $D_{FD_x} = 15$, $D_{FD_y} = 15$, and $D_{FD_z} = 15$. The 5 spatial features include L, cx, cy, cz, and $cdist$. $e = 1.00e - 012$ and $po = 0.50$. The number of EM iterations is 57. With visual validation, the clustering result is quit reasonable.

5.4 Discussion

5.4.1 Evaluation of the Proposed Fourier Descriptor Formation

We have previously mentioned the modification of Fourier descriptor representation for reconstructed white matter tracts in 5.2.2. Take the three dimensional coordinates (x, y, z) of tract step points as shape signatures, we have to apply the Fourier transform on each of

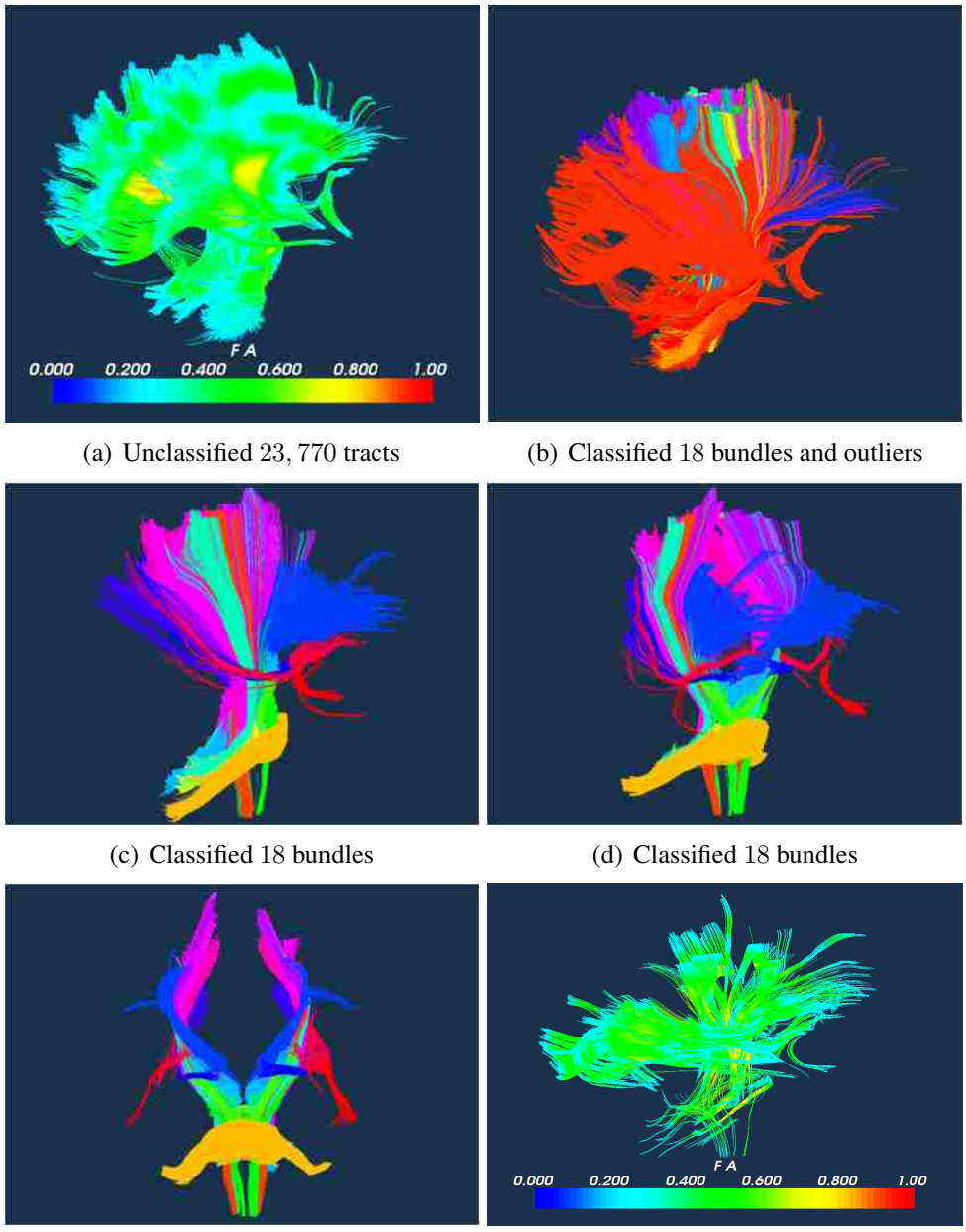

(a) Unclassified $23,770$ tracts

(b) Classified 18 bundles and outliers

(c) Classified 18 bundles

(d) Classified 18 bundles

(e) Classified 18 bundles

(f) Outliers after clustering

Figure 5.5: Illustration of the clustering result on totally $23,770$ reconstructed white matter tracts. Subfigure (a) shows the tracts before clustering. Subfigure (b) gives the clustered tracts including 18 tract bundles and $9,220$ outliers. Subfigures (c), (d), and (e) demonstrates the 18 tract bundles viewed in three different angles. Subfigure (f) illustrates the $9,220$ tracts labeled as outliers.

the components x, y, and z respectively. Then three sets of Fourier descriptors $FD_x(k)$, $FD_y(k)$ and $FD_z(k)$ are obtained. To get the one dimensional Fourier descriptor, the traditional approach is to combine these three sets of descriptors into one set of descriptors. For example [101]

$$|FD(k)| = \sqrt{|FD_x(k)|^2 + |FD_y(k)|^2 + |FD_z(k)|^2}, \tag{5.23}$$

This combination does work well in the context of our proposed method. We find it reduces much differentiation power when a large number of outliers are included in the clustering input. In this work, we have developed a new scheme which is described in Subsection 5.2.2. By comparing these two approaches on the same set of reconstructed white matter tracts, we conclude that our scheme performs much better in the context of this work.

In the following, we refer to the traditional approach and our developed scheme as combined FD and uncombined FD respectively.

In this comparison, $N = 23,770$, $K = 18$, $e = 1.00e-012$ and $po = 0.80$. No any geometric feature is used. For the combined FD method, $D = D_{FD} = 27$. For the uncombined FD approach, $D_{FD_x} = 9$, $D_{FD_y} = 9$, and $D_{FD_z} = 9$. So $D = D_{FD} = D_{FD_x} + D_{FD_y} + D_{FD_z} = 27$ and the two kinds of feature vectors have the same dimension.

After clustering, 21,608 tracts are grouped into the 18 target bundles and 2,162 tracts are labeled as outliers with the combined FD method. With the uncombined FD method, these two numbers are 17,606 and 6,164 separately.

Figure 5.6 gives the visual comparisons of 3 tract bundles among the 18 target bundles after clustering. After visual check, we find that our developed uncombined approach performs better than the traditional combined method on all the 18 bundles.

With a fixed arc length as we fit the tract parameter, our presented scheme can deal with shorter tracts than that in the traditional method. Since we need fewer step points along the tract to achieve the same dimension of feature vectors. In the above comparison, our approach needs only 9 step points to make $D = 27$. On the other hand, the traditional

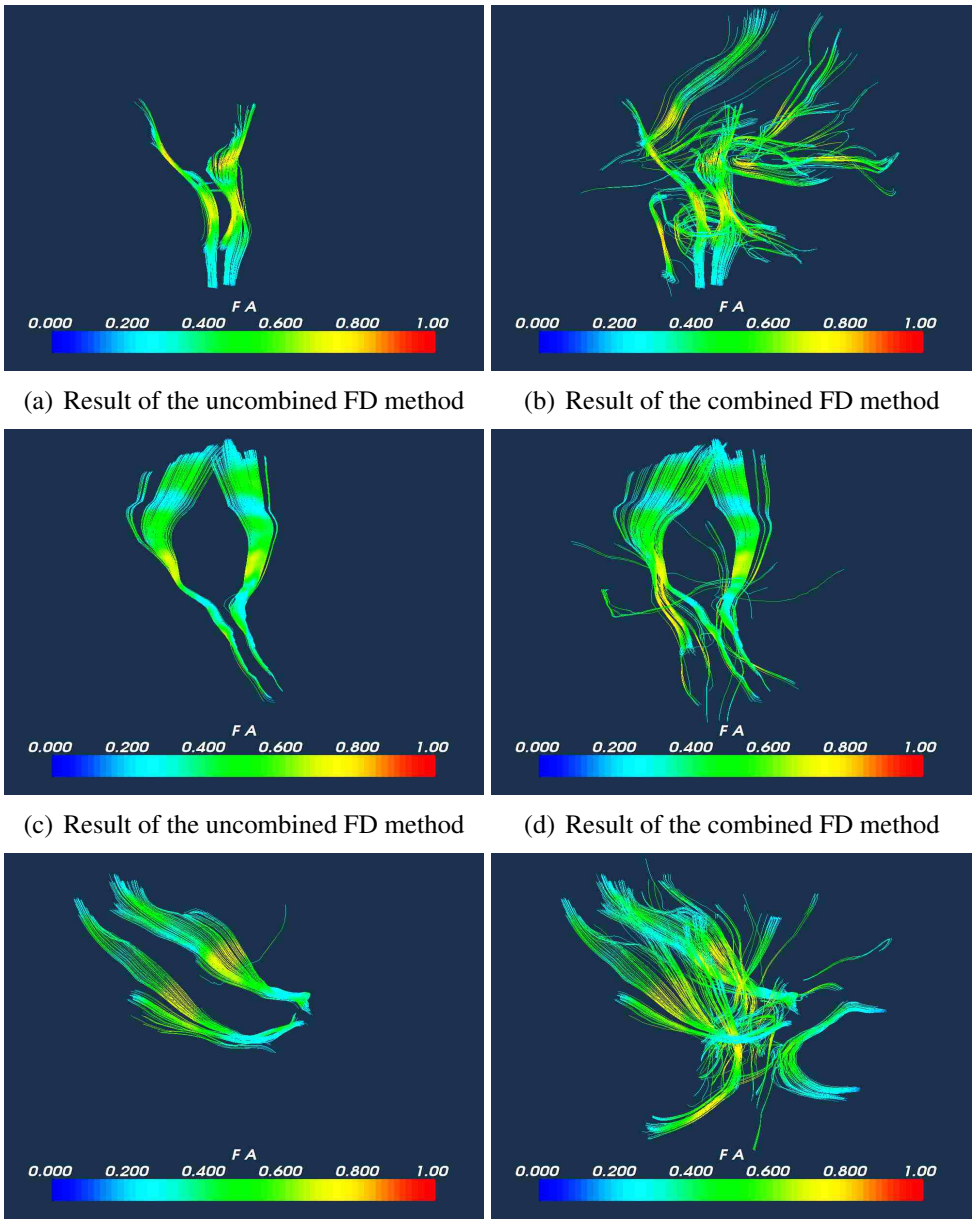

(a) Result of the uncombined FD method

(b) Result of the combined FD method

(c) Result of the uncombined FD method

(d) Result of the combined FD method

(e) Result of the uncombined FD method

(f) Result of the combined FD method

Figure 5.6: Visual comparisons of the performance of combined and uncombined FD methods in reconstructed white matter tract clustering. Subfigures (a), (c), and (e) are the clustering results with the uncombined FD approach. Subfigures (b), (d), and (f) are the clustering results of the same tract bundles using the combined FD method.

approach needs 27 step points. The fitting arc length matters respect to noise resistance and computational efficiency. Shorter fitting arc length can worsen the noise resistance and computational efficiency of an approach.

5.4.2 Comparison with K-means

As a robust and popular clustering algorithm, K-means is widely used in a variety of areas [113, 114]. Here, we compare the clustering result of our presented method with that of the K-means algorithm on a same set of reconstructed white matter tracts.

In this experiment, $N = 4,733$, $K = 5$, $e = 1.00e-012$ and $po = 0.50$. $D_{FD_x} = 5$, $D_{FD_y} = 5$, and $D_{FD_z} = 5$. The 5 spatial features include L, cx, cy, cz, and $cdist$. So $D_{FD} = D_{FD_x} + D_{FD_y} + D_{FD_z} = 15$ and $D = 20$. The iteration number of our algorithm is 5.

Since no any covariance matrix information can be adopted into the K-means algorithm, we provide only the same set of mean vectors as that of our proposed method for the initialization of K-means. The cluster number for K-means is set as 5.

The experimental results show that both of the two algorithms take a very short time to finish the clustering. And all the 4,733 tracts are labeled into the target 5 bundles. There is no outlier is labeled. The major difference between them appears in the accuracy of some result tract bundles. Figure 5.7 illustrates the comparisons of the two clustering algorithms.

5.4.3 Impacts of the Number of Fourier Descriptors

Figure 5.8 shows the effect of the number of the Fourier descriptors included in the feature vector on clustering.

Subfigure 5.8(a) show 1,216 tracts are grouped into one single bundle after the clustering on 23,770 tracts with 9 Fourier descriptors. In detail, the parameters for the clustering are $N = 23,770$, $K = 18$, $e = 1.00e-09$ and $po = 0.50$. $D_{FD_x} = 9$, $D_{FD_y} = 9$, and $D_{FD_z} = 9$. The 5 spatial features include L, cx, cy, cz, and $cdist$. So $D_{FD} = D_{FD_x} + D_{FD_y} + D_{FD_z} = 27$ and $D = 32$.

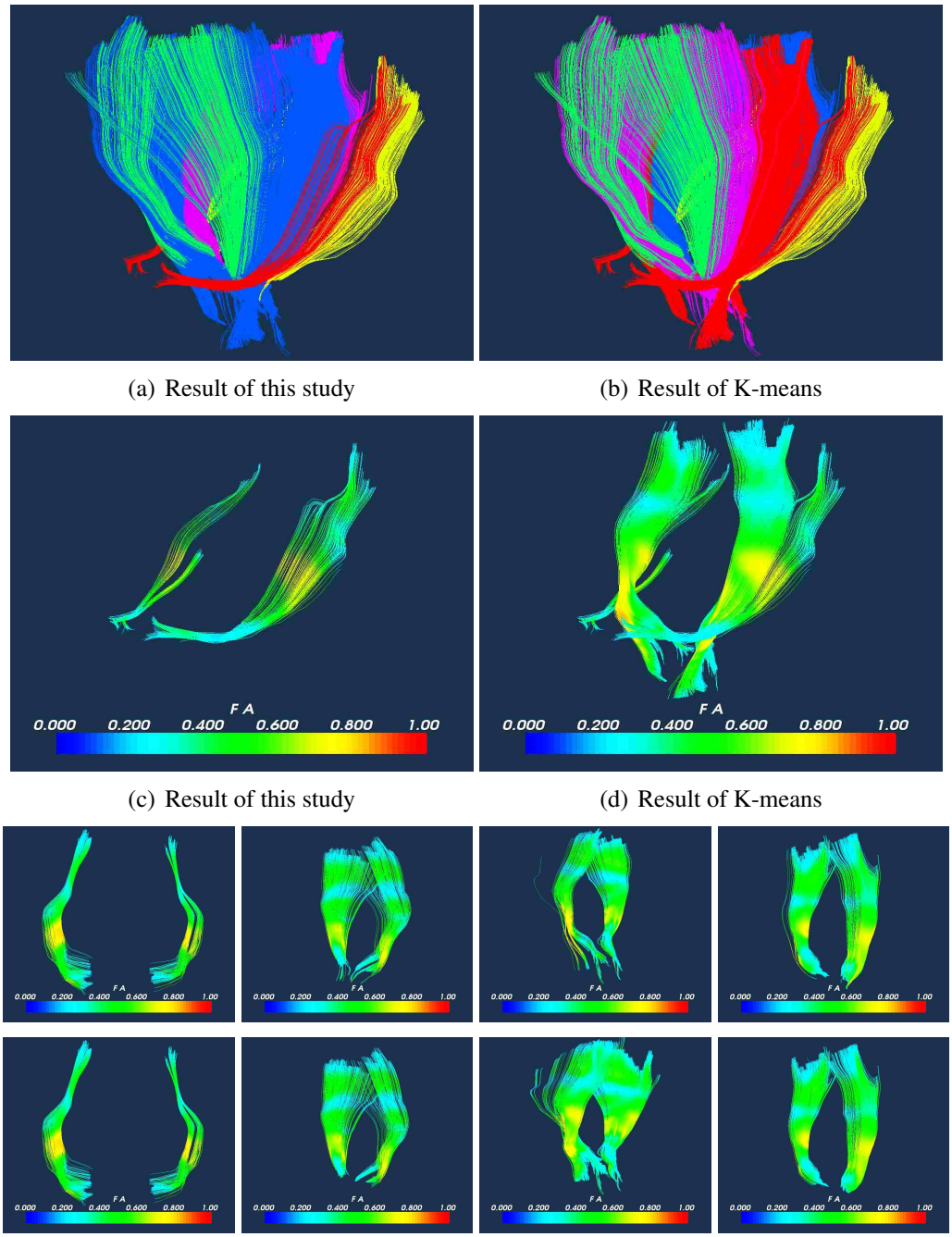

(a) Result of this study (b) Result of K-means

(c) Result of this study (d) Result of K-means

Figure 5.7: Comparisons with the K-means clustering algorithm on a same set of reconstructed white matter. Subfigures (a) and (b) are all the clustered tract bundles by the proposed method and K-means respectively. Subfigures (c) and (c) show the specific tract bundle which has the biggest difference between these two algorithm. The four subfigures in the second last row are the clustering results using K-means. The bottom row are the corresponding results of the proposed method.

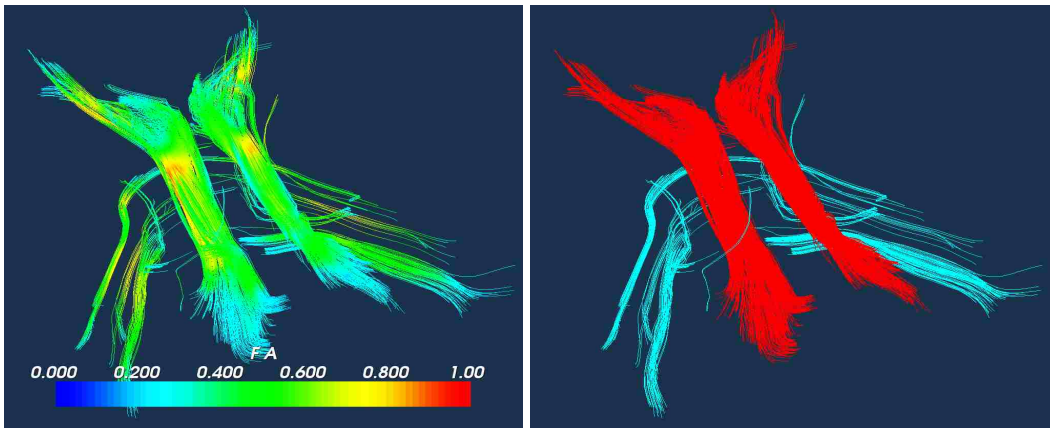

(a) Result with less Fourier descriptors (b) Result with more Fourier descriptors

Figure 5.8: Illustration of the impact of the number of Fourier descriptors on tract clustering. Subfigure (a) demonstrates the clustering result including 1216 tracts which are segmented into one single bundle with 9 Fourier descriptors. Subfigure (b) is the separated tracts after using 12 Fourier descriptors. The red color 983 tracts are labeled into one tract bundle. The rest 233 tracts in another color are labeled as outliers

We then further cluster these 1,216 tracts using the same set of parameters except that $D_{FD_x} = 12$, $D_{FD_y} = 12$, and $D_{FD_z} = 12$. This makes $D_{FD} = D_{FD_x} + D_{FD_y} + D_{FD_z} = 36$ and $D = 41$.

Subfigure 5.8(b) demonstrates that after the second clustering process, outliers are identified successfully. This experiment is in the agreement with our intuition such that in a certain limit, more features are supposed to have more differentiating capability.

This example also indicates that the proposed method has the flexibility to perform hierarchical clustering in necessary.

5.4.4 Sensitivity of π Values

We have afore mentioned that values of priori probabilities $\boldsymbol{\pi}$ of all K target bundles are set as $1/K$ in default. An alternative is to set each single bundle's π value differently based on our *a priori* knowledge. For example, suppose N_k tracts among the totally N tracts belong to a single tract bundle, we may set its $\pi = N_k/N$. But our experiments show that $\boldsymbol{\pi}$ values are not sensitive to the the final clustering result. The major difference appears in the aspect of time cost.

Figure 5.9 graphically depicts the time cost difference. The details of this experiment is $N = 23,770$, $K = 18$, $po = 0.50$, and $e = 1.00e - 09$. The geometric feature used are L, cx, cy, cz, and $cdist$. All the above parameters are fixed for all tests. The only variant parameter is the number Fourier descriptors which is increased by 1 each time. This makes the dimension of the feature vector to increase by 1 accordingly.

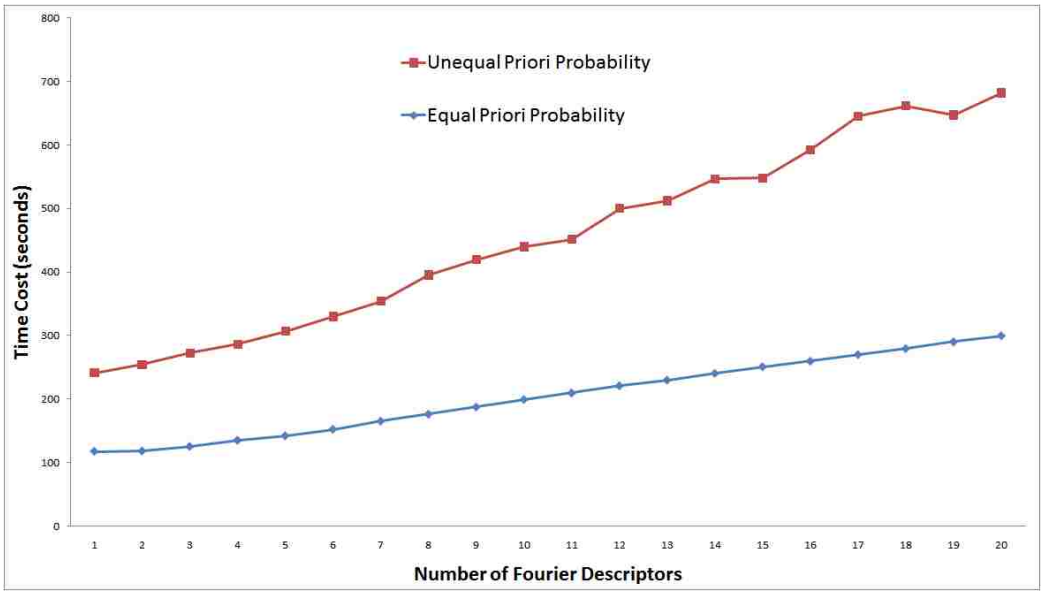

(a)

Figure 5.9: Graphical illustration of the time cost with different setting of $\boldsymbol{\pi}$ values. The graph indicates that the time cost of unequal values of $\boldsymbol{\pi}$ is higher than that of equal values of $\boldsymbol{\pi}$.

5.4.5 Initialization of the EM Algorithm

The initialization of EM seems somewhat arbitrary. But in fact it requires a special attention, since the solution of the algorithm and the time it takes are highly dependent upon its starting points. Suggestions to handle the EM initialization include the approach to run the K-means algorithm first on the data set in order to find a suitable initialization [114, 113]. This becomes even critical under the context of clustering a large amount of fiber tracts as well as handling a large number of outliers. As we have mentioned, outliers in our context include suspicious fiber tracts obtained due to the inaccuracy of the tractography algorithms

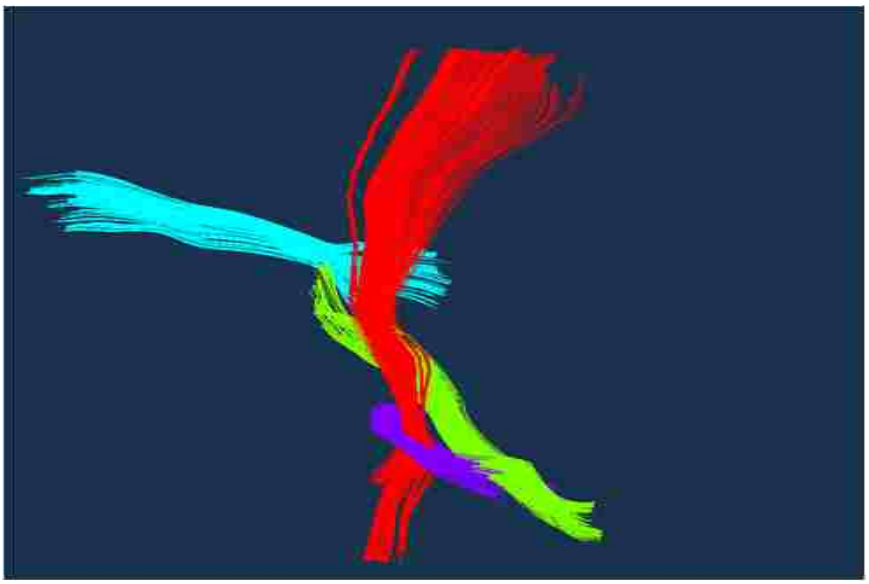

Figure 5.10: Illustration of some initial target fiber bundles used to initialize the EM algorithm.

and fiber tracts which cannot be labeled into any of the target classes. In this work, we first manually track a small number of fiber tracts for each target fiber bundle and then calculate the $\hat{\boldsymbol{\mu}}_k$ and $\hat{\boldsymbol{\Sigma}}_k$. These estimated $\hat{\boldsymbol{\mu}}_k$ and $\hat{\boldsymbol{\Sigma}}_k$ are used to initialize the EM algorithm. Manually tracking a small number of tracts for each bundle is relatively easy and accurate. Since we need only put a small region of interest (ROI) at the center area of a target fiber bundle. Furthermore, we can take the advantage of the symmetry of the left and right brain half spheres. That is, for the fiber bundles appear in both of the left and right half brains, e.g., the cortical spinal tracts, both of their shapes and geometrical positions are symmetric. Thus we only need to track part of the left or right bundles.

Figure 5.10 illustrates some of the initial target bundles we use.

It is worth mentioning that the results discovered by the EM algorithm may be inconsistent among multiple runs if the initializations are different enough. This is because there are generally multiple local maxima of the log likelihood function, and it is not guaranteed for the EM algorithm to reach the global maximum.

Another consequence the inappropriate initialization may incur is the presence of singularities in the Gaussian mixture model context with the maximum likelihood approach.

If the determinant $|\mathbf{\Sigma}_k|$ of the covariance matrix $\mathbf{\Sigma}_k$ of one or more of the Gaussian component becomes close to zero, then its according probability density $\mathcal{N}$ in Equation 5.1 goes to infinity and so does the log likelihood function in Equation 5.14. To reduce the singularity effect on the convergence, we treat the EM as having converged if some parameters instead of the likelihood function fall below some threshold. The parameters we used include the Frobenius norm of $\mathbf{\Sigma}_k$, the maximum eigenvalue of $\mathbf{\Sigma}_k$, and the norm of the mean vector $\boldsymbol{\mu}_k$.

subsectionComputation Complexity and Errors The computation complexity is $O(NDˆ2)$, where N and D are the number of fiber tracts under clustering and the dimension of features. The computation space cost can be accommodated by performing the clustering on a part set of the fiber tracts once a time. The errors are mainly the model error plus the Bayesian error.

5.5 Conclusion

To summarize, we have presented a new clustering framework that aims to facilitate the single subject or group quantitative analysis of the reconstructed white matter tract bundles in DTI data based on certain *a priori* anatomical knowledge. Strategies have developed to handle different situations. The heavy computing burden is largely reduced by eliminating both of the requirements to establish the point-wise correspondence between trajectory pairs and to perform the calculation at the level of the step points along white matter tracts. We achieve this goal by introducing the white matter tract representation in the format of a number of Fourier shape descriptors and geometric features. This representation provides the framework and the theoretical ground to reduce the noise effect inherent to the DTI data and the desired differentiating ability. In the framework, the distribution of fiber tracts is described by a multivariate Gaussian mixture model. This statistical model makes it feasible to exploit the fiber bundle's *a priori* knowledge in the format of the mean and covariance of fiber bundles. Anatomically meaningless white matter tracts are thus mostly avoided.

In the case that we have little *a priori* knowledge, we use the expectation-maximization algorithm to perform the maximum likelihood estimation to label white matter tracts. On the other hand, if a set of white matter tract bundle atlas are given, we can directly label each trajectory by finding its maximum of the *a posterior* Bayesian probabilities among all the target classes. The method has the flexibility to conduct the grouping on a portion or all of the fiber tract set one time to accommodate different situations. In both cases, outliers are handled by easily setting a posterior probability threshold. Real DTI data have been employed to evaluate the method. The experimental results show that the proposed technique is relatively effective and may offer an alternative for existing white matter fiber clustering methods.

6 Evaluation of the Nonnegative Matrix Factorization Technique in White Matter Tract Segmentation

6.1 Outline

In this chapter, we first briefly go over the background and the fundamentals of Nonnegative Matrix Factorization (NMF). Then we present methods to tailor and apply this new classification technique which is widely used in the context of document clustering into the area of white matter tract segmentation. Details about how to construct the nonnegative feature matrix based white matter tract characterizations are described. The performance of NMF clustering technique is evaluated by real DTI data. In the end, the advantages and limitations of NMF in white matter tract segmentation are discussed.

6.2 Introduction

The most popular tractography techniques construct white matter fiber tracts as streamlines [27, 39]. A group of fiber tracts form a white matter fiber bundle that interconnects gray matter regions. Due to the spatial resolution of the currently available DTI datasets, the reconstructed fiber tract streamlines do not correspond to individual axons. Thus, individual streamlines are of no anatomical significance, unless they form a bundle that connects gray matter regions. Clustering reconstructed fiber tract streamlines into meaningful bundles has been an important step in DTI-based white matter fiber analysis.

Over the past few years, a number of white matter tract segmentation schemes have been published. These existing methods have their advantages and disadvantages and generate different clustering results of fiber tracts. The challenge that we face is to model a fiber tract with a representation method to separate fiber tracts belonging to distinct bundles while grouping tracts of the same bundle.

The main purpose of this work is evaluate a computationally efficient and intuitive post processing technique for clustering DTI tractography reconstructed white matter fiber tracts. Especially, we assess approaches to quantify a white matter tract's characterization

and perform segmentation using NMF.

NMF has been widely used in many applications, including document clustering context. It has been shown that NMF surpasses singular value decomposition (SVD) and the eigenvector based clustering methods in the sense that NMF produces both reliable and accurate document clustering results [117].

In this work, we employ Fourier descriptors to provide quantitative and individual representation and normalization of white matter fiber tracts. We then tailor and apply the NMF technique into the context of tract segmentation. Since each basis vector of NMF has a straightforward correspondence with each fiber tract bundle in the frequency domain and thereby fiber tract cluster label can be directly inferred without further clustering operations. In detail, we construct the nonnegative frequency-tract matrix using Fourier descriptors derived from one of the tract shape characterizations, i.e., the central angle dot product. This frequency-tract matrix is analogous to the term-document matrix in the document clustering context. In the NMF derived feature space, each basis vector captures the base characterization of a particular tract bundle. These basis vectors do not need to be orthogonal. This is different from the clustering methods based on SVD and the related spectral clustering methods. In this approach, each fiber tract is represented as an additive combination of the base shapes. The cluster label of each fiber tract is easily determined by finding the basis vector with which a fiber tract has the largest projection value.

6.3 Methods

6.3.1 Fiber Tract Parameter Fitting

The backward streamline based DTI tractography technique proposed by Mori and van Zijl [39] is employed in this analysis to reconstruct white matter fiber tracts. This tractography technique produces fiber tracts as spatial curves in the three dimensional space with unequal separation distances between successive step points. Fourier transform approach is dependent on the parameterization of the curves. This requires the parameterization to

be standardized. For this reason, all reconstructed tracts are fitted using a fixed geodesic arc length. Distinct fiber tracts have equal length unit but usually different numbers of step points.

6.3.2 Tract Characterization

Each step point on a fiber tract has its three dimensional coordinates representing its spatial position and a principal eigenvector indicating the local diffusion orientation in a specific voxel it falls in. We define a fiber tract's global diffusion orientation as the accumulation of local diffusion orientations. Assume $e = \{e_1,\ e_2,\ \ldots,\ e_l\}$ is the set of local diffusion orientations of a fiber tract, then the global diffusion orientation e_g is given by $e_g = \sum_{i=1}^{l} e_i$.

A voxel's diffusion orientation e_i is not equivalent to its associated principal eigenvector in the sense that a diffusion orientation is symmetrically bi-directional while a principal eigenvector is directional. In order to get the correct global orientation e_g, we need to check the directional consistency of the principal eigenvectors. In detail, we start from any one of the two end points of a fiber tract and move towards its unique successive step point. If the dot product between the principal eigenvector and this initial moving direction is negative, we reverse the the principal eigenvector of that point. Then we move forward following the direction of this checked principal eigenvector. At each intermediate step point, if the dot product of the two principal eigenvectors belonging to this step point and its previous neighbor are negative, we reverse the one belonging to this step point and repeat this procedure until reach the other end of this fiber tract.

The central angle dot product (CADP) is defined as the absolute value of the dot product between a step point's local diffusion orientation and the global diffusion orientation of the tract

$$\frac{|e_i^T \cdot e_g|}{\|e_i\|\|e_g\|}.$$

6.3.3 Transformation of Tract Characterizations into Frequency Space

We compute the discrete Fourier transform of a tract as

$$FD(i) = \frac{1}{l}\sum_{k=1}^{l} s(k)\exp(\frac{-j2\pi ik}{l}),\ i = 1, 2, \ldots, l, \tag{6.1}$$

where $s(k),\ k = 1, 2, \ldots, l$, is the CADP shape characterization at the kth point, and $j = \sqrt{-1}$. The coefficients $FD(i),\ i = 1, 2, \ldots, l$, are called Fourier descriptors of the characterization of a fiber tract. Since the shape characterization that we introduced are all real values, there are only $l/2$ different frequencies in the discrete Fourier transform. If l is an odd number, the number of different frequencies is $(l + 1)/2$. In the following discussion, we assume that l is even for convenience. Therefore, only a half of the Fourier descriptors are needed.

Fourier descriptors transform the fiber tract characterization from the spatial domain into a frequency domain. This eliminates the difficulty to establish matching correspondence between two randomly organized fiber tracts in the spatial domain. The number of coefficients from Fourier transform is usually large, but a small subset of these coefficients is sufficient to capture the general characterization features of a fiber tract. The coefficients corresponding to very high frequencies are not helpful in fiber tract characterization differentiation. These high frequency components can be ignored without significant accuracy loss for fiber tract clustering. The lower order components also help filter out noise dependent perturbations. As a result, the dimension of Fourier descriptors used for fiber tract clustering are significantly reduced. In addition, two fiber tracts compared based on the Fourier descriptors do not have to have the same numbers of step points. Consequently, Fourier descriptors can be employed in matching of fiber tracts with unequal length.

To encode a fiber tract with nonnegative values, we discard Fourier descriptors' phase information and keep only their magnitudes. These magnitudes are all nonnegative. This also makes Fourier descriptors rotation invariant without any loss of encoding accuracy in the context of this study. In the following discussion, we use $f(i)$ to represent a Fourier

descriptor's magnitude, i.e., $f(i) = |FD(i)| \geq 0$. We also refer $f(i)$ as a Fourier descriptor for simplicity though it is actually a Fourier descriptor's magnitude. Now, each fiber tract can be encoded by a encoding vector, f, composed of a set of Fourier descriptors $f = [f(1), \ldots, f(i), \ldots, f(m)]$ with all $f(i) \geq 0$ for $i = 1, 2, \ldots, m$, where m ($\leq l/2$) is the number of truncated Fourier descriptors.

6.3.4 Clustering based on Nonnegative Matrix Factorization

To construct the nonnegative frequency-tract matrix, we put each fiber tract's encoding vector, e.g., for the jth tract, $f_j = [f_j(1), \ldots, f_j(i), \ldots, f_j(m)]$ into the jth column of a two dimensional (2D) matrix V. Assume n is the number of fiber tracts under consideration, the constructed nonnegative matrix V thus has the dimension $m \times n$.

We have expressed a set of fiber tracts as an $m \times n$ nonnegative frequency-tract matrix V. Each column V_j of V is an encoding of a fiber tract in the frequency domain and each entry v_{ij} of vector V_j is the significance of frequency i with respect to the fiber tract representation of V_j.

The NMF is defined as finding two low rank nonnegative matrix factors W and H of a given nonnegative matrix V such that $V \approx WH$ [118]. Each column of W is a basis vector and each column of H contains an encoding of the linear combination of the basis vectors that approximates the corresponding column of V. W and H each has the dimension $m \times r$ and $r \times n$ respectively. r is the number of clusters selected. Usually, $r \ll \min(m, n)$. Finding or estimating the approximate value of r depends on applications.

The approach using NMF to obtain factor matrices W and H in this study is to minimize the Frobenius norm of the difference $V - WH$, i.e., minimize $\|V - WH\|^2$ with respect to W and H with $W_{ij} \geq 0$ and $H_{ij} \geq 0$ for each i and j [118]. The updating rule to produce W and H is based on the multiplicative method proposed by Lee and Seung [118]. In the multiplicative method, we first initialize W and H with nonnegative values and then

perform iterations for each α, i, and j until convergence. The updating formulas are

$$H_{\alpha j} \leftarrow H_{\alpha j} \frac{(W^T V)_{\alpha j}}{(W^T W H)_{\alpha j}} \tag{6.2}$$

$$W_{i\alpha} \leftarrow W_{i\alpha} \frac{(V H^T)_{i\alpha}}{(W H H^T)_{i\alpha}} \tag{6.3}$$

At each iteration, W and H remain nonnegative and the columns of W or the basis vectors are normalized to unity. Updating W and H simultaneously generally yields better results than updating each matrix factor individually.

This multiplicative method is related to the expectation maximization (EM) technique used in image processing context and can be classified as a diagonally scaled gradient descent method. It is proved that the Euclidean distance $\|V - WH\|$ is monotonically non-increasing under the above multiplicative method updating rules, and that the convergence of the iteration is guaranteed [118].

We then use matrix H to identify the cluster membership of a fiber tract. In detail, for the jth fiber tract, we compare entries across rows on the jth column of H. Its cluster label is x if $x = \arg\max_i \{H_{ij}\}$.

6.4 Experiments and Results

6.4.1 Data Acquisition

The DTI data used in this study are from health controls which are described in Sections 1.3.2 and 2.4.1.

6.4.2 Experiments and Results

The real dataset used to assess the performance of this method is a fiber tract collection consisting of the corticospinal tract (CST) bundle and the medial cerebellar peduncle (MCP) bundle. It is denoted as CST-MCP dataset and shown in Figure 6.1(a). This data set has totally 310 fiber tracts. Figure 6.1(b) illustrates the segmented two sub-bundles, CST and MCP. Among the 310 fiber tracts, 199 and 111 of them are grouped into CST and MCP respectively.

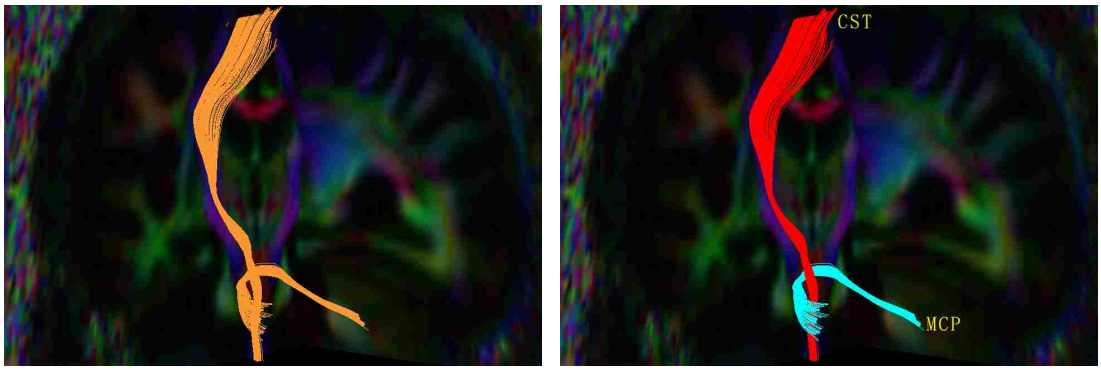

(a) Unclassified Tract Bundles (b) Classified CST and MCP bundles

Figure 6.1: Illustration of the clustering result using NMF technique. Subfigure (a) shows the reconstructed white matter tracts before clustering. Subfigure (b) demonstrates the two labeled bundles. The separated CST and MCP bundles are colored in red and light blue respectively.

In this test, the first 30 Fourier descriptors derived from the CADP shape signature of each fiber tract are used to form the nonnegative frequency-tract matrix V which thus has the dimension 30×310. The cluster number r is selected as 2. After applying NMF, the dimensions of the yielded nonnegative matrices W and H are 30×2 and 2×310 respectively. For the jth ($j = 1, 2, \ldots, 310$) fiber tract, we then compare the values of the two rows on the jth column of matrix H. Its cluster label is identified as the row index i ($i = 1, 2$) if this row has the larger value than that of another row.

Figure 6.2 graphically demonstrates the entry value comparisons between each two rows of the first 10 columns of the matrix H. Among these 10 fiber tracts, the first and last 3 (colored in red) are identified as CST. For each of them, the entry value on the first row (marked as +) is greater than that of the second row (marked as o), and vice versa for the middle four fiber tracts (colored in blue).

Figure 6.3 shows the corresponding first 10 fiber tracts colored according to their cluster labels.

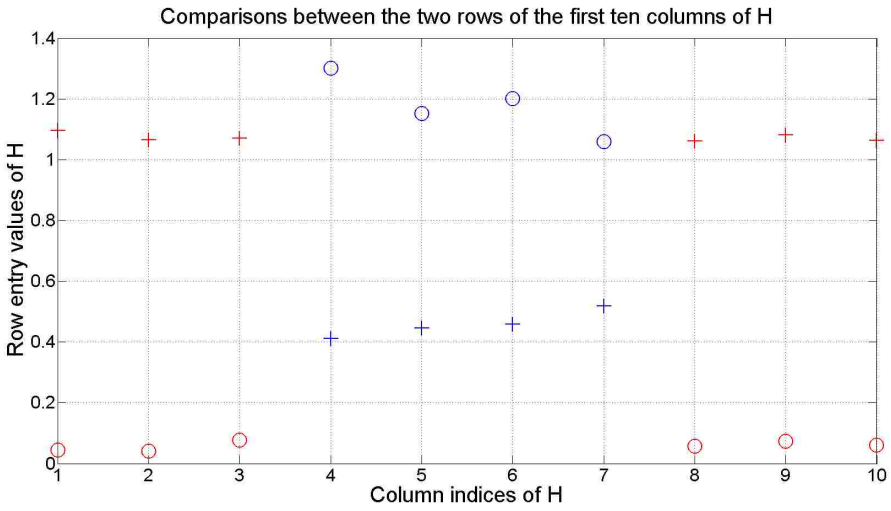

Figure 6.2: Value comparisons of elements in the first 10 columns of matrix H. Red: labeled as CST; Blue: labeled as MCP; +: first row; o: second row. Elements in the first and last three columns of the first row, which are colored in red, have larger values than that of the elements in the second row. The six tracts corresponding to these six matrix elements are labeled as CST. On the other hand, the four elements of the mid four columns of the second row which are colored in blue, have larger values than that of the elements in the first row. The four tracts corresponding to these four matrix elements are labeled into MCP bundle

6.5 Discussion and Conclusion

In this work, we presented a novel technique to group white matter fiber tracts reconstructed from DTI into bundles. This approach is based on NMF. The construction of the nonnegative frequency-tract matrix and the encoding of fiber tracts were described. Preliminary experimental results have been obtained and show that this technique can efficiently separate fascicles into plausible bundles.

In summary, NMF has mostly been applied to text mining and image analysis. Medical imaging, especially the white matter fiber tract analysis, may benefit from this technique as well. Problems such as identifying significant features in the encoded fiber tracts are natural candidates for applications of NMF. In such contexts, fiber tracts can be treated as analogous to text documents and the quantified weights of features to term frequencies. The basis feature vectors can be viewed as analogous to the base topics. With further

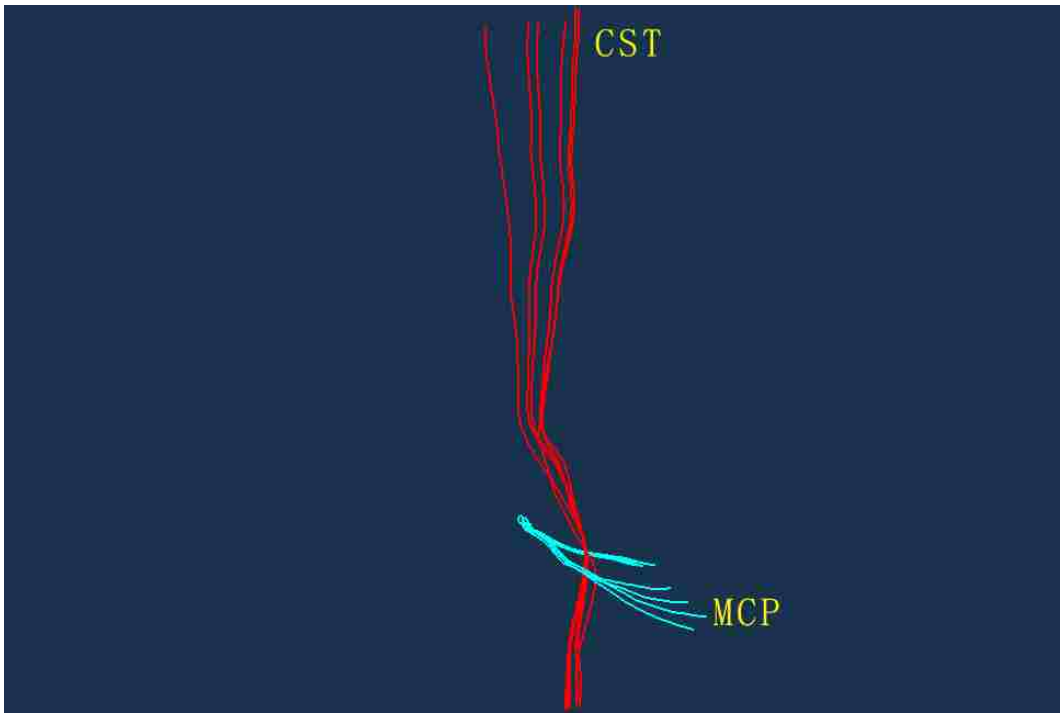

Figure 6.3: Illustration of the classified first 10 fiber tracts rendered in different colors.The red color six tracts are in correspondence with the six first row matrix entries of the first and last three columns in Figure 6.2. The four light blue colored tracts are in correspondence with the four second row matrix elements of the mid four columns in Figure 6.2.

development, it may be possible to apply NMF in quantifications of the deformation of white matter fibers under certain pathologies and brain diseases, e.g., tumor, or for clinical studies.

7 Summary and Outlook

7.1 Summary

In this dissertation, we have implemented a novel computing scheme to be able to estimate regional white matter alterations along neural pathways in 3D space. The mechanism of the proposed method relies on white matter tractography and geodesic distance mapping which establishes correspondences to allow direct cross-subject evaluations. For fibre bundles which are very thin and difficult to reconstruct their entire anatomically valid paths for all subjects in group analysis, we have proposed the white matter tract mask scheme to overcome this difficulty. Real DTI data have been employed to demonstrate the performance of the proposed technique. Experimental results have shown that regional white matter changes are accurately located and are in agreement with previous DTI studies. The proposed method bears great potential to provide a sensitive approach to determine the white matter integrity in human brain.

In order to quantify the individual characterization of white matter fiber tracts without the difficulties such as the spatial normalization which happens in spatial domain, we have presented a technique to transform the tract characterizations into the frequency domain. This technique has potentials to quantify the deformation of white matter fibers under certain pathologies and brain diseases, e.g., tumor, or for clinical group analysis. It also bears the potential to represent invariant tract patterns under translations, rotations and scaling. The Fourier descriptors can be a good candidate for clustering fiber tracts across subjects. With the help of this modeling technique, fiber tracts from a new individual could be matched to an atlas or a prototype in group studies. The methodology could thus be applied to in vivo data with the aim of classifying patients from normal controls by differentiating statistically normal and abnormal tract shapes and configurations.

To facilitate the single subject or group quantitative analysis, we have presented a new framework for clustering the reconstructed white matter tract bundles in DTI data based on

certain *a priori* anatomical knowledge. Strategies have developed to handle different situations. The heavy computing burden is largely reduced by eliminating both of the requirements to establish the point-wise correspondence between trajectory pairs and to perform the calculation at the level of the step points along white matter tracts. We have described the white matter tract representation in the format of a number of Fourier shape descriptors and geometric features. This representation provides the framework and the theoretical ground to reduce the noise effect inherent to the DTI data and the desired differentiating ability. In the framework, the distribution of fiber tracts is described by a multivariate Gaussian mixture model. This statistical model makes it feasible to exploit the fiber bundle's *a priori* knowledge in the format of the mean and covariance of fiber bundles. Anatomically meaningless white matter tracts are thus mostly avoided. In the case that we have little *a priori* knowledge, we use the expectation-maximization algorithm to perform the maximum likelihood estimation to label white matter tracts. On the other hand, if a set of white matter tract bundle atlas are given, we can directly label each trajectory by finding its maximum of the *a posterior* Bayesian probabilities among all the target classes. The method has the flexibility to conduct the grouping on a portion or all of the fiber tract set one time to accommodate different situations. In both cases, outliers have been handled by easily setting a posterior probability threshold. Real DTI data have been employed to evaluate the method. The experimental results show that the proposed technique is relatively effective and may offer an alternative for existing white matter tract clustering methods.

For a small amount of white matter tracts, a modeling and clustering algorithm with the capability of handling white matter tracts with unequal length and sharing no common starting region has been proposed and evaluated with real DTI data. Particularly, the objective representation of white matter tracts is achieved by incorporating the information of diffusion orientation, tract length and geometric center into the mathematical model. The quantitative measurements are implemented by calculating the pairwise affinity score which is sensitive to tract shape, location, and length. A matching method has been im-

plemented to establish piece-wise correspondences between two randomly located tracts. With further development, it may ultimately be possible to produce a standard atlas as tract architecture references, similar to the currently used brain image templates.

NMF has mostly been applied to text mining and image analysis. Medical imaging, especially the white matter fiber tract analysis, may benefit from this technique as well. We have described the construction of the nonnegative frequency-tract matrix and the encoding of fiber tracts in detail. Problems such as identifying significant features in the encoded fiber tracts are natural candidates for applications of NMF. In such contexts, fiber tracts can be treated as analogous to text documents and the quantified weights of features to term frequencies. The basis feature vectors can be viewed as analogous to the base topics. With further development, it may be possible to apply NMF in quantifications of the deformation of white matter fibers under certain pathologies and brain diseases, e.g., tumor, or for clinical studies.

7.2 Future Research Outlook

In addition to what we have described in our studies, there are several directions that we will be pursuing in the future research work.

1. Improve our fiber modeling. Although we have presented one comprehensive and efficient tract model, the effectiveness of the model will be tested with more DTI data and refined as needed. We will explore means to make our model to be learnable of new found bundle patterns. In the end, we will make our tract representation to be less dependent on the *a priori* anatomical knowledge.

2. Build a computational model for inter subject group fiber classification. We may tailor our model to represent tracts across subjects with appropriate normalization. To accurately represent tracts from different unregistered brains, the tract representation should be invariant to translation, scaling and rotation. We will improve our tract model to meet these needs, i.e., to be independent of individual brains so we can

quantitatively compare tracts across subjects. To achieve this goal, we will use the collection of anatomical knowledge of known tract bundles to normalize and generalize our tract bundle representation.

3. We will also make serious effort to develop a class of more efficient and robust clustering algorithm than that reported previously. We will improve our developed multidimensional features to work with clustering algorithms directly and consider hierarchical and spectral clustering approaches In the group or atlas based clustering, existing knowledge of fiber tract bundles can be used to train classifiers such as the Support Vector Machines to get better classification of fiber tracts coming from the unclassified brains. With further development, it may ultimately be possible to produce a standard fiber atlas as tract architecture references, similar to the currently used brain image templates. It thus has the potential to quantify the deformation of white matter fibers under certain pathologies and brain diseases, e.g., tumor, or for clinical group analysis. In group studies, fiber tracts from a new individual can be matched to an atlas or a prototype. The methodology could be applied to in vivo data with the aim of distinguishing patients from normal controls by differentiating statistically normal and abnormal tract shapes and configurations.

Bibliography

[1] D. LeBihan and E. Breton, Imagerie de diffusion in vivo par re'sonance magne'tique nucle'aire, *C. R. Acad. Sci. Paris*, Seri. I 301, pp. 1109-1112, 1985.

[2] K.-D. Merboldt, W. Hanicke, and J. Frahm, Self-diffusion NMR imaging using stimulated echoes, *Journal of Magnetic Resonance*, Vol. 64(3), pp. 479-486, 1985.

[3] D. G. Taylor and M. C. Bushell, The spatial mapping of translational diffusion coefficients by the NMR imaging technique, *Physics in Medicine and Biology*, Vol. 30(4), pp. 345-349, 1985.

[4] D. LeBihan, Molecular diffusion nuclear magnetic resonance imaging, *Magnetic Resonance Quarterly*, Vol. 7(1), pp. 1-30, 1991.

[5] P. J. Basser and C. Pierpaoli, Microstructural and physiological features of tissues elucidated by quantitative-diffusion-tensor MRI, *Journal of Magnetic Resonance Series B*, Vol. 111(3), pp. 209-219, 1996.

[6] S. Warach, D. Chien, W. Li, M. Ronthal, and R. R. Edelman, Fast magnetic resonance diffusion-weighted imaging of acute human stroke, *Neurology*, Vol. 42(9), pp. 1717-1723, 1992.

[7] M. E. Moseley, Y. Cohen, J. Mintorovitch, L. Chileuitt, H. Shimizu, J. Kucharczyk, M. F. Wendland, and P. R. Weinstein, Early detection of regional cerebral ischemia in cats: comparison of diffusion- and T2-weighted MRI and spectroscopy, *Magnetic Resonance in Medicine*, Vol. 14, pp. 330-346, 1990.

[8] G. G. Cleveland, D. C. Chang, C. F. Hazlewood, and H. E. Rorschach, Nuclear magnetic resonance measurement of skeletal muscle: anisotrophy of the diffusion coefficient of the intracellular water, *Biophysical Journal*, Vol. 16(9), pp. 1043-1053, 1976.

[9] M. E. Moseley, Y. Cohen, J. Kucharczyk, J. Mintorovitch, H. S. Asgari, M. F. Wendland, J. Tsuruda, and D. Norman, Diffusion-weighted MR imaging of anisotropic water diffusion in cat central nervous system, *Radiology*, Vol. 176(2), pp. 439-445, 1990.

[10] T. L. Chenevert, J. A. Brunberg, and J. G. Pipe, Anisotropic diffusion in human white matter: demonstration with MR techniques in vivo, *Radiology*, Vol. 177(2), pp. 401-405, 1990.

[11] M. F. Lythgoe, A. L. Busza, F. Calamante, C. H. Sotak , M. D. King, A. C. Bingham, S. R. Williams, and D. G. Gadian, Effects of diffusion anisotropy on lesion delineation in a rat model of cerebral ischemia, *Magnetic Rosonance in Medicine*, Vol. 38(4), pp. 662-668, 1997.

[12] C. A. Clark, D. J. Werring, and D. H. Miller, Diffusion imaging of the spinal cord in vivo: estimation of the principal diffusivities and application to multiple sclerosis, *Magnetic Rosonance in Medicine*, Vol. 43(1), pp. 133-138, 2000.

[13] N. G. Papadakisa, D. Xing, C. L.-H. Huangb, L. D. Halla, and T. A. Carpenter, A Comparative Study of Acquisition Schemes for Diffusion Tensor Imaging Using MRI, *Journal of Magnetic Resonance*, Vol. 137(1), pp. 67-82, 1999.

[14] C. Pierpaoli, P. Jezzard, P. J. Basser, A. Barnett, and G. Di Chiro, Diffusion tensor MR imaging of the human brain, *Radiology*, Vol. 201(3), pp. 637-648, 1996.

[15] P. J. Basser, New histological and physiological stains derived from diffusion-tensor MR images, *Imaging Brain Structure and Function Volume 820 of the Annals of the New York Academy of Sciences*, Vol. 30, pp. 123-138, 1997.

[16] S. Mori and P. C. Van Zijl, Diffusion weighting by the trace of the diffusion tensor within a single scan, *Magnetic Resonance in Medicine*, Vol. 33(1), pp. 41-52, 1995.

[17] C. Pierpaoli and P. J. Basser, Toward a quantitative assessment of diffusion anisotropy, *Magnetic Resonance in Medicine*, Vol. 36(6), pp. 893-906, 1996.

[18] B. Stieltjes, W. E. Kaufmann, P. C. Van Zijl, K. Fredericksen, G. D. Pearlson, M. Solaiyappan, and S. Mori, Diffusion tensor imaging and axonal tracking in the human brainstem, *NeuroImage*, Vol. 14, pp. 723-735, 2001.

[19] D. LeBihan, J. F. Mangin, C. Pouponm, C. A. Clark, S. Pappata, N. Molko, and H. Chabriat, Diffusion tensor imaging: Concepts and applications, *Journal of Magnetic Resonance Imaging*, Vol. 13, pp. 534-546, 2001.

[20] S. Mori and P. B. Barker, Diffusion magnetic resonance imaging: its principle and applications, *The Anatomical Record*, Vol. 257(3), pp. 102-109, 1999.

[21] R. Parasuraman and P. M. Greenwood, Selective attention in aging and dementia, *The attentive brain*, pp. 461-487, Cambridge, MA, US: The MIT Press, 1998.

[22] M. O'Sullivan, P. E. Summers, D. K. Jones, J. M. Jarosz, S. C. Williams, and H. S. Markus, Normal-appearing white matter in ischemic leukoaraiosis: a diffusion tensor MRI study, *Neurology*, Vol. 57(12), pp. 2307-2310, 2001.

[23] S. E. Rose, K. L. McMahon, A. L., Janke, B. O'Dowd, G. de Zubicaray, M. W. Strudwick, and J. B. Chalk, MRI diffusion indices and neuropsychological performance in amnestic mild cognitive impairment, *Journal of Neurology, Neurosurgery, and Psychiatry*, Vol. 77(10), pp. 1122-1128, 2006.

[24] D. Medina, L. DeToledo-Morrell, F. Urresta, J. D. Gabrieli, M. Moseley, D. Fleischman, D. A. Bennett, S. Leurgans, D. A. Turner, and G. T. Stebbins, White matter changes in mild cognitive impairment and AD: A diffusion tensor imaging study, *Neurobiology of Aging*, Vol. 27(5), pp. 663-672, 2006.

[25] Y. Zhang, N. Schuff, G-H. Jahng, W. Bayne, S. Mori, L. Schad, S. Mueller, A-T. Du, J. H. Kramer, K. Yaffe, H. Chui, W. J. Jagust, B. L. Miller, and M. W. Weiner, Diffusion tensor imaging of cingulum fibers in mild cognitive impairment and Alzheimer disease, *Neurology*, Vol. 68(1), pp. 13-19, 2007.

[26] P. J. Basser and D. K. Jones, Diffusion-tensor MRI: Theory, experimental design and data analysis - a technical review, *NMR in Biomedicine*, Vol. 15(7-8), pp. 456-467, 2002.

[27] P. J. Basser, S. Pajevic, C. Pierpaoli, J. Duda, and A. Aldroubi, In vivo fiber tractography using DT-MRI data, *Magnetic Resonance in Medicine*, Vol. 44(4), pp. 625-632, 2000.

[28] A. T. Du, N. Schuff, D. Amend, M. P. Laakso, Y. Hsu, W. Jagust, K. Yaffe, J. Kramer, B. Reed, D. Norman, H. Chui, and M. Weiner, Magnetic resonance imaging of the entorhinal cortex and hippocampus in mild cognitive impairment and Alzheimer's disease, *Journal of Neurology, Neurosurgery, and Psychiatry*, Vol. 71(4), pp. 441-447, 2001.

[29] V. Jelic, O. Almkvist, L. O. Wahlund, B. Winblad, S. Valind, and A. Nordberg, Impaired cerebral glucose metabolism and cognitive functioning predict deterioration in mild cognitive impairment, *NeuroReport*, Vol. 12(4), pp. 851-855, 2001.

[30] E. Pagani, M. Filippi, M. A. Rocca, and M. A. Horsfield, A method for obtaining tract-specific diffusion tensor MRI measurements in the presence of disease: Application to patients with clinically isolated syndromes suggestive of multiple sclerosis, *NeuroImage*, Vol. 26(1), pp. 258-265, 2005.

[31] P.J. Bassser, J. Mattiello, and D. LeBihan, MR diffusion tensor spectroscopy and imaging, *Biophysical Journal*, Vol.66(1), pp. 259-267, 1994.

[32] S. C. Patridge, P. Mukherjee, J. T. Berman, R. G. Henry, S. P. Miller, Y. Lu, O. A. Glenn, D. Ferriero, A. J. Barkovich, and D. B. Vigneron, Tractography-based quantitation of diffusion tensor imaging parameters in white matter tracts of preterm newborns, *Journal of Magnetic Resonance Imaging*, Vol. 22(4), pp. 467-474, 2005.

[33] F. Lin, C. Yub, T. Jiang, K. Lib, X. Li, W. Qin, H. Sun, and P. Chan, Quantitative analysis along the pyramidal tract by length-normalized parameterization based on diffusion tensor tractography: Application to patients with relapsing neuromyelitis optica, *NeuroImage*, Vol. 33(1), pp. 154-160, 2006.

[34] D. M. Weinstein, J. S. Tsuruda, K. M. Hasan, K. Arfanakis, M. E. Meyerand, B. Badie, H. A. Roowley, V. Haughton, A. Field, and A. L. Alexander, White matter tractography using diffusion tensor deflection, *Human Brain Mapping*, Vol. 18, pp. 306-321, 2003.

[35] J. Zhang, N. Kang, and S. E. Rose, Approximating anatomical brain connectivity with diffusion tensor MRI using kernel-based diffusion simulations, *In Proceedings of Information Processing in Medical Imaging (IPMI 2005)*, Vol. 19, pp. 64-75, 2005.

[36] J. Zhang and X. Liang, Diffusion tensor analysis of white matter pathways of amnestic mild cognitive impairment, *in Hot Topics Addendum of the Alzheimer's Association International Conference on Prevention of Dementia*, pp. 227, Washington, DC, USA, June, 2007.

[37] N. Kang, J. Zhang, E. S. Carlson, and D. Gembris, White matter fiber tractography via anisotropic diffusion simulation in the human brain, *IEEE Transactions on Medical Imaging*, Vol. 24(9), pp. 1127-1137, 2005.

[38] S. Mori, B. J. Crain, V. P. Chacko, and P. C. Van Zijl, Three-dimensional tracking of axonal projections in the brain by magnetic resonance imaging, *Annals of Neurology*, Vol. 45(2), pp. 265-269, 1999.

[39] S. Mori and P. C. Van Zijl, Fiber tracking: principles and strategies - a technical review, *NMR in Biomedicine*, Vol. 15(7-8), pp. 468-480, 2002.

[40] P. van Gelderen, M. H. de Vleeschouwer, D. DesPres, J. Pekar, P. C. van Zijl, and C. T. Moonen, Water diffusion and acute stroke, *Magnetic Resonance in Medicine*, Vol. 31(2), pp. 154-163, 1994.

[41] D. LeBihan, Diffusion and Perfusion Magnetic Resonance Imaging: Applications to Functional MRI, *New York: Raven Press*, 1995.

[42] P. J. Basser, J. Mattiello, and D. LeBihan, Estimation of the effective self-diffusion tensor from the NMR spin echo, *Journal of Magnetic Resonance Series B*, Vol. 103(3), pp. 247-254, 1994.

[43] P. J. Basser, J. Mattiello, and D. LeBihan, Diagonal and off-diagonal components of the self-diffusion tensor: their relation to and estimation from the NMR spin-echo signal, *in Proceedings of the 11th Annual Meeting of SMRM*, Vol. 1, pp. 1222. Berlin, 1992.

[44] C.-F. Westin, S.E. Maier, B. Khidhir, P. Everett, F.A. Jolesz, and R. Kikinis, Image Processing for Diffusion Tensor Magnetic Resonance Imaging, *In Proceedings of Second Int. Conf. on Medical Image Computing and Computer-assisted Interventions (MICCAI99)*, pp. 441-452, 1999.

[45] S.E. Maier, M. E. Shenton, and F. A. Jolesz, Diffusion MRI explores new indications, *Diagnostic Imaging, Advanced MR Supplement 2001*, Dec. 2001.

[46] National Institutes of Health (NIH), Diffusion Tensor Magnetic Resonance Imaging, *NIH news, Dec. 2000*, Dec. 2000.

[47] C. Poupon, J. Mangin, C. A. Clark, V. Frouin, J. Rgi, D. LeBihan, and I. Bloch, Towards inference of human brain connectivity from MR diffusion tensor data, *Medical Image Analysis*, Vol. 5(1), pp. 1-15, 2001.

[48] M. R. Wiegell, T. Reese, D. S. Tuch, A. G. Sorensen, and V. J. Wedeen, Diffusion Spectrum Imaging of Fiber White Matter Degeneration, *In Proceedings of the International Society for Magnetic Resonance Medicine (ISMRM)*, Vol. (9), pp. 504, 2001.

[49] D. Gembris, H. Schumacher, and D. Suter, Solving the Diffusion Equation for Fiber Tracking in the Living Human Brain, *In Proceedings of the International Society for Magnetic Resonance Medicine (ISMRM)*, Vol. 9, pp. 1529, Glasgow, Scotland, April 2001

[50] Z. Ding, J. C. Gore, and A. W. Anderson, Tracking, Bundling and Quantitatively Characterizing in vivo Neuronal Fiber Pathways Using Diffusion Tensor Magnetic Resonance Imaging, *In Proceedings of the International Society for Magnetic Resonance Medicine (ISMRM)*, Vol. 9, pp. 1530, Glasgow, Scotland, April 2001.

[51] J. Zhang and X. Liang, Diffusion tensor analysis for detecting white matter changes in mild cognitive impairment, *The Journal of the Alzheimer's Association*, Vol. 4(4), (Suppl 2):T70, 2008.

[52] T. E. Conturo, N. F. Lori, T. S. Cull, E. Akbudak, A. Z. Snyder, J. S. Shimony, R. C. McKinstry, H. Burton, and M. E. Raichle, Tracking neuronal fiber pathways in the living human brain, *In Proceedings of the National Academy of Sciences of the United States of America*, Vol. 96(18), pp. 10422-10427, August 1999.

[53] X. Liang, N. Kang, S. E. Rose, and J. Zhang, A framework for quantitative and visual analysis of white matter integrity using diffusion tensor imaging, *International Journal of Functional Informatics and Personalised Medicine (IJFIPM)*, Vol.2(2), pp. 159-174, 2009.

[54] X. Liang, Q. Zhuang, N. Cao, and J. Zhang, Quantitative and visual analysis of white matter integrity using diffusion tensor imaging, *Proceedings of the International Society for Optical Engineering (SPIE) Medical Imaging 2009 (SPIE 2009)*, Vol. 7261, 726131 (2009), Lake Buena Vista (Orlando Area), Florida, USA, February, 2009.

[55] S. Zhang, C. Demiralp, and D. Laidlaw, Visualizing Diffusion Tensor MR Images Using Streamtubes and Streamsurfaces, *IEEE Trans. Visualization and Computer Graphics*, Vol. 9, pp. 454-462, 2003.

[56] D. Xu, S. Mori, M. Solaiyappan, P. C. van Zijl, and C. Davatzikos, A framework for callosal fiber distribution analysis, *Neuroimage*, Vol. 17(3), pp. 1131-1143, 2002.

[57] C.-F. Westin, S. E. Maier, H. Mamata, A. Nabavi, F. A. Jolesz, and R. Kikinis, Processing and Visualization of Diffusion Tensor MRI, *Medical Image Analysis*, Vol. 6(2), pp. 93-108, 2002.

[58] D. S. Tuch, M. R. Wiegell, T. G. Reese, J. W. Belliveau, and V. J. Wedeen, Measuring Cortico-Cortical Connectivity Matrices with Diffusion Spectrum Imaging, *In Proceedings of the International Society for Magnetic Resonance Medicine (ISMRM)*, Vol. 9, pp. 502, Glasgow, Scotland, April 2001, .

[59] G. J. M. Parker, Tracing Fibre Tracts Using Fast Marching, *In Proceedings of the International Society for Magnetic Resonance Medicine (ISMRM)*, Vol. 8, pp. 85, Denver, Colorado, USA, April 2000.

[60] D. Gering, A. Nabavi, R. Kikinis, W. E. L. Grimson, N. Hata, P. Everett, F. A. Jolesz, and W.Wells III, An Integrated Visualization System for Surgical Planning and Guidance using Image Fusion and Interventional Imaging, *In Proceedings of Medical Image Computing and Computer-Assisted Intervention (MICCAI)*, pp. 809-819, Cambridge, England, September 1999.

[61] OpenGL, OpenGL is a registered trademark of Silicon Graphics, Inc. More information available at http://www.sgi.com/software/opengl, last visited May 2011.

[62] P. Fillard and G. Gerig, Analysis tool for diffusion tensor MRI, *Medical Image Computing and Computer-Assisted Intervention - MICCAI 2003, Lecture Notes in Computer Science*, Vol. 2879/2003, pp. 967-968, 2003.

[63] The Visualization ToolKit (VTK), More information available at http://www.kitware.com/vtk, last visited May 2011.

[64] S. Xie, J. X. Xiao, Y. H. Wang, H. K. Wu, G. L. Gong, and X. X. Jiang, Evaluation of bilateral cingulum with tractography in patients with Alzheimer's disease, *NeuroReport*, Vol. 16(12), pp. 1275-1278 , 2005.

[65] S. M. Smith, M. Jenkinson, H. Johansen-Berg, D. Rueckert, T. E. Nichols, C. E. Mackay, K. E. Watkins, O. Ciccarelli, M. Z. Cader, P. M. Matthews, and T. E. Behrens, Tract-based spatial statistics: voxelwise analysis of multi-subject diffusion data, *Neuroimage*, Vol. 31(4), pp. 1487–1505, 2006.

[66] P. J. Nestor, T. D. Fryer, and J. R. Hodges, Declarative memory impairments in Alzheimer's disease and semantic dementia, *NeuroImage*, Vol. 30(3), pp. 1010-1020, 2006.

[67] N. R. Selden, D. R. Gitelman, N. Salamon-Murayama, T. B. Parrish, and M. M. Mesulam, Trajectories of cholinergic pathways within the cerebral hemispheres of the human brain, *Brain*, Vol. 121(12), pp. 2249-2257, 1998.

[68] G. Gong, T. Jiang, C. Zhu, Y. Zang, F. Wang, S. Xie, J. Xiao, and X. Guo, Asymmetry analysis of cingulum based on scale-invariant parameterization by diffusion tensor imaging, *Human Brain Mapping*, Vol. 24(2), pp. 92-98, 2005.

[69] B. N. Axelrod, J. J. Ryan and L.C. Ward, Evaluation of seven-subtest short forms of the Wechsler Adult Intelligence Scale-III in a referred sample, *Archives of Clinical Neuropsychology*, Vol. 16, pp. 1-8, 2001.

[70] D. Wechsler, Wechsler Adult Intelligence Scale - Third Edition, *New York: Psychological Corporation*, 1997.

[71] D. Wechsler, Wechsler Memory Scale - Third Edition, *New York: Psychological Corporation*, 1997.

[72] O. Spreen and E. Strauss, A compendium of neuropsychological tests - Second Edition, *New York: Oxford University Press*, 1998.

[73] E. Kaplan, H. Goodglass and S. Weintraub, Boston Naming Test, *Philadelphia: Lea and Febiger*, 1983.

[74] R. M. Reitan and D. Wolfson, The Halstead-Reitan Neuropsychological Test Battery: Theory and clinical interpretation, *Tuscon, AZ: Neuropsychology Press*, 1993.

[75] E. K. Warrington and M. James, The visual object and space perception battery, *Bury St. Edmunds, UK: Thames Valley test Company*, 1991.

[76] R.C. Petersen, G.E. Smith, S.C.Waring, R.J. Ivnik, E.G. Tangalos, and E. Kokmen, Mild Cognitive Impairment, *Archives of Neurology*, Vol. 56, pp. 303-308, 1999.

[77] R.C. Petersen, R.G. Thomas, M. Grundman, D. Bennett, R. Doody, S. Ferris S, D. Galasko, S. Jin, J. Kaye, A. Levey, E. Pfeiffer, M. Sano, C.H. van Dyck, and L. J. Thal, Vitamin E and donepezil for the treatment of mild cognitive impairment, *New England Journal of Medicine*, Vol. 352, pp. 2378-2388, 2005.

[78] G. McKhann, D. Drachman, M. Folstein, R. Katzman, D. Price and E. M. Stadlan, Clinical diagnosis of Alzheimer's disease: report of the NINCDS-ADRDA Work Group under the auspices of Department of Health and Human Services Task Force on Alzheimer's Disease, *Neurology*, Vol. 34, pp. 939-944, 1984.

[79] American Psychiatric Association, Diagnostic and statistical manual of mental disorders - Fourth Edition - Revised, *Washington, DC: American psychiatry Association*, 1994.

[80] L.O. Wahlund, F. Barkhof, F. Fazekas, MD; L. Bronge, M. Augustin, M. Sjoren, A. Wallin, H. Ader, D. Leys, L. Pantoni, F. Pasquier, T. Erkinjuntti and P. Scheltens, A new rating scale for age related white matter changes applicable to MRI and CT, *Stroke*, Vol. 32, pp. 1318-1322, 2001.

[81] D. K. Jones, M. A. Horsefield and A. Simmons, Optimal strategies for measuring diffusion in anisotropic systems by magnetic resonance imaging, *Magnetic Resonance in Medicine*, Vol. 42, pp. 515-525, 1999.

[82] J.A. Lucas, R.J. Ivnik, G.E. Smith, D. L. Bohac, E.G.Tangalos, N.R. Graff-Radford, and R.C. Petersen, Mayos older American normative studies: Category fluency norms, *Journal of Clinical and Experimental Neuropsychology*, Vol. 20(2), pp. 194-200, 1998.

[83] J. Mazziotta, A. Toga, A Evans, P. Fox, J. Lancaster, K. Zilles, R. Woods, T. Paus, G. Simpson, B. Pike, C. Holmes, L. Collins, P. Thompson, D. MacDonald, M. Iacoboni, T. Schormann, K. Amunts, N. Palomero-Gallagher, S. Geyer, L. Parsons, K. Narr, N. Kabani, G. Le Goualher, D. Boomsma, T. Cannon, R. Kawashima, and B. Mazoyer, A probabilistic atlas and reference system for the human brain: International consortium for brain mapping (ICBM), *Philosophical Transactions of the Royal Society B: Biological Sciences*, Vol. 356(1412), pp. 1293-1322, 2001.

[84] D.L. Collins, P. Neelin, T.M. Peters, and A. C. Evans, Automatic 3D intersubject registration of MR volumetric data in standardized Talairach space, *Journal of Computer Assisted Tomography*, Vol. 18(2), pp. 192-205, 1994.

[85] K. J. Worsley, C. H. Liao, J. Aston,V. Petre, G. H. Duncan, F. Morales, and A. C. Evans A General Statistical Analysis for fMRI Data, *Neuroimage*, Vol. 15, pp. 1-15, 2002.

[86] E. Kishon, T. Hastie, and H. J. Wolfson, 3-D Curve Matching Using Splines, *ECCV '90: Proceedings of the First European Conference on Computer Vision, Lecture Notes in Computer Science*, Vol. 427, pp. 589-591, 1990

[87] X. Liang and J. Zhang, White matter integrity analysis along the cingulum paths in mild cognitive impairment - a geodesic distance approach, *In Proceedings of the 2nd International Conference on Bioinformatics and Biomedical Engineering (iCBBE 2008)*, Vol. 1, pp. 510-513, Shanghai, China, May, 2008

[88] C. Lin, S. Lu, X. Liang, J. Hua, and O. Muzik, Cocluster Analysis of Thalamo-Cortical Fiber Tracts Extracted from Diffusion Tensor MRI, *International Journal of Data Mining and Bioinformatics (IJDMB)*, Vol. 2(4), pp. 342-361, 2008.

[89] X. Liang, Q. Zhuang, N. Cao, and J. Zhang, Shape modeling and clustering of white matter fiber tracts using Fourier descriptors, *In Proceedings of the IEEE Symposium on Computational Intelligence in Bioinformatics and Computational Biology (CIBCB 2009)*, pp. 292-297, Nashville, TN, USA, March 30 - April 2, 2009.

[90] X. Liang, J. Wang, Z. Lin, and J. Zhang, White matter fiber tract segmentation using nonnegative matrix factorization, *In Proceedings of the 3rd International Conference on Bioinformatics and Biomedical Engineering (iCBBE 2009)*, Vol. 1, pp. 1-4, Beijing, China, June 11 - 13, 2009.

[91] S. Warfield, M. Kaus, F. A. Jolesz, and R. Kikinis, Adaptive Template Moderated Spatially Varying Statistical Classification, In Proceedinds of Medical Image Computing and Computer-assisted Inverventions (MICCAI), pp. 231-238, 1998.

[92] W. M. Wells III, W. E. L. Grimson, R. Kikinis, and F. A. Jolesz, Adaptive Segmentation of MRI Data, *IEEE Transactions on Medical Imaging*, Vol. 15, pp. 429-442, 1996.

[93] S. Mori, W.E. Kaufmann, C. Davatzikos,B. Stieltjes,L. Amodei, K. Fredericksen, G.D. Pearlson, E.R. Melhem, M. Solaiyappan, G.V. Raymond, H. W. Moser, and P.C. van Zijl, Imaging cortical association tracts in the human brain using diffusion-tensor-based axonal tracking, *Magnetic Resonance in Medicine*, Vol. 47(2), pp. 215-223, 2002.

[94] Z. Ding, J. C. Gore, and A. W. Anderson, Classification and quantification of neuronal fiber pathways using diffusion tensor MRI, *Magnetic Resonance in Medicine*, Vol. 49(4), pp. 716-721, 2003.

[95] A. Brun, H. Knutsson, H.-J. Park, M. E. Shenton, and C.-F. Westing, Clustering fiber tracts using normalized cuts, *In Proceedings of Medical Image Computing and Computer-Assisted Intervention (MICCAI 2004), Lecture Notes in Computer Science*, Vol. 3216, pp. 368-375, 2004.

[96] I. Corouge, S. Gouttard, and G. Gerig, Towards a shape model of white matter fiber bundles using diffusion tensor MRI, *In Proceedings of International Symposium on Biomedical Imaging (ISBI)*, Vol. 1(5), pp. 344-347, 2004.

[97] G. Gerig, S. Gouttard, and I. Corouge, Analysis of brain white matter via fiber tract modeling, *In Proceedings of the 26th Annual International Conference of the IEEE Engineering in Medicine and Biology Society*, pp. 4421-4424, 2004.

[98] Y. Xia, U. Turken, S. L. Whitfield-Gabrieli, and J. D. Gabrieli, Knowledge-based classification of neuronal fibers in entire brain, *In Proceedings of Medical Image Computing and Computer-Assisted Intervention (MICCAI 2005), Lecture Notes in Computer Science*, Vol. 3749, pp. 205-212, 2005.

[99] L. Jonasson, P. Hagmann, J.-P. Thiran, and V. J. Wedeen, Fiber tracts of high angular resolution diffusion MRI are easily segmented with spectral clustering, *In Proceedings of 13th Annual Meeting of International Society for Magnetic Resonance in Medicine*, pp. 1310, 2005.

[100] V. El Kouby, Y. Cointepas, C. Poupon, D. Riviere, N. Golestani, J.-B. Poline, D. LeBihan, and J.-F. Mangin, MR diffusion-based inference of a fiber bundle model from a population of subjects, *In Proceedings of Medical Image Computing and Computer-Assisted Intervention (MICCAI 2005), Lecture Notes in Computer Science*, pp. 196-204, 2005.

[101] P. G. Batchelor, F. Calamante, J.-D. Tournier, D. Atkinson, D.L.G. Hill, and A. Connelly, Quantification of the shape of fiber tracts, *Magnetic Resonance in Medicine*, Vol. 55, pp. 894-903, 2006.

[102] L. J. O'Donnell, M. Kubicki, M. E. Shenton, M. H. Dreusicke, W. E. L. Grimson, and C.-F. Westin, A method for clustering white matter fiber tracts, *American Journal of Neuroradiology (AJNR)*, Vol. 27, pp. 1032-1038, 2006.

[103] L. J. O'Donnell and C.-F. Westin, Automatic tractography segmentation using a high-dimensional white matter atlas, *IEEE Transaction on Medical Imaging*, Vol. 26(11), pp. 1562-1575, 2007.

[104] J. Klein, P. Bittihn, P. Ledochowitsch, H. K. Hahn, O. Konrad, J. Rexilius, and H.-O. Peitgen, Grid-based spectral fiber clustering, *In Proceedings of Proceedings of SPIE, Medical Imaging 2007: Visualization and Image-Guided Procedures*, Vol. 6509(1), pp. 65097E, 2007.

[105] M. Maddah, W. E. Grimson, S. K. Warfield, and W. M. Wells, A unified framework for clustering and quantitative analysis of white matter fiber tracts, *Medical image analysis*, Vol. 12(2), pp. 191-202, 2008.

[106] B. Moberts, A. Vilanova, J. J. van Wijk, Evaluation of fiber clustering methods for diffusion tensor imaging, *In Proceedings of IEEE Visualization 2005*, pp. 65-72, 2005.

[107] R. Chellappa and R. Bagdazian, Fourier coding of image boundaries, *IEEE Transaction on Pattern Analysis and Machine Intelligence*, vol. 6(1), pp. 102-105, 1984.

[108] P.J. van Otterloo, A Contour-Oriented Approach to Shape Analysis, *Prentice Hall*, 1992.

[109] C.-L. Huang and D.-H. Huang, A Content-based image retrieval system, *Image and Vision Computing*, vol. 16, pp. 149-163, 1998.

[110] D. S. Zhang and G. Lu, A comparative study on shape retrieval using Fourier descriptors with different shape signatures, *In Proceedings of International Conference on Intelligent Multimedia and Distance Education(ICIMADE01)*, pp. 1-9, Fargo, ND, USA, 2001.

[111] C.T. Zahn and R.Z. Roskies, Fourier descriptors for plane closed curves, *IEEE Transaction on Computer*, vol. c-21(3), pp. 269-281, 1972.

[112] D.N. Do and S. Osowski, Shape recognition using FFT preprocessing and neural network, *The International Journal for Computation and Mathematics in Electrical and Electronic Engineering*, Vol. 17(5/6), pp. 658-666, 1998.

[113] R.O. Duda, P.E. Hart, and D. G. Stork, Pattern Classification - 2nd Edition, *John Wiley and Sons, Inc.*, 2000.

[114] C.M. Bishop, Pattern Recognition and Machine Learning, *Springer*, 2007.

[115] A. P. Dempster, N. M. Laird, and D. B. Rubin, Maximum likelihood from incomplete data via the EM algorithm, *Journal of the Royal Statistical Society*, Vol. B39(1), pp. 1-38, 1977.

[116] G. J. McLachlan, T. Krishnan, The EM Algorithm and its Extensions, *Wiley*, 1997.

[117] W. Xu, X. Liu, and Y. Gong, Document clustering based on non-negative matrix factorization, *In Proceedings of the 26th Annual International ACM SIGIR Conference on Research and Development in Informaion Retrieval*, pp. 267-273, Toronto, Canada, July 28-August 01, 2003.

[118] D. D. Lee and H. S. Seung, Algorithms for Non-negative Matrix Factorization, *In Proceedings of Advances in Neural Information Processing Systems (NIPS)*, Vol. 13, pp. 556-562, Vancouver, British Columbia, Canada, December, 2001.

Vita

Personal Data:

Ahthor's Name: Xuwei Liang

Birth Place: Shanxi, China

Birth Date: 06/24/1967

Educational Background:

- M.A. in Computer Science, Wayne State University, Detroit, Michigan 48202, August 2006
- M.S. in Applied Statistics, Bowling Green State University, Bowling Green, Ohio 43402, August 2003
- M.E. in Electrical and Computer Engineering, Tianjin Polytechnic University, Tianjin 300160, P. R. of China, May 1993
- B.E. in Optical Technology, Beijing Institute of Technology, Beijing 10082, P. R. of China, 1986

Professional Experience:

- Research Associate, Department of Computational Science, University of South Carolina Beaufort, Bluffton, South Carolina, May 2011 - August 2011
- Visiting Assistant Professor, Department of Computer Science, Eastern Kentucky University, Richmond, Kentucky, December 2010 - May 2011
- Teaching/Research Assistant, University of Kentucky, Lexington, Kentucky, 2006 - 2009

- Teaching/Research Assistant, Wayne State University, Detroit, Michigan, 2004 - 2006
- Associate Professor/ Lecturer, Tianjin Polytechnic University, Tianjin, China, 1993 - 2000

Awards:

- The 2010 - 2011 Dissertation Year Fellowship from the President's Office of University of Kentucky
- The 2010 Thaddeus B. Curtz Memorial Scholarship in the Department of Computer Science at University of Kentucky
- One of the two best papers out of approximately 2200 submitted papers at the 2nd International Conference on Bioinformatics and Biomedical Engineering (iCBBE 2008), Shanghai, China, May 15 - 18, 2008
- Student Travel Support, Graduate School, University of Kentucky, 2007 - 2009.

Refereed Publications:

- Xuwei Liang, Ning Kang, Stephen E. Rose, and Jun Zhang, A framework for quantitative and visual analysis of white matter integrity using diffusion tensor imaging, *International Journal of Functional Informatics and Personalised Medicine (IJFIPM)*, Vol.2,No.2: pp.159-174, 2009.
- Xuwei Liang, Jie Wang, Zhenmin Lin, and Jun Zhang, White matter fiber tract segmentation using nonnegative matrix factorization, *in Proceedings of the 3rd International Conference on Bioinformatics and Biomedical Engineering (iCBBE 2009)*, Vol.1, pp.1-4, Beijing, China ,June 11 - 13, 2009.

- Xuwei Liang, Qi Zhuang, Ning Cao, and Jun Zhang, Shape modeling and clustering of white matter fiber tracts using Fourier descriptors, *in Proceedings of the IEEE Symposium on Computational Intelligence in Bioinformatics and Computational Biology (CIBCB 2009)*, pp.292-297, Nashville, TN, USA, March 30 - April 2, 2009.

- Xuwei Liang, Qi Zhuang, Ning Cao, and Jun Zhang, Quantitative and visual analysis of white matter integrity using diffusion tensor imaging, *in Proceedings of the International Society for Optical Engineering (SPIE) Medical Imaging 2009 (SPIE 2009)*, Vol.7261, 726131 (2009), Lake Buena Vista (Orlando Area), Florida, USA, February 7 - 12, 2009.

- Qi Zhuang, Xuwei Liang, Ning Cao, and Jun Zhang. Generalized analytic expressions for the b matrix of twice-refocused spin echo pulse sequence, *in Proceedings of the International Society for Optical Engineering (SPIE) Medical Imaging 2009 (SPIE 2009)*, Vol. 7259, 725920 (2009), Lake Buena Vista (Orlando Area), Florida, USA, February 7 - 12 2009.

- Ning Cao, Xuwei Liang, Qi Zhuang, and Jun Zhang, Approximating high angular resolution apparent diffusion coefficient profiles using spherical harmonics under biGaussian assumption, *in Proceedings of the International Society for Optical Engineering (SPIE) Medical Imaging 2009 (SPIE 2009)*, Vol.7262, 726204 (2009), Lake Buena Vista (Orlando Area), Florida, USA, February 7 - 12 2009.

- Xuwei Liang and Jun Zhang, White matter integrity analysis along the cingulum paths in mild cognitive impairment - a geodesic distance approach, *in Proceedings of the 2nd International Conference on Bioinformatics and Biomedical Engineering (iCBBE 2008)*, Vol.1, pp.510-513, Shanghai, China, May 15-18, 2008 (Best Paper Award).

- Jun Zhang and Xuwei Liang, Diffusion tensor analysis for detecting white matter

changes in mild cognitive impairment, *The Journal of the Alzheimer's association*, Vol.4, No.4, (Suppl 2):T70, 2008.

- Cui Lin, Shiyong Lu, Xuwei Liang, Jing Hua, and Otto Muzik, Cocluster Analysis of Thalamo-Cortical Fiber Tracts Extracted from Diffusion Tensor MRI, *International Journal of Data Mining and Bioinformatics (IJDMB)*, Vol.2, No.4, pp.342 - 361, 2008.

- Ning Cao, Qi Zhuang, Xuwei Liang, Ruiwang Huang and Jun Zhang, Computing White Matter Fiber Orientations in High Angular Resolution Diffusion-Weighted MRI, *in Proceedings of the 1st IEEE International Conference on Bioinformatics and Biomedical Engineering (ICBBE 2007)*, pp.752-755, Wuhan, China, July 6-8, 2007.

- Jun Zhang and Xuwei Liang, Diffusion tensor analysis of white matter pathways of amnestic mild cognitive impairment, *in Hot Topics Addendum of the Alzheimer's Association International Conference on Prevention of Dementia*, pages P-227, Washington, DC, USA, June 9 - 12, 2007.

- Cui Lin, Shiyong Lu, Xuwei Liang, Jing Hua, and Otto Muzik, Genetic coclustter analysis of Thalamo-Cortical Connectivity in Human Brain, *in Proceedings of MICWIC*, pp.18-24, Hickory Corners, MI, USA, March, 2007.

- Cui Lin, Shiyong Lu, Xuwei Liang, and Jing Hua, GCA: A Coclustering Algorithm for Thalamo-Cortico-Thalamic Connectivity Analysis, *in Proceedings of IEEE International Conference on Data Mining (ICDM)*, pp. 163-168, Hong Kong, China, December 18 - 22, 2006.

- Xuwei Liang, Jing Hua, and Weiping Ren, Volumetric Histology Data Visualization and Quantitative Analysis, *in Proceedings of 2005 NAFIPS Annual Conference on*

Soft Computing for Real World Applications, pp.638 - 643, Ann Arbor, Michigan, USA, June 22-25, 2005.

- Xuwei Liang, Zhongyuan Wu, Xinguo Zhuang, Xianji Meng, Yanhua Liu, and Zheng Di, A novel approach to reduce the computational workload for sensitivity analysis in cathodic protection System, *Journal of the Tianjin Institute of Textile Science and Technology (ISSN 1671-024X, CN 12-1341/TS)*, Vol. 18(2), DOI: CNKI:SUN:TJFZ.0.1999-02-017, 1999.

- Xuwei Liang, Zhongyuan Wu, Yanhua Liu, Zheng Di, Xinguo Zhuang, and Xianji Meng, Optimal control of current in cathodic protection system, *Journal of the Tianjin Institute of Textile Science and Technology (ISSN 1671-024X, CN 12-1341/TS)*, Vol. 18(1), pp. 37-41, DOI: cnki:ISSN:1000-1557.0.1999-01-008, 1999.

- Xianji Meng, Zhongyuan Wu, Xuwei Liang, Xinguo Zhuang, Zhenkun Yuan, and Yanhua Liu, Improvement of the algorithm for the regional cathodic protection model, *Journal of Chinese Society for Corrosion and Protection (ISSN: 1005-4537 CN: 31-1421/TG)*, Vol. 18(3), pp. 221 - 226, 1998

- Xuwei Liang, Zhongyuan Wu, Xianji Meng, and Xinguo Zhuang, Study on the computer assisted optimal design for the regional cathodic protection system, *Journal of the Tianjin Institute of Textile Science and Technology (ISSN 1671-024X, CN 12-1341/TS)*, Vol. 17(5), pp. 90-94, DOI: CNKI:SUN:TJFZ.0.1998-05-018, 1998.

- Zhongyuan Wu, Yongcai Wang, Xuwei Liang, and Hongju Lin, Stability of the optimization procedure and its improvement for the regional cathodic protection model, *Journal of the Tianjin Institute of Textile Science and Technology (ISSN 1671-024X, CN 12-1341/TS)*, Vol. 17(5), pp. 95-98, DOI: CNKI:SUN:TJFZ.0.1998-05-019, 1998.

- Xuwei Liang and Minhui Wang, Graduate Student Information Management System,

Journal of the Tianjin Institute of Textile Science and Technology (ISSN 1671-024X, CN 12-1341/TS), Vol. 16(6), DOI: CNKI:SUN:TJFZ.0.1997-06-017, 1997.

- Xuwei Liang and Changjun Chen, A novel technique of system floppy disk copy protection - the double lock *Journal of the Tianjin Institute of Textile Science and Technology (ISSN 1671-024X, CN 12-1341/TS)*, Vol. 16(4), DOI: CNKI:SUN:TJFZ.0.1997-04-013, 1997.

- Zhongyuan Wu, Xuwei Liang, Xianji Meng, and Liping Bai, Algorithmic improvement on the regional cathodic protection potential distribution, *Journal of the Tianjin Institute of Textile Science and Technology (ISSN 1671-024X, CN 12-1341/TS)*, Vol. 16(4), DOICNKI:SUN:TJFZ.0.1997-04-011, 1997.

- Xinguo Zhuang, Xianji Meng, and Xuwei Liang, The evolvement and current development on the cathodic protection system design, *China Harbour Engineering*, 1996(6), DOI: CNKI:SUN:GKGC.0.1996-06-012, 1996.

Professional Affiliations:

- Member, Association for Computing Machinery (ACM)